

SLENDER CONCRETE COLUMNS REINFORCED WITH  
FIBER REINFORCED POLYMER SPIRALS

by

Thomas A. Hales

A dissertation submitted to the faculty of  
The University of Utah  
in partial fulfillment of the requirements for the degree of

Doctor of Philosophy

Department of Civil and Environmental Engineering

The University of Utah

May 2015

Copyright © Thomas A. Hales 2015

All Rights Reserved

# The University of Utah Graduate School

## STATEMENT OF DISSERTATION APPROVAL

The dissertation of Thomas A. Hales  
has been approved by the following supervisory committee members:

<u>Chris P. Pantelides</u>	, Chair	<u>Nov. 21, 2014</u> Date Approved
<u>Lawrence D. Reveley</u>	, Member	<u>Nov. 21, 2014</u> Date Approved
<u>Luis F. Ibarra</u>	, Member	<u>Nov. 21, 2014</u> Date Approved
<u>Amanda C. Bordelon</u>	, Member	<u>Nov. 21, 2014</u> Date Approved
<u>Daniel O. Adams</u>	, Member	<u>Nov. 21, 2014</u> Date Approved

and by Michael E. Barber, Chair/Dean of  
the Department/College/School of Civil and Environmental Engineering

and by David B. Kieda, Dean of The Graduate School.

## ABSTRACT

Corrosion in commonly used epoxy-coated steel reinforcing bars has raised concern with its use and has increased interest in the use of alternative reinforcement including fiber-reinforced polymer (FRP) bars. Glass FRP (GFRP) bars are a cost-competitive alternative in conditions where chloride-induced deterioration is an issue. There has been considerable research and code-writing effort towards using GFRP bars in construction of bridge deck and beam elements but these efforts are still somewhat limited with regards to the use of FRP bars in construction of column elements and particularly in the use of FRP-spiral confining hoops or spirals. Steel spiral reinforcement is commonly used in concrete columns for confinement and improvement of displacement ductility but little is known regarding the use of FRP-spiral reinforcement for confinement.

The purpose of this research is to gain a better understanding of the behavior and performance of FRP reinforcement for short as well as slender concrete columns, particularly FRP-spiral confining reinforcement, to better determine its viability as a potential construction alternative. Tests were conducted on nine circular concrete columns reinforced with internal GFRP-spirals and either steel, GFRP or a combination of steel and GFRP longitudinal bars. Axial load tests were conducted on both slender and short columns with loads placed at two eccentricities to observe the mode of failure, load capacity, and general behavior associated with different geometric and loading

conditions.

The test data is analyzed and a confinement model based on plasticity theory is derived to describe the axial strength and stress-strain relationship for FRP-spiral-confined circular columns. The confinement model is used to predict the moment-curvature relationship for FRP-spiral-confined circular columns. An analytical buckling model is developed, based on a numerical integration method, to describe the load-deflection behavior for slender FRP-spiral-confined circular columns.

Axial load and bending moment interaction diagrams are produced for FRP-spiral-confined slender columns. The analytical buckling model is also used in parametric studies of large-scale slender columns to compare steel with FRP spirals in addition to other comparisons between reinforcement configurations and concrete compressive strength.

## TABLE OF CONTENTS

ABSTRACT.....	iii
LIST OF TABLES.....	viii
LIST OF FIGURES .....	ix
ACKNOWLEDGEMENTS.....	xv
Chapters	
1 INTRODUCTION .....	1
1.1 General Background.....	2
1.2 Research Background.....	4
1.2.1 General Analysis of Reinforced Concrete Columns .....	5
1.2.2 Concrete Columns Utilizing External FRP Reinforcement (FRP Wrap).....	7
1.2.3 Concrete Columns Utilizing Internal FRP Reinforcement.....	8
1.2.4 Analysis of Slender Columns .....	12
2 FULL-SCALE EXPERIMENTS.....	16
2.1 General Approach.....	16
2.2 Specimen Materials and Construction Details.....	17
2.3 Experimental Setup.....	19
2.4 Experimental Results .....	20
2.4.1 Short Columns Loaded Concentrically .....	20
2.4.2 Tall Columns Loaded with 1 in. Eccentricity.....	21
2.4.3 Tall Columns Loaded with 4 in. Eccentricity.....	22
2.5 Experimental Summary .....	23
3 ANALYTICAL CONFINEMENT MODEL FOR FRP-SPIRAL-CONFINED CONCRETE .....	56
3.1 Plasticity Theory Overview .....	57
3.2 Willam and Warnke (1975) Five-Parameter Concrete Model.....	59
3.3 Axial Strength of FRP-Confined Concrete and the Modified Willam-Warnke Model.....	61

3.3.1	Axial Strength of FRP-Confined Normal- and High-Strength Concrete ..	63
3.3.2	Axial Strength of FRP-Confined High-Strength Concrete.....	65
3.3.3	Modified Axial Strength of FRP-Confined Normal- and High-Strength Concrete .....	66
3.3.4	Comparison of Axial Strength Equations.....	68
3.4	Theoretical Stress-Strain Relationship of FRP-Confined Concrete .....	70
3.5	Internal FRP-Spiral Confining Pressure .....	73
3.6	Implementation of Internal FRP-Confined Concrete Model .....	76
3.7	Axial Load Capacity of Internal FRP-Confined Concrete Columns .....	77
<b>4</b>	<b>ANALYTICAL BUCKLING MODEL FOR SLENDER FRP-SPIRAL-CONFINED CIRCULAR COLUMNS.....</b>	<b>90</b>
4.1	Column Cross-Sectional Analysis .....	91
4.2	Slender Column Buckling Model .....	93
4.2.1	General Approach.....	93
4.2.2	Axial Load-Moment-Curvature Relationship.....	95
4.2.3	Numerical Integration Function for Column Deflection .....	96
4.2.4	Deriving the Ascending Branch of the Load-Deflection Curve.....	96
4.2.5	Deriving the Descending Branch of the Load-Deflection Curve .....	99
4.3	Slender Column Analytical Buckling Model Verification .....	101
4.3.1	Model Verification with Cranston (1972) Analytical Model .....	102
4.3.2	Model Verification with Kim and Yang (1995) Experimental Results...	104
4.3.3	Model Verification with Claeson and Gylltoft (1998) Experimental Results .....	105
4.3.4	Model Verification with Fitzwilliam and Bisby (2006) Experimental Results .....	107
4.3.5	Model Verification with Ranger and Bisby (2007) Experimental Results .....	108
4.3.6	Model Comparison with the Experimental Results of the Present Study.....	109
4.3.6.1	Load-Deflection Curves #4T-DB1, #5T-SS1, and #6T-SG1 .....	110
4.3.6.2	Load-Deflection Curves #7T-DB4, #8T-SS4, and #9T-SG4 .....	113
4.3.6.3	Axial Load-Moment Interaction Curves DB, SS, and SG Columns .....	116
4.3.6.4	Slender Column Interaction Curves for DB, SS, and SG Columns .....	117
4.4	Parametric Studies Using Present Model .....	118
4.4.1	Parametric Study 1 – GFRP, CFRP, or Steel Spiral .....	118
4.4.2	Parametric Study 2 – Large-Scale Column .....	123
4.4.3	Parametric Study 3 – Longitudinal Reinforcement .....	127
4.4.4	Parametric Study 4 – Compressive Concrete Strength.....	129
<b>5</b>	<b>SUMMARY AND CONCLUSIONS .....</b>	<b>164</b>
5.1	Summary.....	164

5.2 Conclusions.....	170
6 RECOMMENDATIONS FOR FUTURE RESEARCH.....	172
REFERENCES .....	174

## LIST OF TABLES

### Tables

2.1: Summary of specimen construction and load eccentricity .....	28
2.2: Summary of max. load, horizontal deflection, and strain test results .....	28
3.1: Summary of analytical and experimental test load capacities of the short columns of the present study and four columns of Pantelides et al. (2013a) .....	79
4.1: Summary of Cranston (1972) specimens used for comparison .....	132
4.2: Detail of properties used for Cranston specimens with present model .....	132
4.3: Summary of Kim and Yang (1995) specimens used for comparison .....	133
4.4: Summary of Claeson and Gylltoft (1998) specimens used for comparison .....	133
4.5: Summary of properties of Fitzwilliam and Bisby (2006) specimens used for comparison .....	134
4.6: Summary of properties of Ranger and Bisby (2007) specimens used for comparison .....	134
4.7: Required spiral pitch to achieve equivalent confinement strength based on proposed models .....	135

## LIST OF FIGURES

### Figures

1.1: Examples of corrosion and concrete degradation on bridge structures .....	15
2.1: Reinforcement of 12 in. diameter concrete columns .....	29
2.2: Elevation of 12 in. diameter concrete columns.....	29
2.3: Typical strain gauge placement on column reinforcing bars.....	30
2.4: Column testing setup .....	31
2.5: Short column setup for concentric loading condition.....	31
2.6: Tall column setup for eccentric loading condition .....	32
2.7: Typical short column setup (column #1S-DB0 shown).....	33
2.8: Short columns tested to failure (concentric load) .....	34
2.9: Failure details of column #1S-DB0 .....	34
2.10: Failure details of column #2S-SS0 .....	35
2.11: Failure details of column #3S-SG0.....	35
2.12: Axial stress vs. axial strain for column #1S-DB0.....	36
2.13: Axial stress vs. axial strain for column #2S-SS0.....	36
2.14: Axial stress vs. axial strain for column #3S-SG0 .....	37
2.15: Comparison of axial stress vs. axial strain for all short columns .....	37
2.16: Typical tall column setup (column #4T-DB1 shown).....	38
2.17: Tall columns tested to failure (1 in. eccentricity) .....	39

2.18: Failure details of column #4T-DB1 .....	40
2.19: Failure details of column #5T-SS1 .....	41
2.20: Failure details of column #6T-SG1 .....	42
2.21: Load-deflection curve for column #4T-DB1 .....	43
2.22: Axial stress vs. axial strain curve for column #4T-DB1 .....	43
2.23: Load-deflection curve for column #5T-SS1 .....	44
2.24: Axial stress vs. axial strain curve for column #5T-SS1 .....	44
2.25: Load-deflection curve for column #6T-SG1 .....	45
2.26: Axial stress vs. axial strain curve for column #6T-SG1 .....	45
2.27: Comparison of load-deflection curves for columns #4T-DB1, #5T-SS1, and #6T-SG1 .....	46
2.28: Comparison of axial stress vs. axial strain curves for columns #4T-DB1, #5T-SS1, and #6T-SG1 .....	46
2.29: Tall columns tested to failure (4 in. eccentricity) .....	47
2.30: Tall columns tested to failure (4 in. eccentricity) .....	48
2.31: Failure details of column #7T-DB4 .....	49
2.32: Failure details of column #8T-SS4 .....	50
2.33: Failure details of column #9T-SG4 .....	51
2.34: Load-deflection curve for column #7T-DB4 .....	52
2.35: Axial stress vs. axial strain curve for column #7T-DB4 .....	52
2.36: Load-deflection curve for column #8T-SS4 .....	53
2.37: Axial stress vs. axial strain curve for column #8T-SS4 .....	53
2.38: Load-deflection curve for column #9T-SG4 .....	54
2.39: Axial stress vs. axial strain curve for column #9T-SG4 .....	54

2.40: Comparison of load-deflection curves for columns #7T-DB4, #8T-SS4, and #9T-SG4 .....	55
2.41: Comparison of axial stress vs. axial strain curves for columns #7T-DB4, #8T-SS4, and #9T-SG4.....	55
3.1: Three-dimensional stress space .....	80
3.2: State of stress at a point projected on a deviatoric plane .....	80
3.3: Willam-Warnke ultimate surface.....	81
3.4: Failure data points for triaxial compression concrete tests – normal- and high-strength concrete ( $\overline{\sigma}_a <  -1.4 $ ).....	82
3.5: Failure data points for triaxial compression concrete tests – high-strength concrete $> 8,000$ psi ( $\overline{\sigma}_a <  -1.4 $ ) .....	82
3.6: Failure data points for triaxial compression concrete tests – normal- and high-strength concrete ( $\overline{\sigma}_a <  -0.8 $ ).....	83
3.7: Failure data points for triaxial compression concrete tests – comparison of all curves.....	84
3.8: Failure data points for triaxial compression concrete tests – comparison of present study curves.....	84
3.9: Comparison of different axial strength models for confined concrete .....	85
3.10: Comparison of different axial strength models for confined concrete .....	85
3.11: Evolution of loading surfaces .....	86
3.12: Generic stress-strain relation for unconfined and confined concrete .....	86
3.13: Stress-strain curve for concrete with hardening behavior .....	87
3.14: Half-body diagram at interface between spiral and concrete core.....	87
3.15: Effectively confined core for spiral reinforcement.....	88
3.16: Simplified stress-strain curves for steel, CFRP, and GFRP reinforcement .....	89

4.1: Strains and stresses over a circular reinforced concrete cross-section confined by one or more spirals.....	136
4.2: Schematic of the theoretical model.....	136
4.3: Moment-curvature curves for two axial loads of a sample column.....	137
4.4: Example of bisection method for finding descending branch of load-deflection curve .....	138
4.5: Cross-section of Cranston (and other rectangular) columns.....	139
4.6: Stress-strain curves used for Cranston columns .....	139
4.7: Comparison of present model with Cranston’s analytical model (Cranston1) .....	140
4.8: Comparison of present model with Cranston’s analytical model (Cranston2) .....	140
4.9: Comparison of present model with Cranston’s analytical model (Cranston3) .....	141
4.10: Comparison of present model with Cranston’s analytical model (Cranston4) .....	141
4.11: Stress-strain curves used for other column comparisons.....	142
4.12: Comparison of present model with Kim and Yang’s experimental tests (Columns KY60L2-1 and KY60L2-2).....	143
4.13: Comparison of present model with Kim and Yang’s experimental tests (Columns KY100L2-1 and KY100L2-2).....	143
4.14: Comparison of present model with Claeson and Gylltoft’s experimental tests (Columns CG23 and CG24) .....	144
4.15: Comparison of present model with Claeson and Gylltoft’s experimental tests (Columns CG27 and CG28) .....	144
4.16: Comparison of present model with Claeson and Gylltoft’s experimental tests (Columns CG31 and CG32) .....	145
4.17: Cross-section of Fitzwilliam and Bisby (2006) and Ranger and Bisby (2007) columns.....	146

4.18: Comparison of present model with Fitzwilliam and Bisby’s experimental tests (Columns FB1 and FB2).....	146
4.19: Comparison of present model with Ranger and Bisby’s experimental tests (Columns RB-U5, RB-U10, RB-U20, RB-U30, and RB-U40).....	147
4.20: Assumed load transfer through steel plate to obtain effective eccentricity of 0.81 in. for columns #4T-DB1, #5T-SS1, and #6T-SG1 .....	148
4.21: Comparison of present model with present experimental test #4T-DB1.....	149
4.22: Comparison of present model with present experimental test #5T-SS1.....	149
4.23: Comparison of present model with present experimental test #6T-SG1 .....	150
4.24: Comparison of modeled load-deflection curves for columns #4T-DB1, #5T-SS1, and #6T-SG1 using 0.81 in. eccentricity .....	150
4.25: Assumed load transfer through steel plate to obtain effective eccentricity of 3.66 in. for columns #7T-DB4, #8T-SS4, and #9T-SG4.....	151
4.26: Comparison of present model with present experimental test #7T-DB4.....	152
4.27: Comparison of present model with present experimental test #8T-SS4.....	152
4.28: Comparison of present model with present experimental test #9T-SG4 .....	153
4.29: Comparison of modeled load-deflection curves for columns #7T-DB4, #8T-SS4, and #9T-SG4 using 3.66 in. eccentricity .....	153
4.30: Axial load-moment interaction curve for DB columns .....	154
4.31: Axial load-moment interaction curve for SS columns.....	154
4.32: Axial load-moment interaction curve for SG columns .....	155
4.33: Slender column axial load-moment interaction curve for DB columns .....	155
4.34: Slender column axial load-moment interaction curve for SS columns .....	156
4.35: Slender column axial load-moment interaction curve for SG columns.....	156
4.36: Comparison of stress-strain curves used for Parametric Study 1 and models of columns tested in present study .....	157
4.37: Load-deflection curves for Parametric Study 1 – DB columns .....	158

4.38: Load-deflection curves for Parametric Study 1 – SS columns .....	158
4.39: Load-deflection curves for Parametric Study 1 – SG columns .....	159
4.40: Comparison of load-deflection curves for Parametric Study 1 columns – GFRP-spiral .....	159
4.41: Comparison of load-deflection curves for Parametric Study 1 columns – CFRP-spiral .....	160
4.42: Comparison of load-deflection curves for Parametric Study 1 columns – steel spiral .....	160
4.43: Comparison of stress-strain curves used for Parametric Study 2 and models of columns tested in present study .....	161
4.44: Comparison of load-deflection curves for Parametric Study 2 columns .....	161
4.45: Comparison of load-deflection curves for Parametric Study 3 columns .....	162
4.46: Comparison of load-deflection curves for Parametric Study 4 columns .....	163

## ACKNOWLEDGEMENTS

I would like to first express my sincere appreciation and gratitude to my mentor, friend, and academic advisor Dr. Chris Pantelides for his support, guidance, and encouragement in helping me achieve this longtime goal. Also, I would like to extend a special thanks to Dr. Larry Reaveley for his enthusiasm and helpful input and insight with this research.

I am thankful for the helpful suggestions and support provided by my other committee members Dr. Luis Ibarra, Dr. Amanda Bordelon, and Dr. Dan Adams. Thank you to Mark Bryant, Ruifen Liu, Mike Gibbons, Hughes Bros Inc., and Hanson Structural Precast for their contributions and help with the experimental portion of this project.

Lastly, and most importantly, I would like to express my deepest gratitude and appreciation to my dear wife, Krissy, for her tremendous sacrifice and devotion, and our five children, Matt, Bryce, Tyler, Emma, and Gracie. Without their unconditional love, encouragement and support (including getting hands dirty helping with the experimental portion of the project) this academic adventure would not have been possible.

## CHAPTER 1

### INTRODUCTION

The concept of strengthening concrete structural elements with fiber-reinforced polymer (FRP) composites has been around for many years. Some of its earliest uses involved the retrofit and rehabilitation of existing concrete structural elements through utilization of FRP wraps, jackets, or strips applied externally to concrete members. This was found to be a desirable and cost effective way to increase the strength and displacement ductility of existing concrete elements. Much of the need to strengthen and retrofit these concrete elements came from the detrimental effects of corrosion occurring in the steel reinforcement or deficient reinforcement details. This is particularly true with reinforced concrete structures used in transportation infrastructure.

Concrete bridge structures are typically designed to last at least 50 to 75 years but seldom last half that time before needing major rehabilitation of certain structural elements due to premature strength degradation. This degradation is due to the severe environmental conditions that these structures are subjected to, such as fluctuations in temperature, number of freeze-thaw cycles, improper drainage, and presence of deicing salts, which cause expansion of corroded steel reinforcement and subsequent deterioration of concrete through cracking and spalling similar to that shown in Figure 1.1. This results in major rehabilitation costs and traffic disruption due to these adverse

effects as well as a significant reduction in the life of the structure.

### 1.1 General Background

Over the past several years, many solutions have been investigated for overcoming steel reinforcement corrosion including glass fiber-reinforced polymer (GFRP) bars, stainless-steel bars, polymer-impregnated concrete, electro-static-spray fusion-bonded (powder resin) coating, galvanized coating, and epoxy coating. For many years, epoxy-coated steel reinforcement has been the method of choice for many state transportation departments in an effort to reduce the corrosion problem. Now that epoxy-coating has been in use for over 30 years it is being found to not be as effective as originally hoped for with some structures experiencing corrosive degradation (Sohanghpurwala and Scannall 1999). This is often attributed to defects in the epoxy coating by way of nicks, cracks, or breaks that allow the initiation of the corrosion process at those locations. After the initiation of corrosion in epoxy coated bars the process is often accelerated due to a concentrated effect that occurs at the defect.

The problems associated with epoxy-coated steel reinforcing bars have raised concern with its use and have increased interest in the use of alternative reinforcement materials such as GFRP bars. It has been found through research that fiber-reinforced polymer (FRP) bars are not affected by corrosion (Tobbi et al. 2012, Pantelides et al. 2013a). As a result, many of the costs and user impacts associated with addressing the corrosion problem could potentially be eliminated with a proactive approach of using corrosive resistant reinforcement in the original construction of concrete structures exposed to such environments. This also is potentially a much more economical and less

disruptive approach than the reactive approach of retrofitting structures with external FRP jackets after degradation has occurred.

A significant amount of research has been carried out in recent years to study and investigate the performance of FRP materials with concrete construction. FRP materials are commercially available utilizing Aramid FRP (AFRP), Carbon FRP (CFRP), or GFRP fibers, which are embedded in a resin matrix and formed using a variety of techniques including pultrusion, braiding, and weaving (Bank 1993). Typical FRP reinforcement products used for civil engineering applications include fabrics, grids, ropes, and bars.

FRP reinforcement mechanically behaves differently than conventional steel reinforcement. One of the major differences is that FRP reinforcement does not yield and generally exhibits elastic behavior until failure. This brittle characteristic, as compared with ductile steel reinforcement, causes a lack of ductility in structural concrete members, which is an important factor to consider when utilizing FRP reinforcing bars. GFRP reinforcement has a substantially lower modulus of elasticity as compared to steel reinforcement, which can contribute to larger deflections in structural elements. The compressive strength of GFRP reinforcing bars is lower than its tensile strength and is also lower than the compressive strength of steel reinforcement. On the other hand, GFRP bars have a higher tensile strength compared to steel by roughly 65%, which can present an advantage over steel reinforcement in providing increased tensile capacity.

GFRP reinforcement is more economical than other available types such as AFRP and CFRP and is more attractive for infrastructure applications and the construction industry (Pantelides et al. 2013b). It also can be a cost-competitive alternative to other

corrosion resistant methods of reinforcement such as epoxy-coated reinforcing bars.

GFRP bars are also lighter than steel bars, which can make transportation, handling and construction easier and more economical than steel reinforcement.

There has been a considerable amount of research, testing, and code-writing effort towards the use of FRP bars in construction of bridge deck and beam elements, but these efforts are still somewhat limited with regards to the use of FRP bars in construction of column elements. The Canadian Highway Bridge Design Code (CHBDC CAN/CSA-S6-06), the AASHTO LRFD Bridge Design Guide Specifications for GFRP-Reinforced Concrete Bridge Decks and Traffic Railings, and ACI 440.1R-06 are examples of codes introducing new design guidelines for use of FRP reinforcement.

The purpose of this research was to gain a better understanding of the behavior and performance of FRP reinforcement in concrete columns and to better determine its viability as a potential construction alternative. The use of FRP longitudinal bars and spirals as internal reinforcement of concrete columns could potentially be an economically viable approach for constructing corrosion resistant columns.

## 1.2 Research Background

The idea of using FRP composite materials as reinforcement in concrete columns has been of interest to the research community in recent years. Its use as external reinforcement has been more extensively researched than its use as internal reinforcement largely due to its significant ability to add flexural and shear strength as well as confinement, resulting in improved displacement ductility for existing steel-reinforced concrete columns. Research investigating the use of FRP bars as internal reinforcement

for concrete columns is somewhat limited with very little research reported regarding the use FRP-spirals as internal confining reinforcement. A brief discussion follows that identifies previous research conducted similar in nature to the present study and is outlined in the following categories: 1) general analysis of reinforced concrete columns, 2) concrete columns utilizing external FRP reinforcement (FRP wrap), 3) concrete columns utilizing internal FRP reinforcement, and 4) analysis of slender columns.

### 1.2.1 General Analysis of Reinforced Concrete Columns

General compressive strength confinement models have been investigated for steel confining reinforcement for many years prior to the use of FRP confining reinforcement. Many of these models were based on concepts presented by Richart et al. (1928) who explored the triaxial states of stress of concrete. Mander et al. (1988) developed one of the earliest steel confining models based on the Willam-Warnke plasticity model (Willam and Warnke 1975). This model has been used as a basis and comparison for other confining models that have been developed afterwards.

Experiments performed by Sheikh and Toklucu (1993) on short circular concrete columns utilizing steel confining reinforcement found that for well-confined columns (approximately 1.7% or higher steel spiral ratio) the steel spiral yielded when concrete was subjected to the maximum stress; the increase in concrete strength due to confinement was observed to be between two to four times the lateral pressure.

Cusson and Paultre (1995) developed a stress-strain model for steel-confined, high-strength concrete square columns, which was compared to multiple large-scale test results. In this case it was found that the confining reinforcement did not necessarily

reach its yield stress at peak strength, and its overall strength was largely dependent on how well the column was confined with transverse tie reinforcement.

Imran and Pantazopoulou (1996) conducted extensive research to characterize the effects of confining pressure on the behavior of normal-strength concrete. The research demonstrated consistent enhancement of concrete strength and ductility under increasing lateral confinement. The effect of confining pressure on high-strength concrete was studied by Ansari and Li (1998), who found that the influence of confining pressure was less pronounced with high-strength concrete than it was with normal-strength concrete. For a given amount of confining pressure, the increase of axial strength capacity for the high-strength concrete was roughly one-half to two-thirds of that achieved in normal-strength concrete.

Additional research was conducted by Bing et al. (2001) in which steel-confined, high-strength concrete square and circular columns were tested with transverse ties or spirals closely spaced between 1 in. to 3 in. A stress-strain model was developed, and it was found that transverse reinforcement did reach its yield stress due to the high level of confinement. It was also determined that confined concrete strength was increased when higher yield strength ties or spirals were used.

With regards to this background research, and as presented in greater detail in the following chapters, the following observations of the present study can be briefly made as it relates to this background research: 1) the Willam-Warnke plasticity model is a useful method in developing a confining model, 2) the increase in axial-load capacity is largely dependent on how well confined the column is with transverse tie/spiral reinforcement, and 3) the influence of confining pressure was less pronounced for high-strength as

compared to normal-strength concrete.

### 1.2.2 Concrete Columns Utilizing External FRP Reinforcement (FRP Wrap)

There have been many tests performed on concrete columns reinforced with externally applied FRP wraps or jackets. These tests have been predominantly conducted on short columns as opposed to slender columns.

Lam and Teng (2003) developed a simplified stress-strain model for concrete confined by an FRP wrap with fibers predominantly oriented in the hoop direction. They were able to determine that the average hoop strain in the FRP at rupture potentially can be much lower than the ultimate tensile strain in the FRP material from flat coupon tests. This demonstrated that it is not valid to assume that FRP wraps rupture when the FRP material tensile strength is reached.

A confinement model based on the Willam-Warnke plasticity model was developed by Yan and Pantelides (2006) to express the axial strength capacity of FRP-wrapped concrete columns. This model incorporates the assumption that the FRP confinement exhibits linear behavior, and the confining stress varies continuously until failure. In contrast, the model developed by Mander et al. (1988) for steel-confined concrete assumes that the steel confining bar yields and behaves in a perfectly plastic manner and provides a constant confining stress in the concrete core until failure.

In general, the research has consistently shown that externally applied FRP wraps can potentially provide substantial confinement and increased load capacity. This was further demonstrated in tests performed on 4 in. by 4 in. by 12 in. tall square concrete columns by Benzaid et al. (2008).

Csuka and Kollar (2012) investigated a stress-strain model to better predict eccentrically loaded FRP-externally-confined (FRP-wrapped) concrete columns. Moran and Pantelides (2012) developed a theoretical mechanics-based stress-strain model for FRP-confined concrete that utilizes the concept of diagonal dilation and the principle of a two parameter Mohr-Coulomb-type failure envelope. This model utilized the fact that concrete is a restraint sensitive material whose dilation and compressive behavior depend on the FRP jacket stiffness in the hoop direction rather than on the passive confining pressure.

With regards to this background research, and as presented in greater detail in the following chapters, the following observations of the present study can be briefly made as it relates to this background research: 1) it is not necessarily valid to assume that FRP confinement ruptures when the FRP tensile strength is reached; 2) FRP confinement exhibits a linear, elastic behavior as opposed to steel confinement, which ideally yields and exhibits a plastic behavior; and 3) internal FRP confinement can provide improved column behavior but testing so far has not been able to produce the levels of improvement that have been observed with external FRP confinement.

### 1.2.3 Concrete Columns Utilizing Internal FRP Reinforcement

Early testing was performed on concrete columns reinforced with FRP bars by Alsayed et al. (1999). Fifteen specimens of rectangular cross-section were tested. All had a cross-section size of 10 in. (250 mm) by 18 in. (450 mm) and a 47 in. (1200 mm) height. Longitudinal reinforcement consisted of six 0.62 in. (16 mm) diameter steel or GFRP bars, and transverse reinforcement consisted of 0.24 in. (6 mm) diameter

rectangular ties at 4 in. (100 mm) spacing. They used varying configurations of steel and/or GFRP bars. It was found that replacing longitudinal steel reinforcing bars with GFRP bars of equivalent size reduced the axial capacity of the columns by an average of 13%. It was also found that replacing steel ties with GFRP ties of equivalent size reduced the axial capacity of the column by approximately 10% and that the use of GFRP ties in comparison to columns without ties had little influence on the load-deflection response of the columns up to approximately 80% of the ultimate capacity. These two observations were attributed to the low modulus of elasticity of the GFRP ties and the likelihood that the ties had little or no contribution to the confinement effort until subjected to the higher levels of load.

A parametric study performed by Mirmiran et al. (2001) determined that the use of FRP internal bars makes reinforced concrete columns more susceptible to slenderness effects due to the lower stiffness and compression contribution of FRP reinforcing bars. This was observed in columns with a longitudinal reinforcement ratio of at least the code minimum of 1% and where steel reinforcement was replaced with an equivalent amount of FRP reinforcement. It was also found that in rectangular concrete columns reinforced with internal longitudinal FRP bars, the interaction strength diagrams do not exhibit balanced points as defined by the ACI Building Code (ACI 318-05) code due to the yielding behavior of steel reinforcement as opposed to the linear-elastic behavior of FRP reinforcement (Choo et al., 2006).

De Luca et al. (2009, 2010) observed that very few studies had been conducted on concrete columns reinforced with FRP internal bars. They performed axial load tests on full-scale square concrete columns reinforced with two types of GFRP vertical

reinforcement with GFRP lateral confining ties and compared them with tests performed on steel-reinforced columns having identical reinforcing configurations. The square columns had a 2 ft by 2 ft cross-section and a height of 10 ft. All columns were reinforced identically with eight #8 longitudinal bars of their respective material type. The all-steel reinforced column had #4 ties at 16 in. spacing, but the all-GFRP reinforced columns had one column with #4 ties at 12 in. spacing and another column with #4 ties at 3 in. spacing to help account for the lower modulus of elasticity of the GFRP material. They determined that FRP compression reinforcement contributes very little to the axial load capacity of the column and found that a tie spacing of 3 in. provided a more desirable level of ductility than a tie spacing of 12 in.

Additional axial load tests were performed on square columns reinforced with GFRP vertical reinforcement and GFRP lateral confining ties by Tobbi et al. (2012). The columns were 14 in. (350 mm) by 14 in. (350 mm) by 55 in. (1400 mm) tall and were tested using four different tie configurations utilizing 0.5 in. (13 mm) diameter GFRP ties at either 4.72 in. (120 mm) or 3.15 in. (80 mm) spacing. Three tie configurations utilized eight 0.75 in. (19 mm) diameter longitudinal GFRP bars, and one tie configuration utilized 12 0.63 in. (16 mm) diameter longitudinal GFRP bars. They confirmed that the use of GFRP ties can be an effective means for providing confinement and reported that reducing the tie spacing from 4.72 in. (120 mm) to 3.15 in. (80 mm) achieved a strength gain of more than 20%. Although the authors indicated that additional experimental evidence is needed to more accurately validate this, it was estimated that the compressive strength of the GFRP bars could be approximated as 35% of the maximum tensile strength of the GFRP bars.

A concurrent program of research and testing conducted at the University of Utah (Pantelides et al., 2013a) evaluated the corrosion resistance of short circular concrete columns reinforced with GFRP-spirals compared to those reinforced with steel spirals. It was found that GFRP reinforcement was not affected by the effects of corrosion.

Afifi et al. (2013a, 2013b) and Mohamed et al. (2014) performed a series of experimental tests on circular columns reinforced with GFRP or CFRP longitudinal bars confined with either GFRP- or CFRP-spirals or hoops. A total of 30 columns reinforced only with FRP bars were tested in addition to four columns reinforced only with steel for comparison. The diameter and height of the columns were 11.8 in. (300 mm) and 5 ft (1500 mm), respectively, and they were reinforced with various configurations of FRP reinforcement, including different sizes and spacing of confinement reinforcement. The steel reinforced columns were reinforced with six 0.63 in. (16 mm) diameter longitudinal bars ( $\rho = 1.7\%$ ) and 0.37 in. (9.5 mm) diameter spirals at 3.15 in. (80 mm) spacing. The CFRP reinforced columns were reinforced typically with 10 0.5 in. (12.7 mm) diameter longitudinal bars ( $\rho = 1.8\%$ ) and with various spiral/hoop configurations with 0.37 in. (9.5 mm) diameter spirals at 1.57 in. (40 mm) spacing being the maximum used. The GFRP reinforced columns were reinforced typically with eight 0.63 in. (15.9 mm) diameter longitudinal bars ( $\rho = 2.3\%$ ) and with various spiral/hoop configurations with 0.37 in. (9.5 mm) diameter spirals at 1.57 in. (40 mm) spacing being the maximum used. In general, they found that FRP reinforcement could be a viable alternative to steel reinforcement for both longitudinal and confinement reinforcement, although the columns with steel reinforcement did provide for larger load capacities when compared with similarly reinforced columns utilizing FRP. The CFRP reinforced columns ( $\rho =$

1.8%) with the maximum spiral reinforcement (1.57 in. spacing) achieved nearly the same load capacity as the steel reinforced columns ( $\rho = 1.7\%$ ) with the spiral reinforcement at 3.15 in. spacing. CFRP reinforced columns, in general, outperformed GFRP reinforced columns.

With regards to this background research, and as presented in greater detail in the following chapters, the following observations of the present study can be briefly made as it relates to this background research: 1) FRP longitudinal bars provide a lower contribution to column compression capacity as compared to steel longitudinal bars, 2) FRP confinement reinforcing needs to be provided at closer spacing due to its lower modulus of elasticity, and 3) CFRP reinforcement provides better compression and confining strengths as compared to GFRP reinforcement.

#### 1.2.4 Analysis of Slender Columns

An approximate design method for slender reinforced concrete columns was developed by MacGregor et al. (1970) utilizing the moment magnifier principle to provide a simplified approach to account for slenderness effects in columns. Cranston (1972) presented a method of analysis to model the behavior of slender steel-reinforced concrete columns; the column deflected shape was able to be reasonably predicted based on a given axial load through an iterative process where a deflected shape is assumed, bending moments are calculated, and then adjusted; this process is repeated until equilibrium conditions are satisfied.

Tikka (2008) performed a study investigating the applicability of using the moment magnifier design approach as outlined in the Canadian Standards Association

(CSA) Standard A23.3 for concrete columns reinforced with GFRP bars. Ten columns were tested that contained GFRP longitudinal bars and GFRP U-shaped transverse ties. Seven columns had a size of 6 in. (150 mm) by 6 in. (150 mm) by 71 in. (1800 mm) tall and were reinforced with four 0.5 in. (12.7 mm) diameter GFRP longitudinal bars ( $\rho = 2.3\%$ ) and 0.24 in. (6 mm) GFRP U-shaped ties at 3.94 in. (100 mm) spacing. Three columns had a size of 4 in. (100 mm) by 6 in. (150 mm) by 71 in. (1800 mm) tall and were reinforced with four 0.5 in. (12.7 mm) diameter GFRP longitudinal bars ( $\rho = 3.4\%$ ) and 0.24 in. (6 mm) GFRP U-shaped ties at 2.36 in. (60 mm) spacing. Two steel-reinforced columns were also tested for comparison. One had a size of 6 in. (150 mm) by 6 in. (150 mm) by 71 in. (1800 mm) tall and the other had a size of 4 in. (100 mm) by 6 in. (150 mm) by 71 in. (1800 mm) tall. Both were reinforced with four 0.44 in. (11.3 mm) diameter longitudinal bars ( $\rho = 1.8\%$  and  $2.7\%$ , respectively) and were laterally tied with 0.13 in. (3.2 mm) diameter ties at 6 in. (150 mm) and 4 in. (100 mm) spacing, respectively. It was determined that the CSA moment magnifier design approach produced conservative designs for the all-GFRP reinforced columns. It was also found that the GFRP reinforcing bars did not contribute as much compression strength to the axial capacity of the columns as compared to steel reinforcing bars.

Fitzwilliam and Bisby (2010) and Jiang and Teng (2013) found that FRP-wrapped circular concrete columns are more susceptible to slenderness effects and that a reinforced concrete column originally classified as a short column may need to be considered a slender column after adding external FRP confinement. This phenomenon is due to the fact that external FRP-wrap confinement can substantially increase the axial

load capacity, but its flexural rigidity, in the range of confinement-enhanced resistance, is much lower than the initial flexural rigidity.

Jiang and Teng (2012, 2013) presented an analytical model for slender FRP-wrapped circular concrete columns based on the numerical integration method. They found reasonable agreement to existing test results through use of the Lam and Teng (2003) stress-strain model, which was developed to describe the behavior of FRP-wrapped concrete.

With regards to this background research, and as presented in greater detail in the following chapters, the following observations of the present study can be briefly made as it relates to this background research: 1) an iterative numerical integration method similar to that used by Jiang and Teng (2012, 2013) for external FRP-wrapped circular concrete columns was successfully used for the present study, which is similar in methodology to the method used by Cranston (1972) but is more accurate and detailed than the moment magnifier method presented by MacGregor et al. (1970), and 2) the effective levels of confinement achieved with internal FRP reinforcement have, so far, been considerably less than those achieved with external FRP-wraps, and the phenomenon found by Fitzwilliam and Bisby (2010) and Jiang and Teng (2013) for external FRP-wraps has yet to be observed for columns with internal FRP confinement.



(a)



(b)



(c)

Figure 1.1: Examples of corrosion and concrete degradation on bridge structures:  
(a) deck, girder, and pier cap elements; (b) abutment; (c) column

## CHAPTER 2

### FULL-SCALE EXPERIMENTS

GFRP reinforcement behaves in a linear elastic fashion until tensile failure, which is sudden and brittle. This type of failure is generally less desirable in contrast to a more ductile mode of failure. Consequently, it was of interest to test several columns with various reinforcement configurations, including steel and GFRP, under various loading conditions, such as concentric and eccentric compression, to investigate their behavior as short and slender columns.

High-strength concrete was also used due to its increased popularity for use in high capacity structures such as bridges utilizing both traditional and accelerated bridge construction (ABC) methods. Many of the precast elements utilized in ABC are incorporating high-strength concrete because of the improved technology, structural capacity, durability, and quality control that is available with its use.

#### 2.1 General Approach

The experimental testing portion of this research was conducted at the University of Utah Structural Testing Laboratory in conjunction with experiments conducted by Pantelides et al. (2013a) to utilize the specialized setup of the loading frame needed to perform the axial load tests which involved the use of two different lengths of loading

rams to accommodate both short and tall columns.

Tests were conducted on circular concrete columns reinforced with GFRP-spirals and either steel, GFRP, or a combination of steel and GFRP longitudinal bars. Axial compression tests were conducted for both slender and short columns with loads placed at varying eccentricities to observe the mode of failure, load capacity, and general behavior associated with different geometric and slenderness conditions.

## 2.2 Specimen Materials and Construction Details

A summary of the fabrication and loading eccentricity of each specimen is shown in Table 2.1. The specimens tested in the present research consisted of nine columns with a diameter of 12 in. constructed with high-strength concrete. Three columns were constructed with a height of 30 in., and six columns were constructed with a height of 12 ft, 3 in. The tall columns meet the criteria of being slender columns according to ACI 318-08 having a slenderness ratio  $kL/r$  of 49 ( $1 \times 147 \text{ in.} / [0.25 \times 12 \text{ in.}] = 49$ ). The end conditions were simulated as pinned-pinned.

Three configurations of reinforcement were used as shown in Figures 2.1 and 2.2. Three columns (Type DB) were reinforced with a double layer of reinforcement. This consisted of an inner layer of six #4 longitudinal steel bars confined with a 7 in. diameter #3 GFRP-spiral and an outer layer of six #5 longitudinal GFRP bars confined with an 8.5 in. diameter #3 GFRP spiral. The pitch for the inner and outer spirals was 3 in. as shown in Figures 2.1(a) and 2.2(a). Three columns (Type SS) were reinforced with a single layer of six #4 longitudinal steel bars confined with an 8.5 in. diameter #3 GFRP-spiral spaced at 3 in. on center as shown in Figures 2.1(b) and 2.2(b). The last three columns

(Type SG) were reinforced with a single layer of six #5 longitudinal GFRP bars confined with an 8.5 in. diameter #3 GFRP-spiral spaced at 3 in. on center as shown in Figures 2.1(b) and 2.2(b).

The Type SS columns utilized six #4 longitudinal steel bars, which provided a reinforcement ratio of  $\rho = 1.06\%$ , which meets the minimum 1% required reinforcement ratio of ACI 318-08. Due to the observations from past research that GFRP bars provide a lower contribution to column compression capacity as compared to steel longitudinal bars, it was decided to utilize six #5 longitudinal GFRP bars for the Type SG columns, which provided a reinforcement ratio of  $\rho = 1.65\%$ . The Type DB columns were selected to have a combination of both Type SS and Type SG reinforcement in a double-reinforced configuration to evaluate the effects of both types of reinforcement in one column, which provided for a reinforcement ratio of  $\rho = 2.71\%$ . Based on the recommendations of previous research that confinement reinforcement should be provided at no more than a 3 in. spacing, it was decided to have all columns confined with a #3 spiral at a 3 in. spacing for each layer of vertical reinforcement (therefore the DB columns had a double spiral provided).

The three short columns were tested under an axial load applied concentrically. These columns also helped provide an interrelationship between the present tests and tests of the short columns from the concurrent research by Pantelides et al. (2013a). Three of the tall columns were tested under an axial load applied at an eccentricity of 1 in., and the remaining three tall columns were tested under an axial load applied at an eccentricity of 4 in.

The properties for the specific lot of GFRP bars used in this research were tested

by the manufacturer and found to have an ultimate tensile strength of 103,700 psi and a modulus of elasticity of 6,280,000 psi. The properties of the steel bars had a yield strength of 64,000 psi and a modulus of elasticity of 29,000,000 psi. The concrete used in this research was high-strength and had a compressive strength,  $f'_c$ , of 13,000 psi at the time of testing.

### 2.3 Experimental Setup

All columns were tested using a tall loading frame and a hydraulic actuator capable of generating a load up to 2,000 kips. Loading was applied monotonically at a rate of 0.02 in. per minute.

All columns were instrumented with strain gauges and linear variable differential transformers (LVDTs) at the midheight of each column. All longitudinal bars had strain gauges placed at the midheight of the column to measure longitudinal strains. The spirals had strain gauges placed at four locations around the circumference, 90° apart, to measure radial strains at column midheight. Figure 2.3 shows the strain gauge attachment to reinforcing bars for three of the columns.

Concrete strain gauges were placed in four locations at midheight on the exterior concrete around the circumference of the column, 90° apart, to measure radial concrete strains. Vertical LVDTs were placed at four locations at midheight on the exterior of the column, 90° apart, to measure vertical concrete strains and displacements. Horizontal LVDTs were placed at two locations at midheight on the exterior of the tall columns, 90° apart, to measure the in-plane and out-of-plane horizontal deflections. A depiction of the column test setup is shown in Figure 2.4.

The short columns were prepared for testing by installing a 6 in. tall, 0.25 in. thick steel collar at both column ends to provide increased confinement and prevent end bearing failure. A 2 in. thick steel bearing plate was provided at the top of the column and a steel semihemispherical assembly was provided at the base of the column to simulate a pinned condition. This system provided a concentric axial load condition as shown in Figure 2.5.

The tall columns were prepared for testing by installing an 18 in. tall, 0.25 in. thick steel collar at both column ends to provide increased confinement and prevent end bearing failure. A 2 in. thick steel bearing plate and steel roller assembly were also provided at each end to simulate a pinned condition and an eccentric loading condition as shown in Figure 2.6.

## 2.4 Experimental Results

The experimental testing was accomplished in three phases as follows: 1) short columns loaded concentrically, 2) tall columns loaded with 1 in. eccentricity, and 3) tall columns loaded with 4 in. eccentricity.

### 2.4.1 Short Columns Loaded Concentrically

Three short columns were tested under concentric axial compressive load. Figure 2.7 shows the typical short column setup in the test frame. These columns are identified as #1S-DB0 (both steel and GFRP longitudinal bars with double spirals), #2S-SS0 (steel longitudinal bars), and #3S-SG0 (GFRP longitudinal bars). Column #1S-DB0 achieved a maximum load of 1,376 kips. Column #2S-SS0 achieved a maximum load of 1,498 kips.

Column #3S-SG0 achieved a maximum load of 1,602 kips. All three columns experienced sudden material-type failures at column midheight, which can be seen in Figures 2.8 through 2.11. As seen in these figures, column failure modes included compressive rupture of the longitudinal GFRP bars, tensile rupture of the GFRP-spiral, and compressive buckling of the longitudinal steel bars. The stress-strain curves for each of the short columns are shown in Figures 2.12 through 2.14 with a comparison of all three shown in Figure 2.15.

It is interesting to note in Figure 2.15 how the initial slope of the curve for column #1S-DB0, which had the double layer of reinforcement, matched more closely to that of column #3S-SG0 with GFRP longitudinal bars as opposed to that of column #2S-SS0, which had steel longitudinal bars. It was found, as described in Section 4.3.6, that due to the low modulus of elasticity of the GFRP spirals and the high strength of the concrete, the GFRP spirals were ineffective in contributing to the overall axial strength and stiffness of the column. However, it appears from the curves that the steel longitudinal bars spaced farther apart in column #2S-SS0 were able to effectively provide more indirect confinement and greater stiffness (as observed by the steeper curve) as opposed to column #1S-DB0, which had the steel longitudinal bars spaced closer together (therefore less concrete confined between the longitudinal bars) or column #3S-SG0 that was not reinforced with any steel longitudinal bars.

#### 2.4.2 Tall Columns Loaded with 1 in. Eccentricity

Three tall columns were tested under axial compressive load with 1 in. eccentricity. Figure 2.16 shows the typical tall column setup in the test frame. These

columns are identified as #4T-DB1 (both steel and GFRP longitudinal bars), #5T-SS1 (steel longitudinal bars), and #6T-SG1 (GFRP longitudinal bars). Column #4T-DB1 achieved a maximum load of 925 kips with a maximum midheight horizontal deflection of 0.28 in. Column #5T-SS1 achieved a maximum load of 850 kips with a maximum midheight horizontal deflection of 0.35 in. Column #6T-SG1 achieved a maximum load of 861 kips with a maximum midheight horizontal deflection of 0.24 in. All three columns experienced sudden material failures near the middle half of the column, which can be seen in Figures 2.17 through 2.20. As seen in the figures, the failure modes of these columns included compressive rupture of the longitudinal GFRP bars, tensile rupture of the GFRP-spiral, and compressive buckling of the longitudinal steel bars. The load-deflection and stress-strain curves for each of these three columns are shown in Figures 2.21 through 2.26 with a comparison of all three shown in Figures 2.27 and 2.28.

#### 2.4.3 Tall Columns Loaded with 4 in. Eccentricity

Three tall columns were tested under axial compressive load with 4 in. eccentricity. Figure 2.16 shows the typical tall column setup in the testing frame. These columns are identified as #7T-DB4 (both steel and GFRP longitudinal bars), #8T-SS4 (steel longitudinal bars), and #9T-SG4 (GFRP longitudinal bars). Column #7T-DB4 achieved a maximum load of 213 kips with a maximum midheight horizontal deflection of 2.50 in. Column #8T-SS4 achieved a maximum load of 206 kips with a maximum midheight horizontal deflection of 2.24 in. Column #9T-SG4 achieved a maximum load of 150 kips with a maximum midheight horizontal deflection of 2.82 in. All three columns experienced stability-type, buckling failures due to the large eccentricity with

the concrete cover on the compressive side breaking away near the middle half of the column as shown in Figures 2.29 through 2.33. There was much less damage to the reinforcement as compared to the other tests due to the fact that this was a stability failure. It was interesting to note that once the load was removed, all three columns rebounded nearly to their original shape, with the all-GFRP column (#9T-SG4) rebounding almost entirely to the vertical position (Figure 2.30).

The load-deflection and stress-strain curves for each of these three columns are shown in Figures 2.34 through 2.39 with a comparison of all three shown in Figures 2.40 and 2.41. The erratic curves of column #8T-SS4 shown in Figures 2.36 and 2.37 were caused by a malfunction of the testing equipment. At a load of about 140 kips it was observed that the load mechanism lost power due to a broken connection to the power source. When the connection was restored, the loading ram tried to instantly catch up to the programmed total deflection causing an instant surge of load and failure of the column.

## 2.5 Experimental Summary

In general, the tall columns with two layers of reinforcement outperformed the tall columns with just one layer of reinforcement. Table 2.2 provides a summary of the test results. It is interesting to note that in the case of 1 in. eccentricity the GFRP reinforced column #6T-SG1 outperformed the steel reinforced column #5T-SS1 in terms of both axial load and maximum horizontal deflection. In the case of short columns, the type and amount of reinforcement had a much smaller influence on the overall load capacity. The tall columns with two sets of longitudinal bars (GFRP and steel), #4T-DB1 and #7T-

DB4, were of particular interest in this study. It was expected that all-GFRP reinforced columns would experience a more brittle failure than those that had at least some steel reinforcement. This was the case with the all-GFRP reinforced columns #3S-SG0 and #6T-SG1, which had small load eccentricities and experienced material-type failures with the columns essentially being severed into two pieces. This was because all the GFRP longitudinal bars and GFRP-spiral had fully ruptured at the point of failure. The concept behind the doubly reinforced columns is that it would provide an inner, central core of steel bars to provide ductility in the case of failure due to lateral loads, while utilizing the corrosive resistant GFRP bars together with the outer GFRP-spiral toward the face of the column. As was observed, the doubly reinforced columns, which had small load eccentricities, did retain some semblance of ductility in that the pieces of column on either side of the failure were held together with the steel reinforcement. In contrast, however, as mentioned in the previous section, the all-GFRP column that had the larger load eccentricity interestingly incurred almost no permanent deformation once the load was removed as seen in Figure 2.30.

The axial compression load capacities of the doubly reinforced tall columns exceeded those having a single layer of reinforcement of either steel or GFRP longitudinal bars by at least 3%. However, the axial load capacity of the doubly reinforced short column unexpectedly achieved less than 92% the capacity of either of the columns with single layers of reinforcement. This appeared to be attributed to a construction defect from the use of a plastic rebar spacer strip that caused a localized weakness and allowed a portion of concrete cover to prematurely break off prior to full failure of the column as shown in Figures 2.8(a) and 2.12. For the concentric and 1 in.

eccentric loading conditions, the all-GFRP columns achieved a 1% to 7% increased load capacity over their counterpart columns having steel longitudinal bars. The short columns with concentric load achieved an average of 70% greater load capacity over the tall columns with 1 in. eccentric load, and the tall columns with 1 in. eccentric load achieved an average of 363% greater load capacity over the tall columns with 4 in. eccentric load.

The tall columns with a 1 in. eccentric loading condition had an average horizontal deflection of 0.29 in. It is interesting to note, however, that as seen in the load-deflection curves of Figure 2.27, after a very short period of positive deflection a reversal occurs, and the columns undergo a substantial period of negative deflection until about a load of 500 to 600 kips axial load. At this point the load is large enough that with its small eccentricity it can produce a dominant bending moment to influence the remaining deflection of the column to occur in the expected positive direction. This can be attributed to limitations and imperfections of the test setup to properly simulate a true 1 in. eccentric loading condition. The eccentricity is small enough that as the load is applied two different scenarios occur. First, when the load is initiated and begins to increase in magnitude, the metal plates distributing the load from the loading frame to the column begin to get firmly seated in place, and any inconsistencies between perfectly parallel interfaces (i.e., steel-plate-to-steel-plate or steel-plate-to-column) can cause the column to try to initially deflect in different directions. Second, the thick bearing plates on the top and bottom of the column can actually provide a medium of load distribution such that some of the load is actually being transferred to the opposite side of the load eccentricity, especially for small eccentricities (such as 1 in.). As a result, for a period of

time the location of the load the column is subjected to may actually hover on either side of 0 in. eccentricity until the load is large enough to dominantly provide the load on the intended side. In Chapter 4 this is analyzed in further detail in which it is determined that there was likely a loss of approximately 0.4 in. of actual horizontal deflection due to these effects. With this in consideration, it is estimated that the adjusted average horizontal deflection of these columns was 0.69 in.

The tall columns with a 4 in. eccentric loading condition had an average horizontal deflection of 2.52 in. The eccentricity effects as described in the previous paragraph likely had some influence on the overall horizontal deflection of these columns but to a much lesser degree due to the considerably larger eccentricity. Chapter 4 provides additional discussion on this topic. This increase in eccentricity of approximately 300% produced a 265% increase of horizontal deflection over the adjusted average horizontal deflection of the tall columns with a 1 in. eccentric loading, but also resulted in the columns with a 4 in. eccentricity achieving only 22% of the average axial load capacity of the columns with a 1 in. eccentricity.

The short columns and the tall columns with a 1 in. eccentric load experienced an average maximum compressive axial strain of 0.0031 in./in., while the tall columns with a 4 in. eccentric load experienced an average maximum compressive axial strain of 0.0034 in./in. The short columns did not have tensile axial strain, but the tall columns with a 1 in. eccentric load had an average maximum tensile axial strain of 0.00045 in./in., and the tall columns with a 4 in. eccentric load had an average maximum tensile axial strain of 0.0099 in./in. A point of interest is that the tall column with all-GFRP reinforcement loaded at 4 in. eccentricity, #9T-SG4, demonstrated the greatest flexibility

of all columns by producing the largest horizontal deflection of 2.83 in., the largest compressive axial strain of 0.0039 in./in., and the largest tensile axial strain of 0.0128 in./in.

Table 2.1: Summary of specimen construction and load eccentricity

Specimen	Height*	Outer Layer Reinforcement		Inner Layer Reinforcement		Load Eccen.
		Longitud. Bar	Spiral	Longitud. Bar	Spiral	
#1S-DB0	2'-6"	#5 GFRP	#3 GFRP	#4 Steel	#3 GFRP	0"
#2S-SS0	2'-6"	#4 Steel	#3 GFRP	N/A	N/A	0"
#3S-SG0	2'-6"	#5 GFRP	#3 GFRP	N/A	N/A	0"
#4T-DB1	12'-3"	#5 GFRP	#3 GFRP	#4 Steel	#3 GFRP	1"
#5T-SS1	12'-3"	#4 Steel	#3 GFRP	N/A	N/A	1"
#6T-SG1	12'-3"	#5 GFRP	#3 GFRP	N/A	N/A	1"
#7T-DB4	12'-3"	#5 GFRP	#3 GFRP	#4 Steel	#3 GFRP	4"
#8T-SS4	12'-3"	#4 Steel	#3 GFRP	N/A	N/A	4"
#9T-SG4	12'-3"	#5 GFRP	#3 GFRP	N/A	N/A	4"

\* All columns had a diameter of 12 in.

Table 2.2: Summary of max. load, horizontal deflection, and strain test results

Specimen	Max. Load (kips)	Max. Stress (psi)	Max. Horiz. Deflection (in.)	Max. Spiral Radial Strain at Failure (in./in.)	Max. Axial Strain at Failure (Compr. Side) (in./in.)	Max. Axial Strain at Failure (Tension Side) (in./in.)
#1S-DB0	1,376	12,167	N/A	0.004221	0.003742	N/A
#2S-SS0	1,498	13,244	N/A	0.001201	0.00262	N/A
#3S-SG0	1,602	14,165	N/A	0.000783	0.003038	N/A
#4T-DB1	925	8,181	0.28	0.000656	0.003036	-0.000197
#5T-SS1	850	7,517	0.35	0.000424	0.003175	-0.000752
#6T-SG1	861	7,609	0.24	0.000482	0.003042	-0.000406
#7T-DB4	213	1,880	2.50	0.000627	0.003411	-0.009109
#8T-SS4	206	1,818	2.24	0.000689	0.003079	-0.007688
#9T-SG4	150	1,322	2.83	0.001040	0.003856	-0.012788

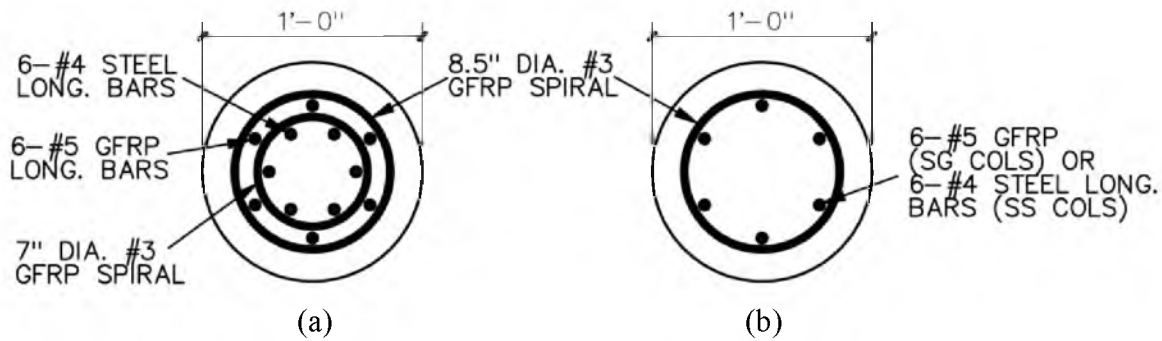


Figure 2.1: Reinforcement of 12 in. diameter concrete columns:  
 (a) type DB – double layer; (b) type SS and SG – single layer

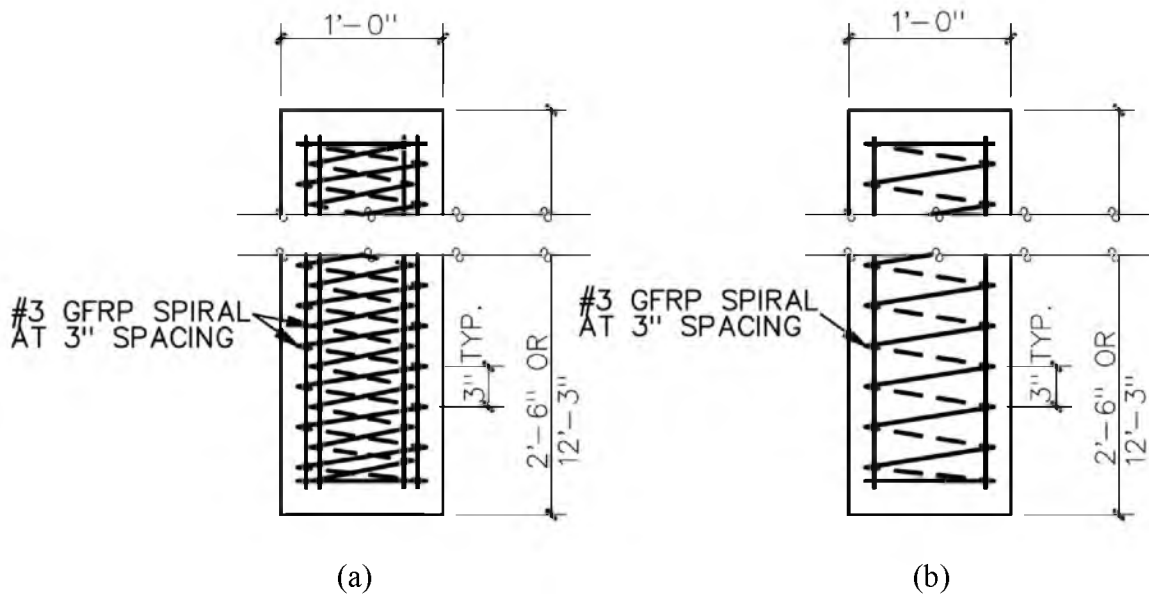
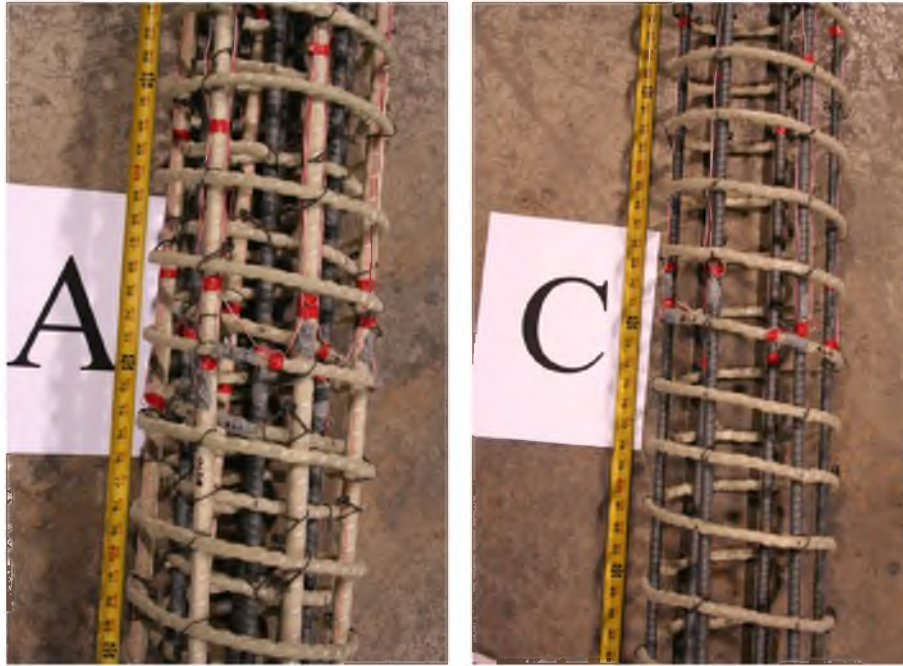
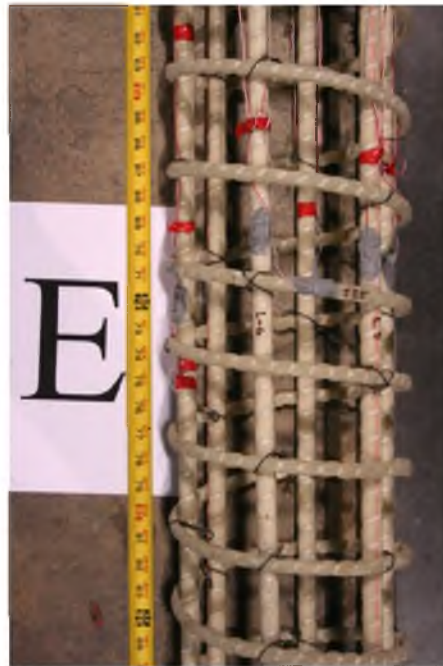


Figure 2.2: Elevation of 12 in. diameter concrete columns:  
 (a) type DB – double layer; (b) type SS and SG – single layer



(a)

(b)



(c)

Figure 2.3: Typical strain gauge placement on column reinforcing bars:  
(a) column #4T-DB1; (b) column #5T-SS1; (c) column #6T-SG1

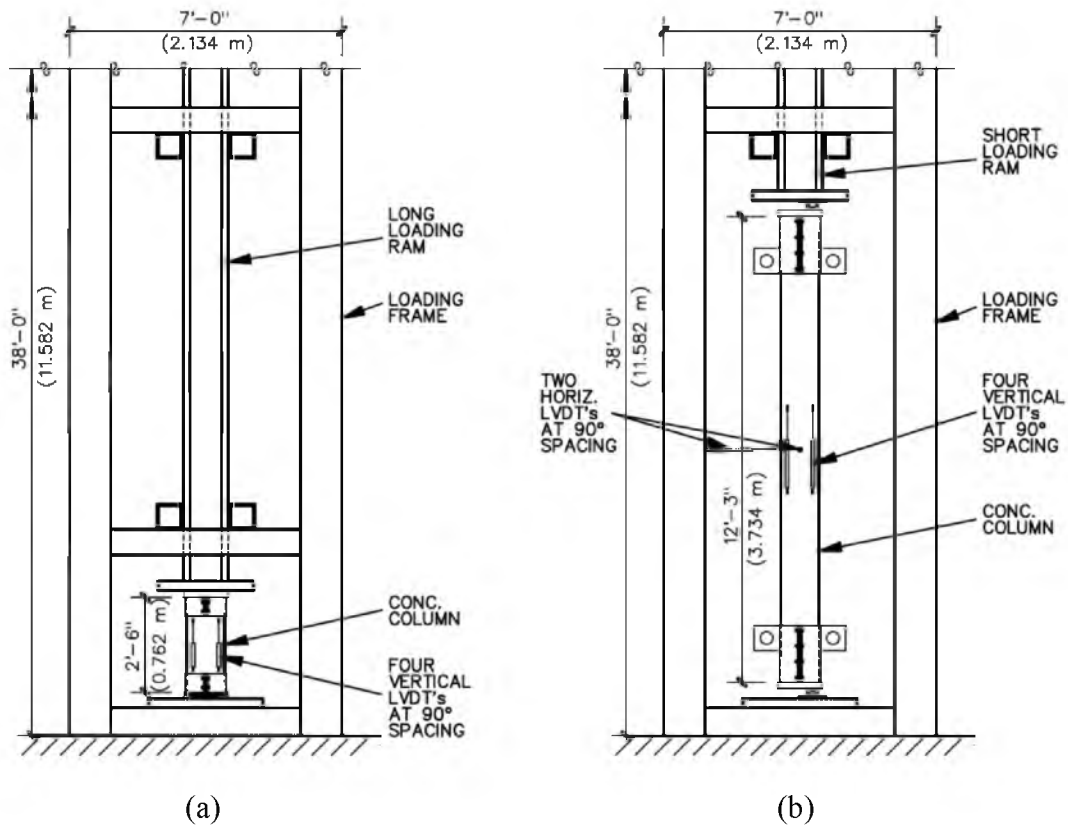


Figure 2.4: Column testing setup: (a) short column; (b) tall column

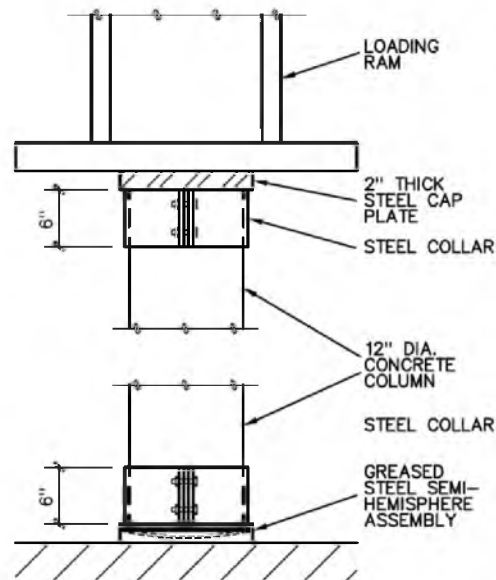


Figure 2.5: Short column setup for concentric loading condition

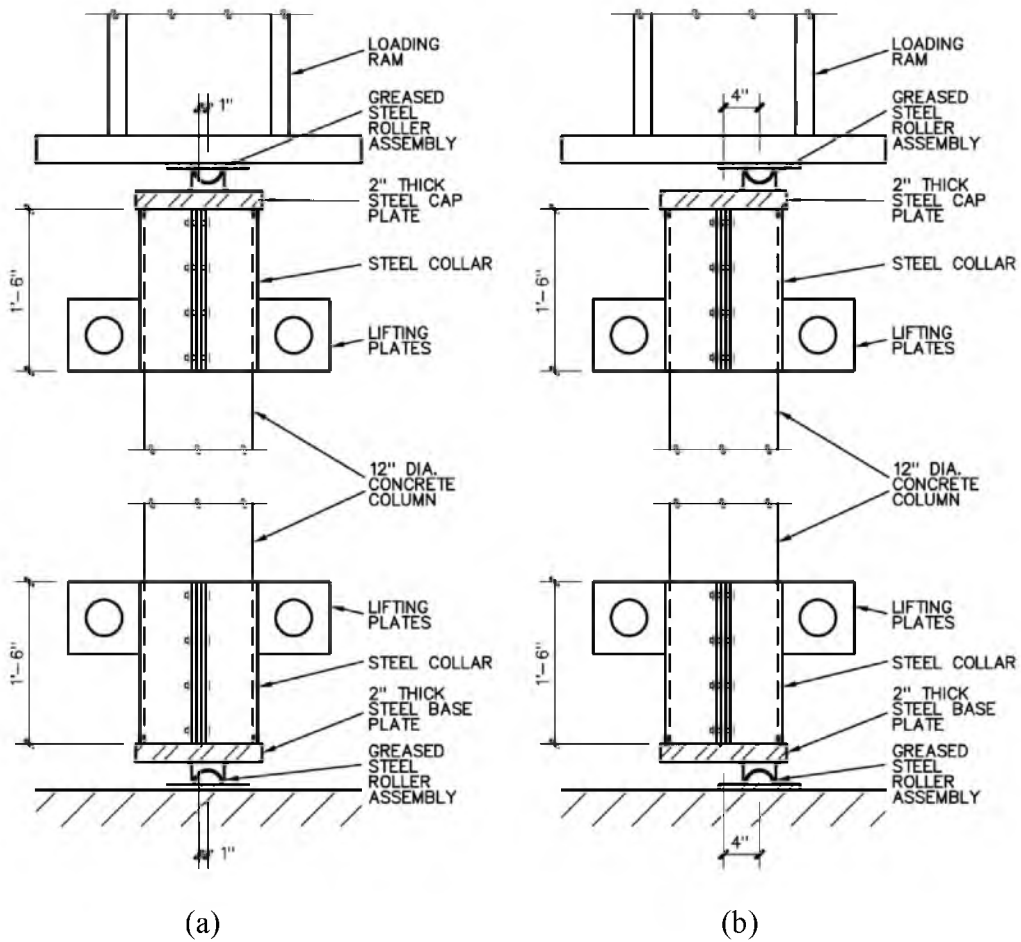


Figure 2.6: Tall column setup for eccentric loading condition:  
 (a) 1 in. eccentricity; (b) 4 in. eccentricity

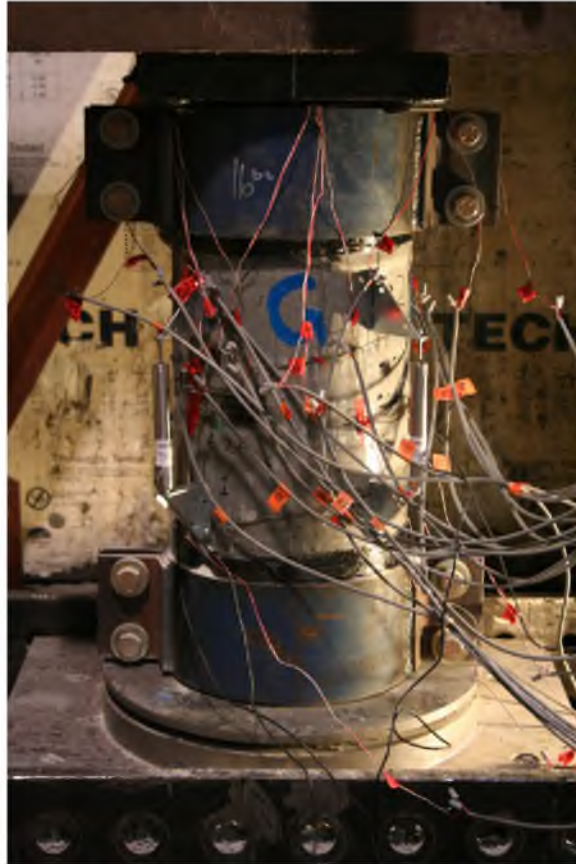


Figure 2.7: Typical short column setup (column #1S-DB0 shown)



(a)

(b)

(c)

Figure 2.8: Short columns tested to failure (concentric load):  
(a) column #1S-DB0; (b) column #2S-SS0; (c) column #3S-SG0



Figure 2.9: Failure details of column #1S-DB0



Figure 2.10: Failure details of column #2S-SS0



Figure 2.11: Failure details of column #3S-SG0

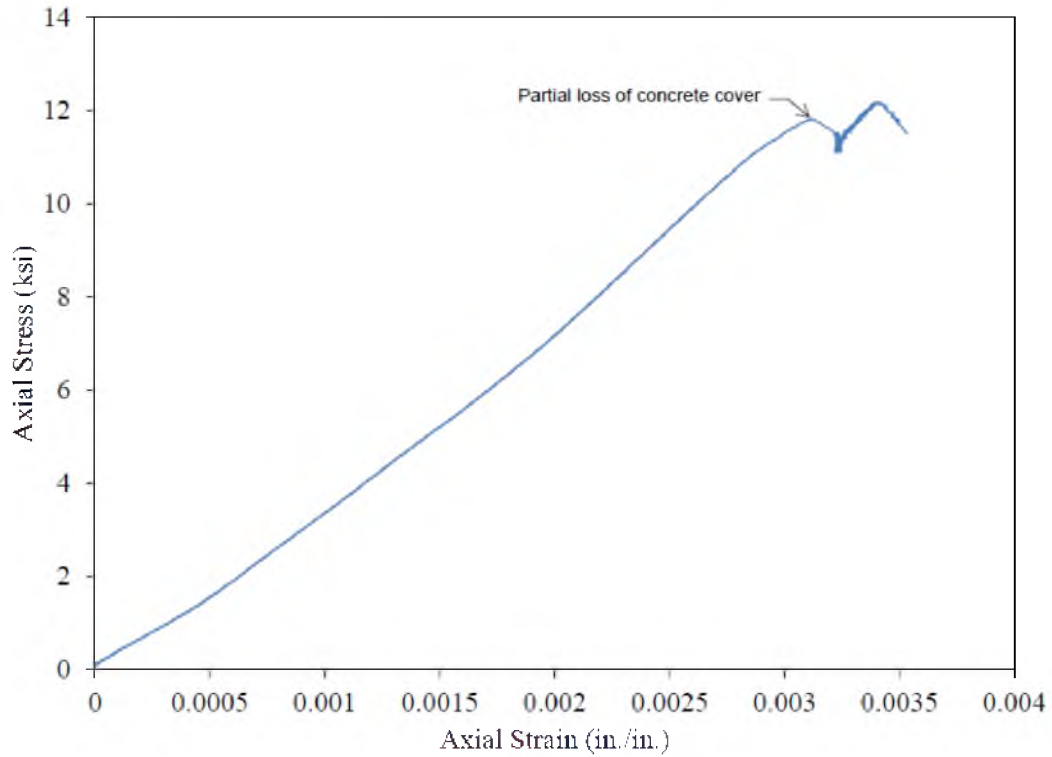


Figure 2.12: Axial stress vs. axial strain for column #1S-DB0

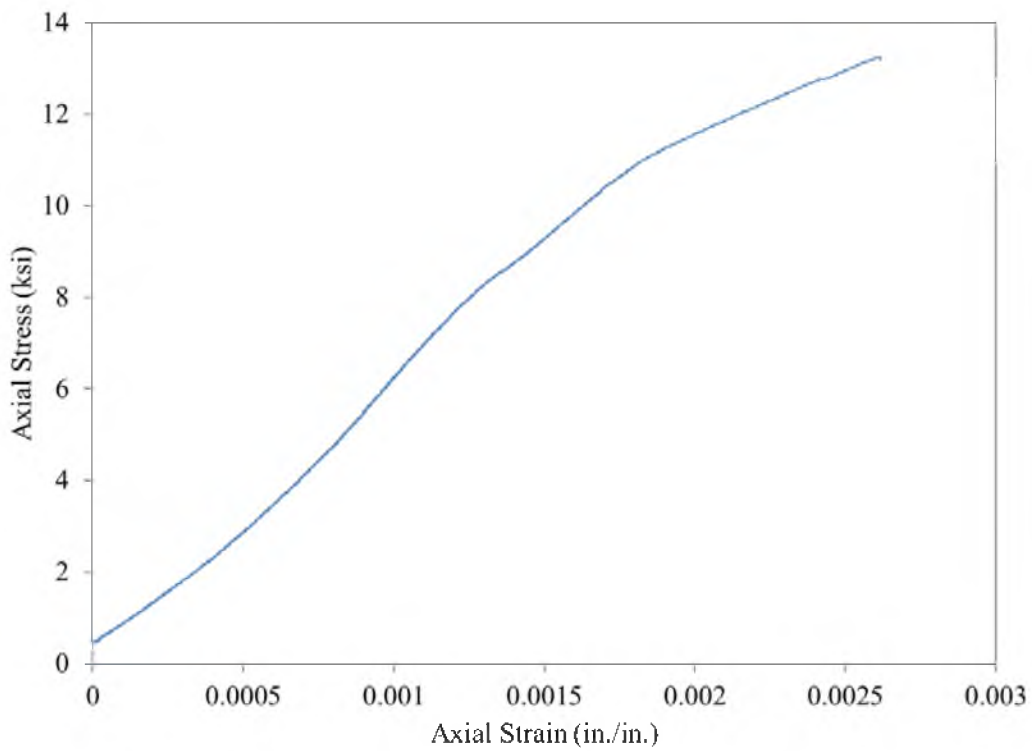


Figure 2.13: Axial stress vs. axial strain for column #2S-SS0

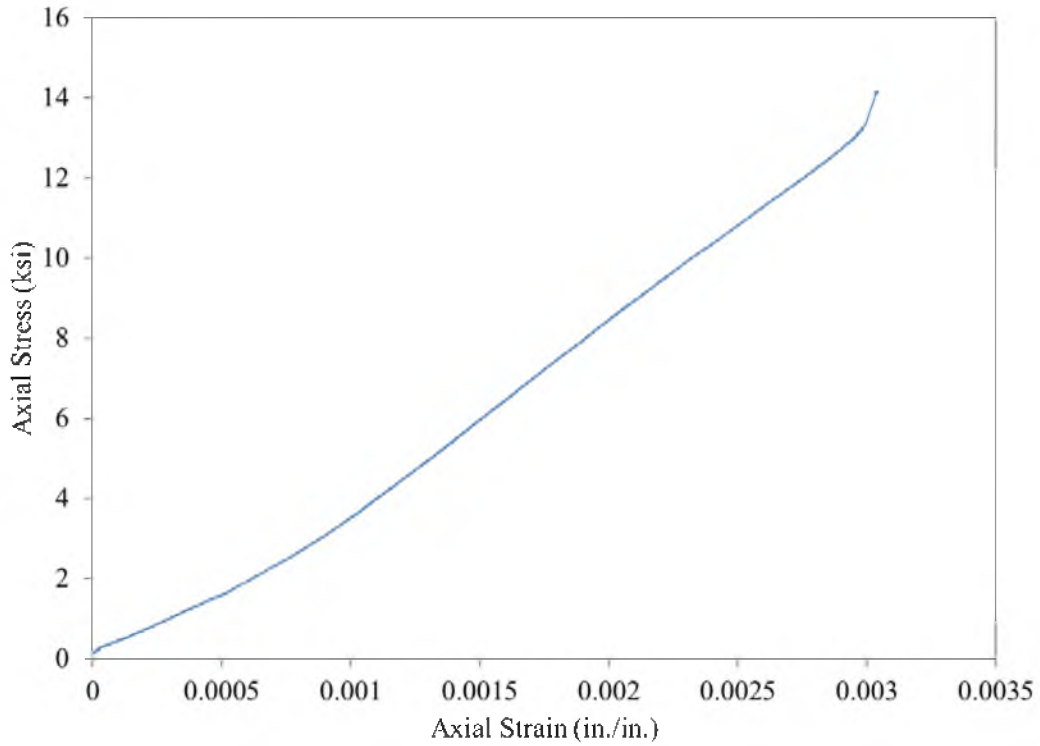


Figure 2.14: Axial stress vs. axial strain for column #3S-SG0

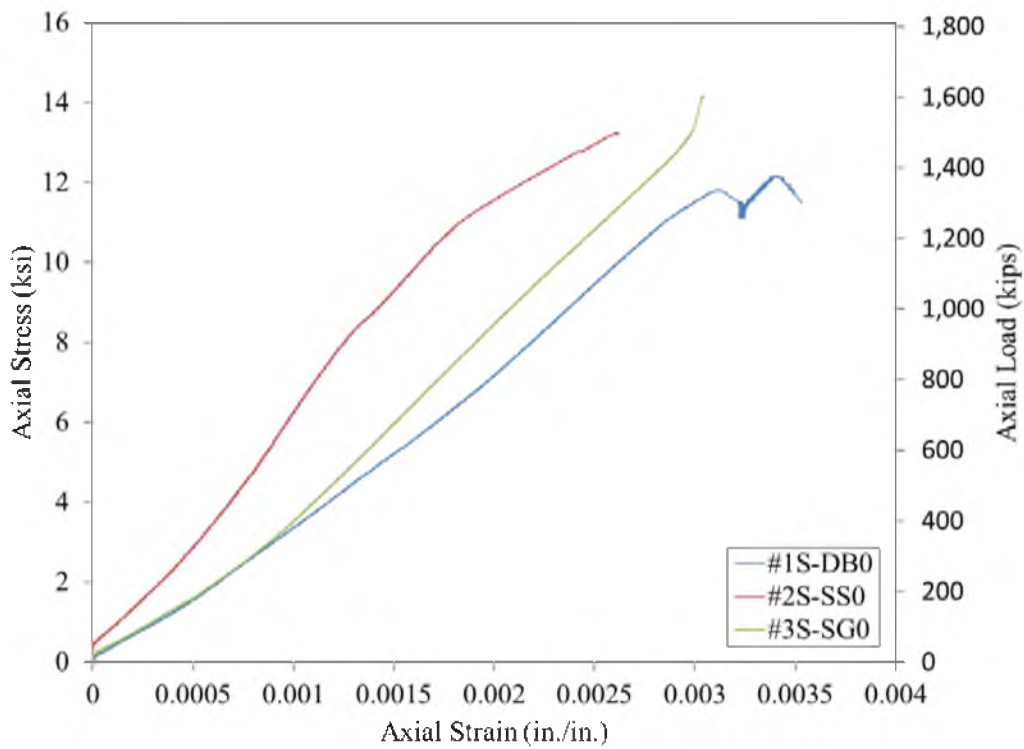
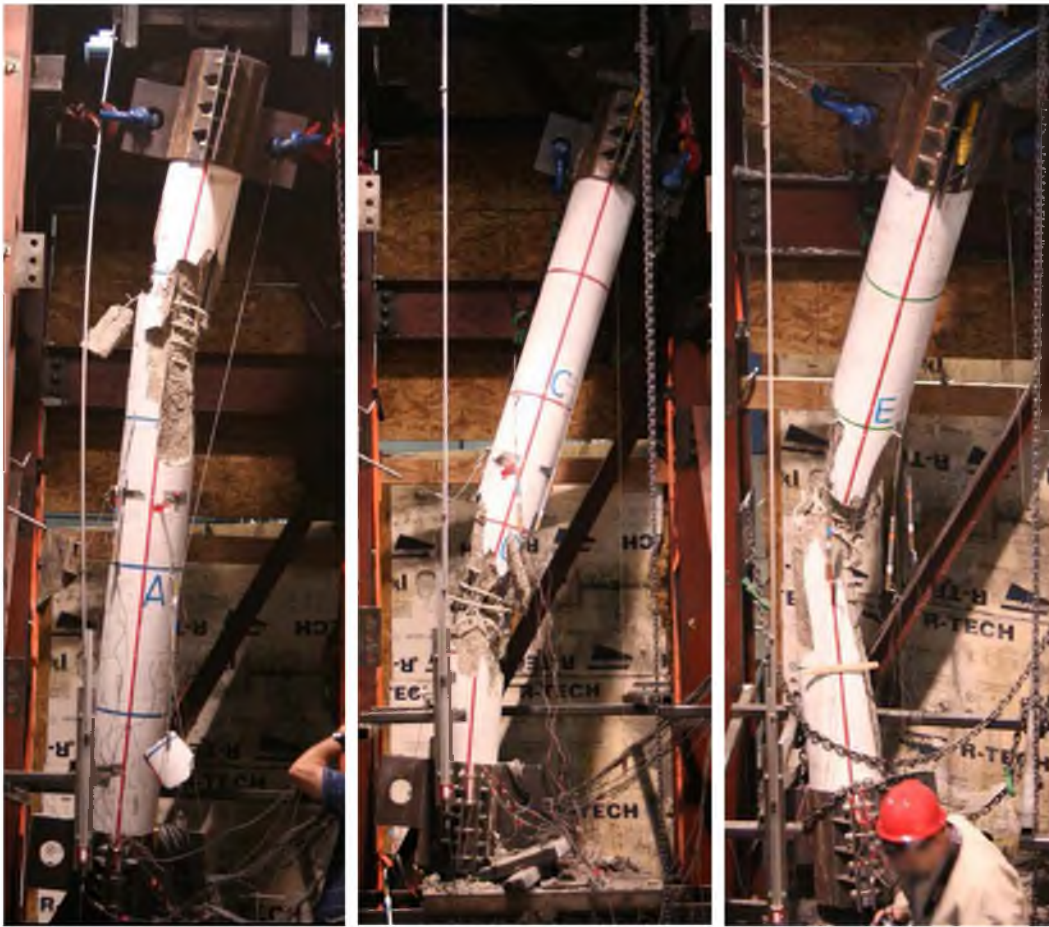


Figure 2.15: Comparison of axial stress vs. axial strain for all short columns



Figure 2.16: Typical tall column setup (column #4T-DB1 shown)



(a)

(b)

(c)

Figure 2.17: Tall columns tested to failure (1 in. eccentricity):  
(a) column #4T-DB1; (b) column #5T-SS1; (c) column #6T-SG1



Figure 2.18: Failure details of column #4T-DB1



Figure 2.19: Failure details of column #5T-SS1



Figure 2.20: Failure details of column #6T-SG1

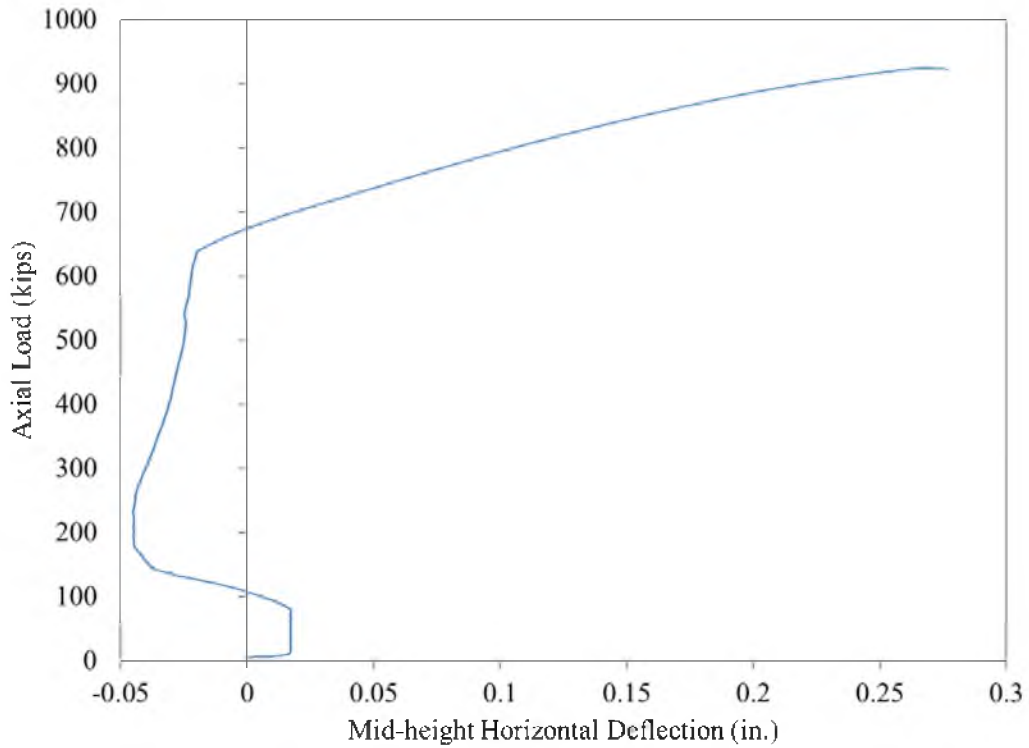


Figure 2.21: Load-deflection curve for column #4T-DB1

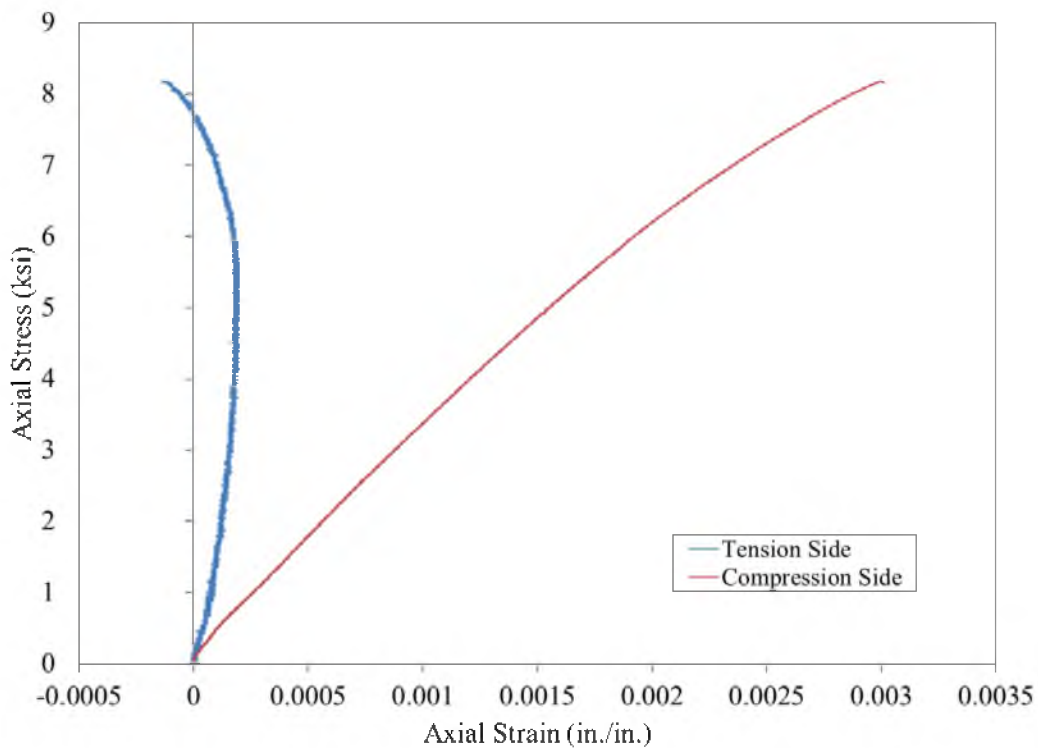


Figure 2.22: Axial stress vs. axial strain curve for column #4T-DB1

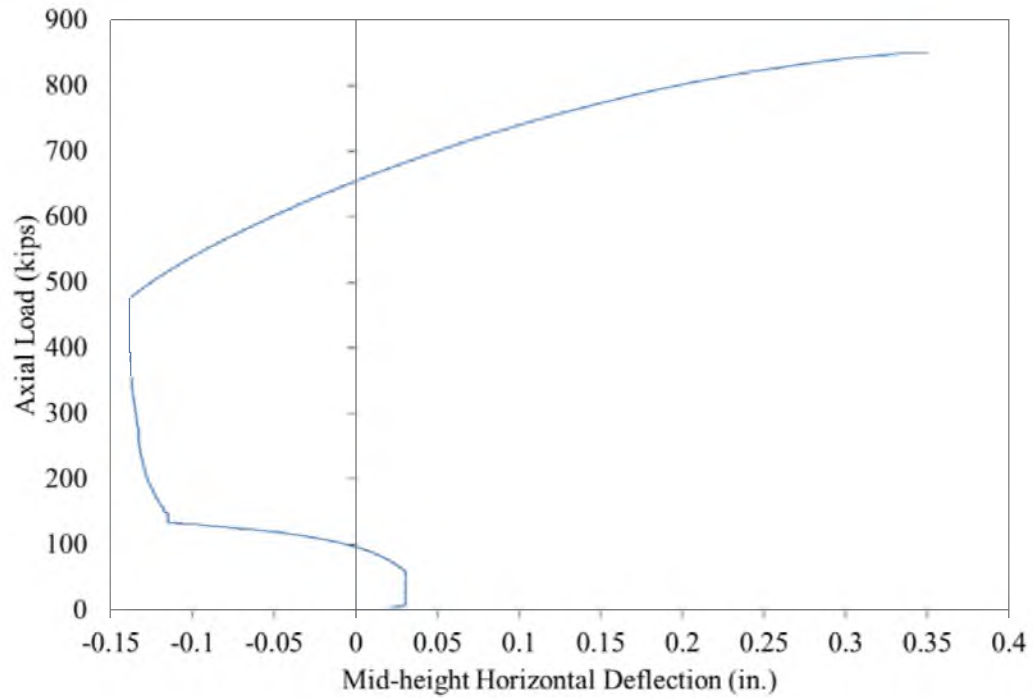


Figure 2.23: Load-deflection curve for column #5T-SS1

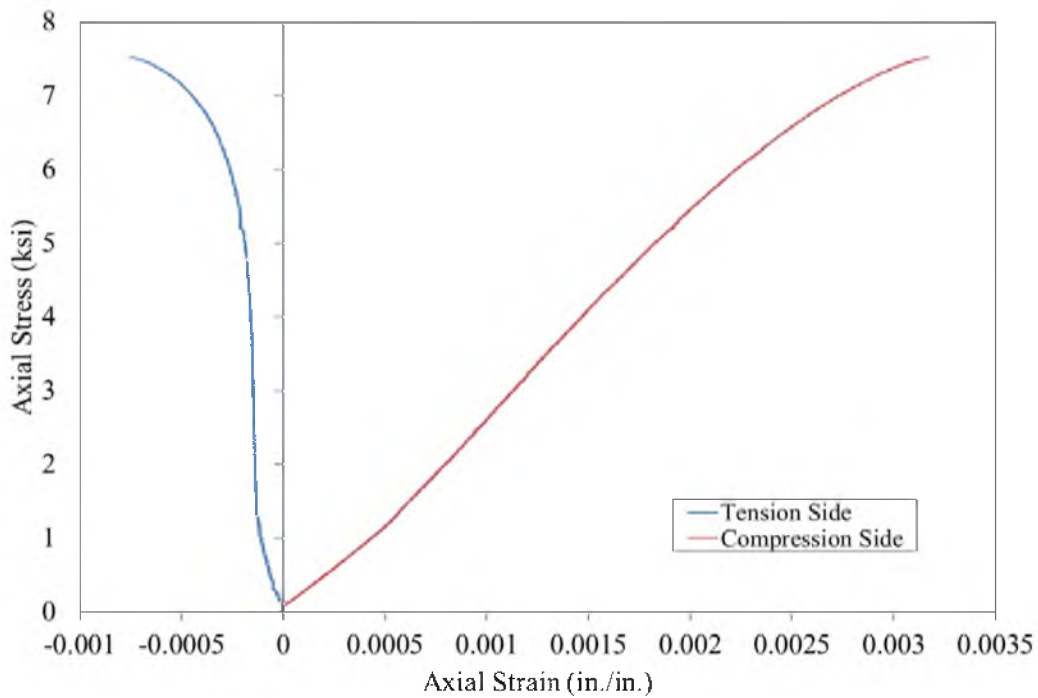


Figure 2.24: Axial stress vs. axial strain curve for column #5T-SS1

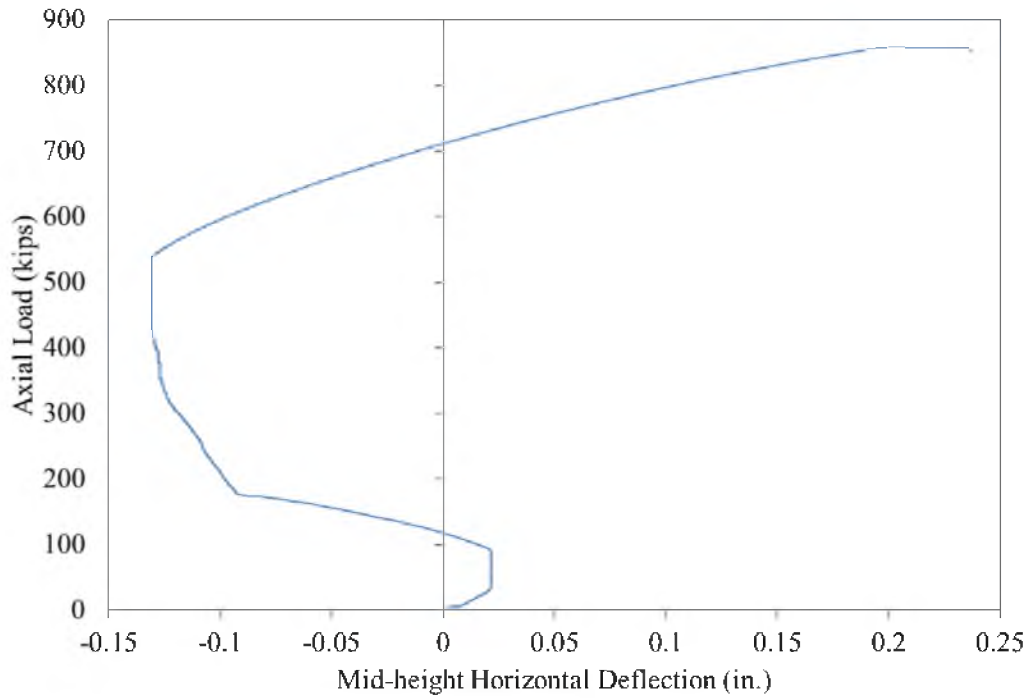


Figure 2.25: Load-deflection curve for column #6T-SG1

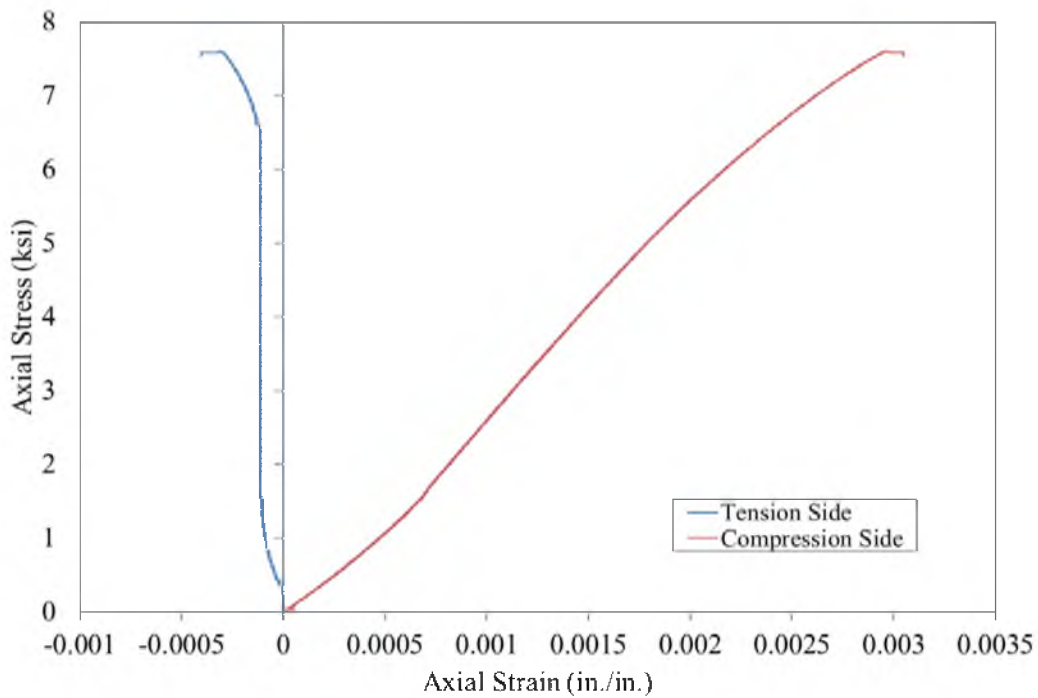


Figure 2.26: Axial stress vs. axial strain curve for column #6T-SG1

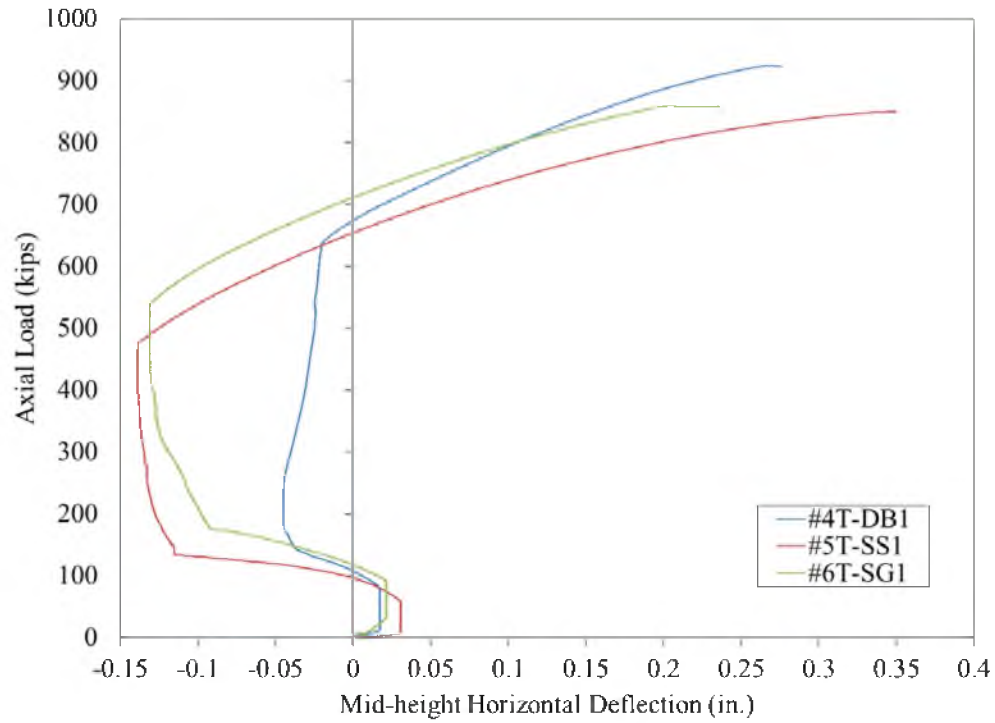


Figure 2.27: Comparison of load-deflection curves for columns #4T-DB1, #5T-SS1, and #6T-SG1

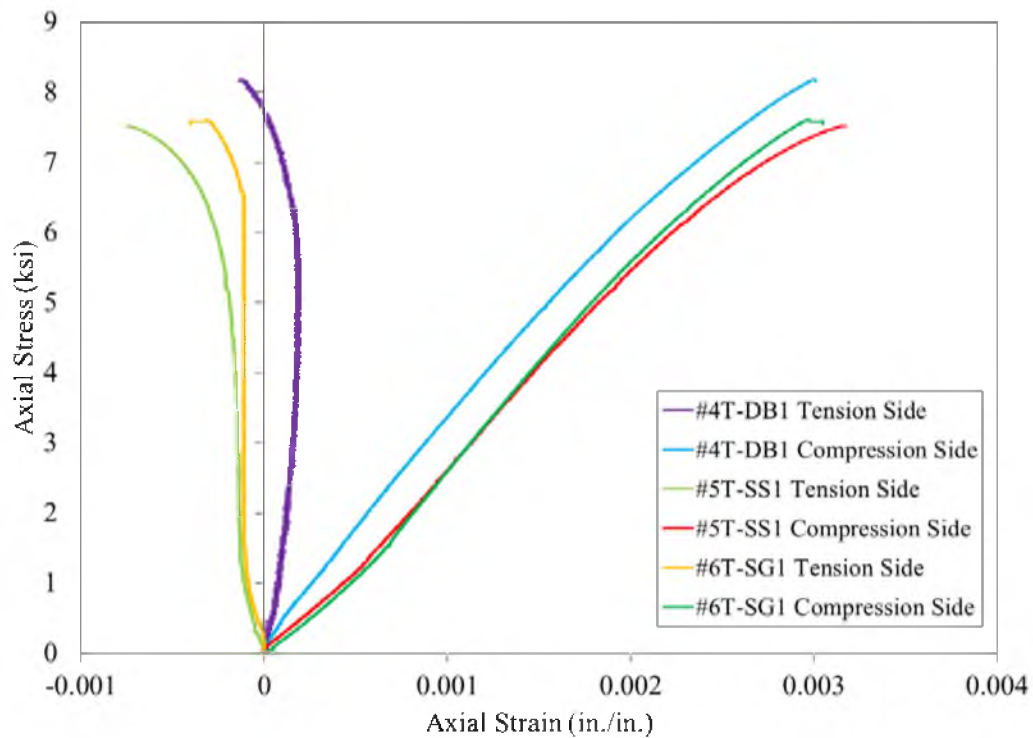


Figure 2.28: Comparison of axial stress vs. axial strain curves for columns #4T-DB1, #5T-SS1, and #6T-SG1



(a)

(b)

Figure 2.29: Tall columns tested to failure (4 in. eccentricity):  
(a) column #7T-DB4; (b) column #8T-SS4

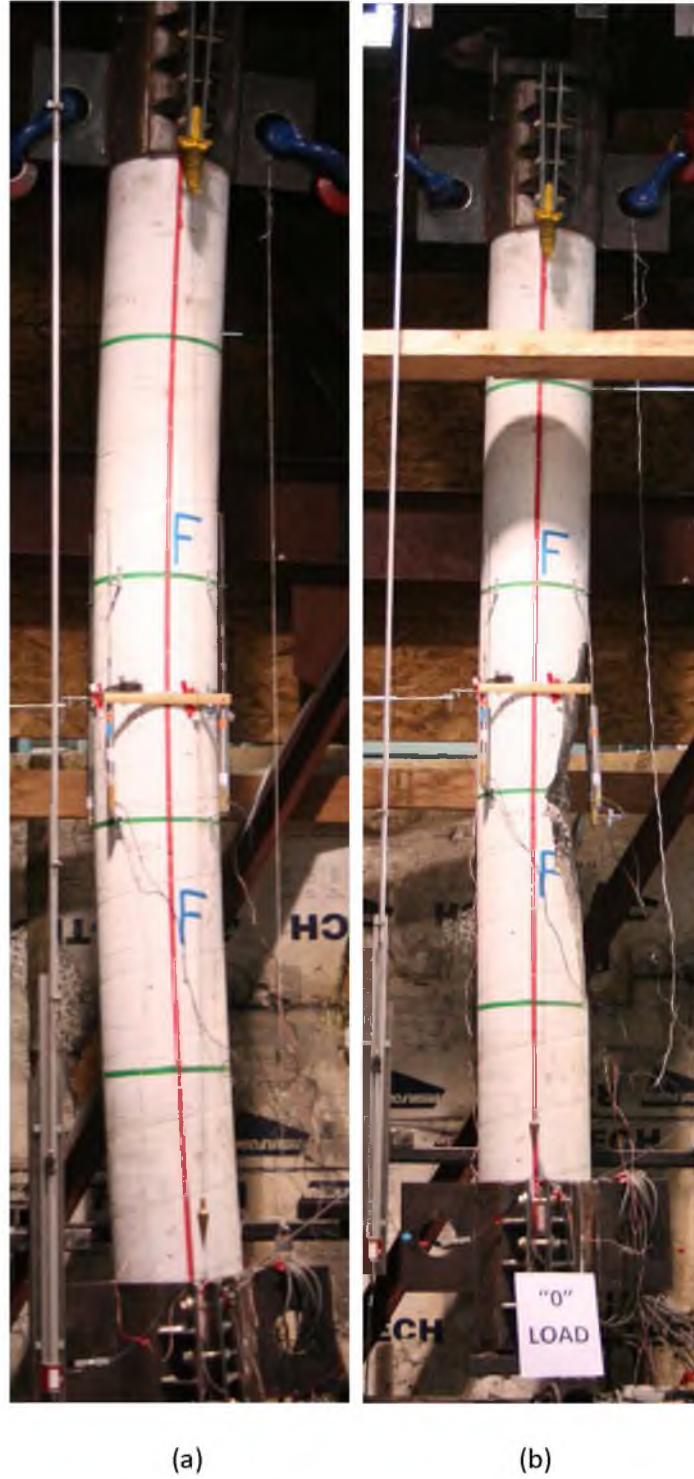


Figure 2.30: Tall columns tested to failure (4 in. eccentricity):  
(a) column #9T-SG4 just prior to failure showing curvature;  
(b) column #9T-SG4 just after failure showing rebound at no axial load



Figure 2.31: Failure details of column #7T-DB4



Figure 2.32: Failure details of column #8T-SS4



Figure 2.33: Failure details of column #9T-SG4

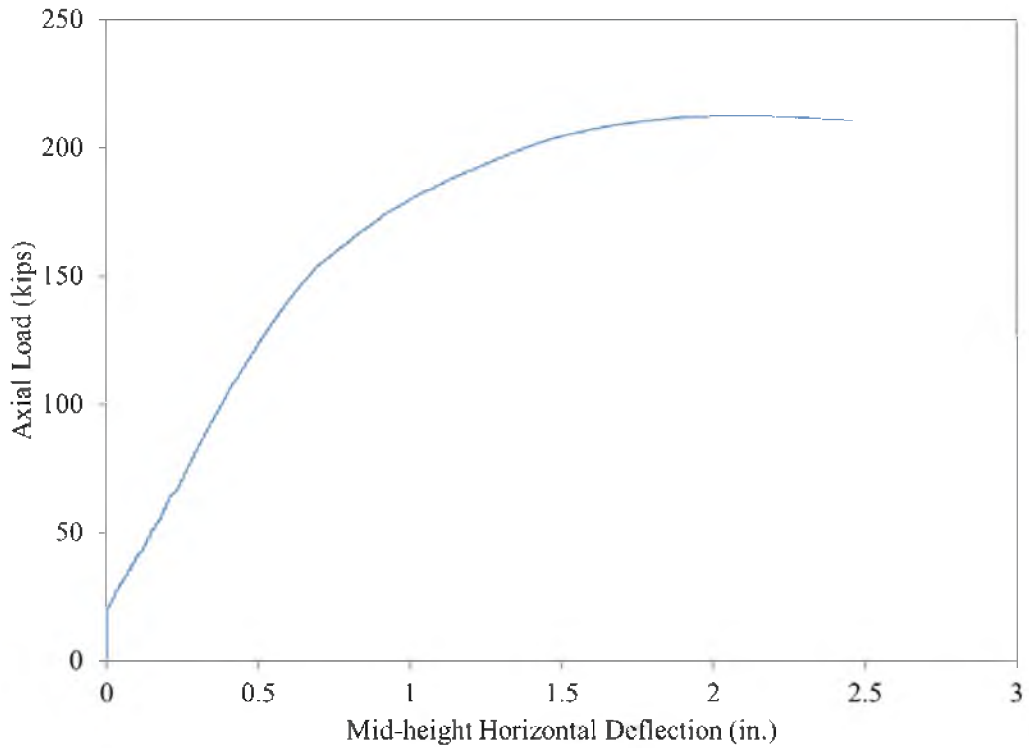


Figure 2.34: Load-deflection curve for column #7T-DB4

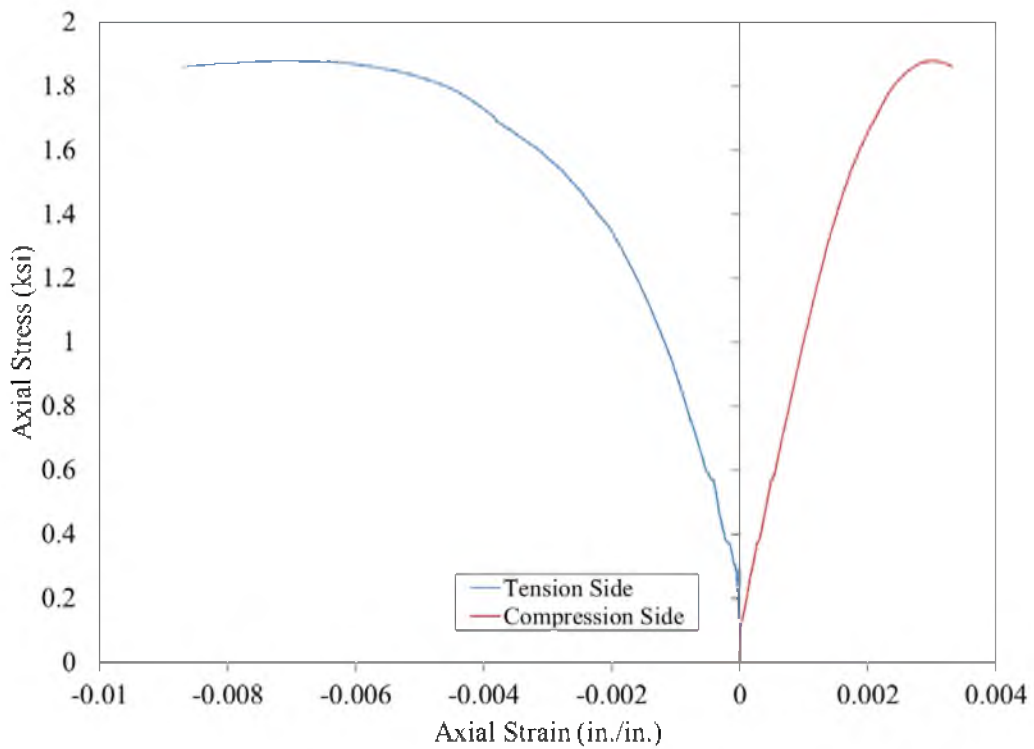


Figure 2.35: Axial stress vs. axial strain curve for column #7T-DB4

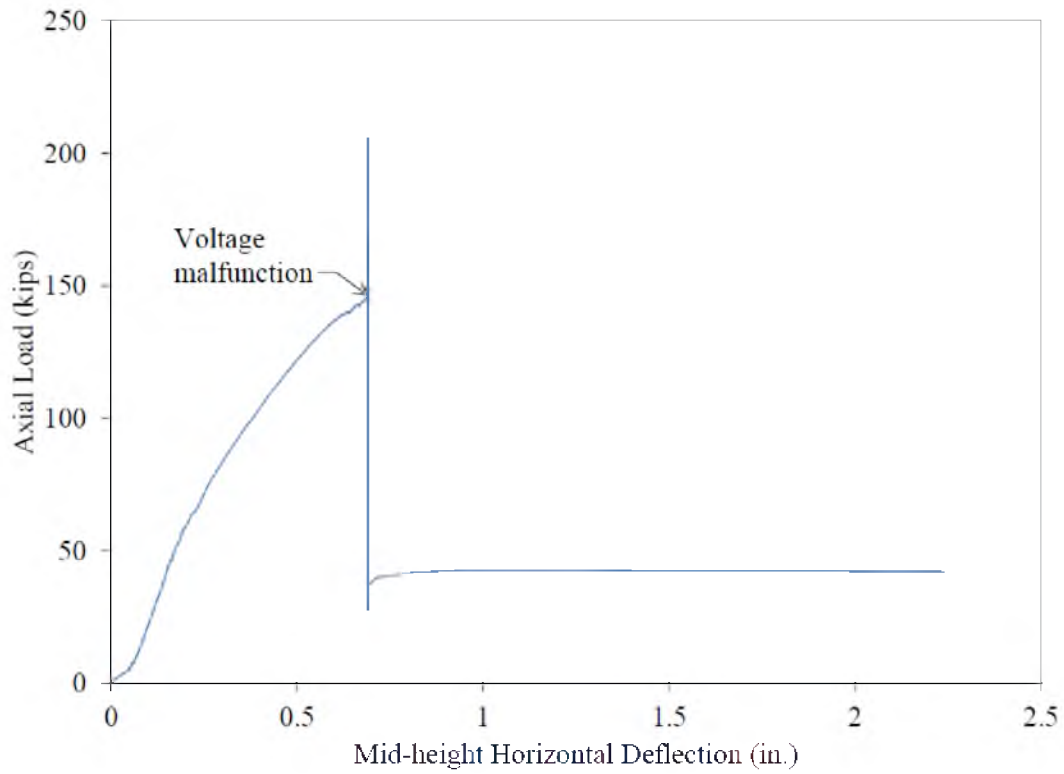


Figure 2.36: Load-deflection curve for column #8T-SS4

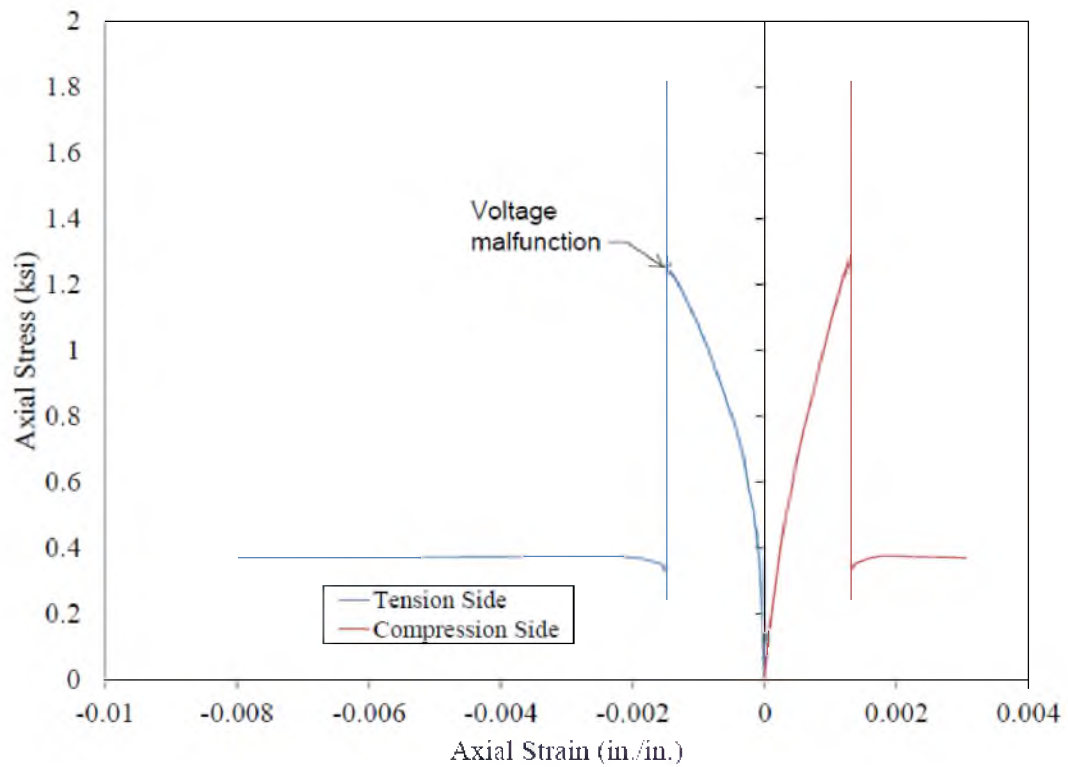


Figure 2.37: Axial stress vs. axial strain curve for column #8T-SS4

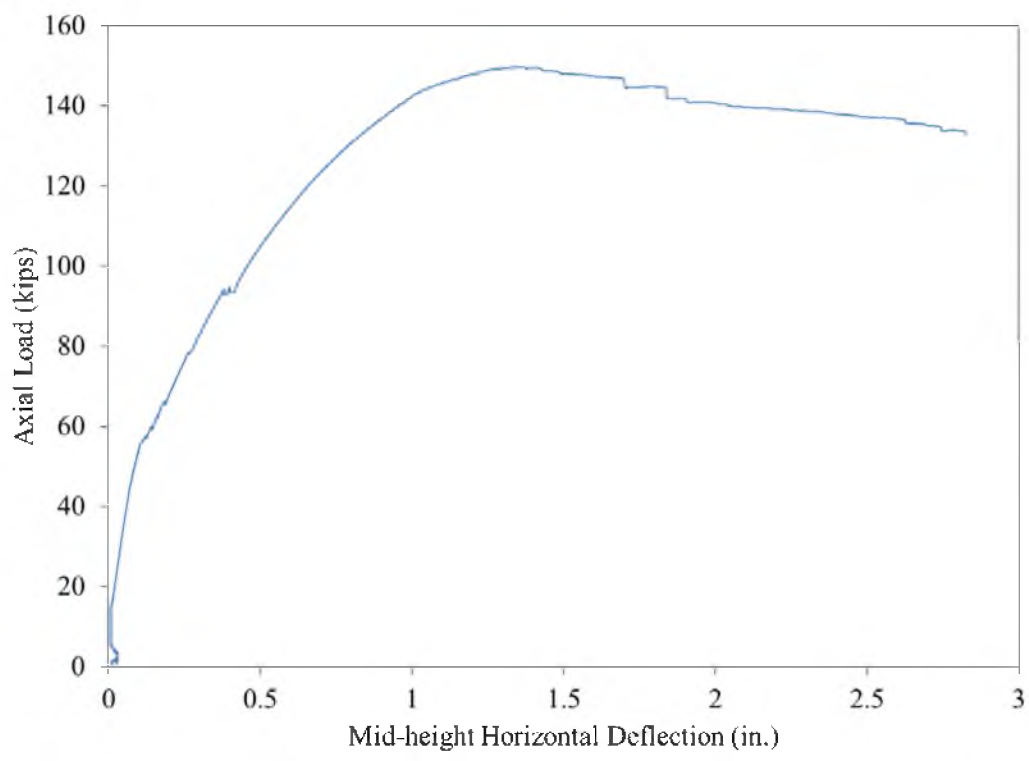


Figure 2.38: Load-deflection curve for column #9T-SG4

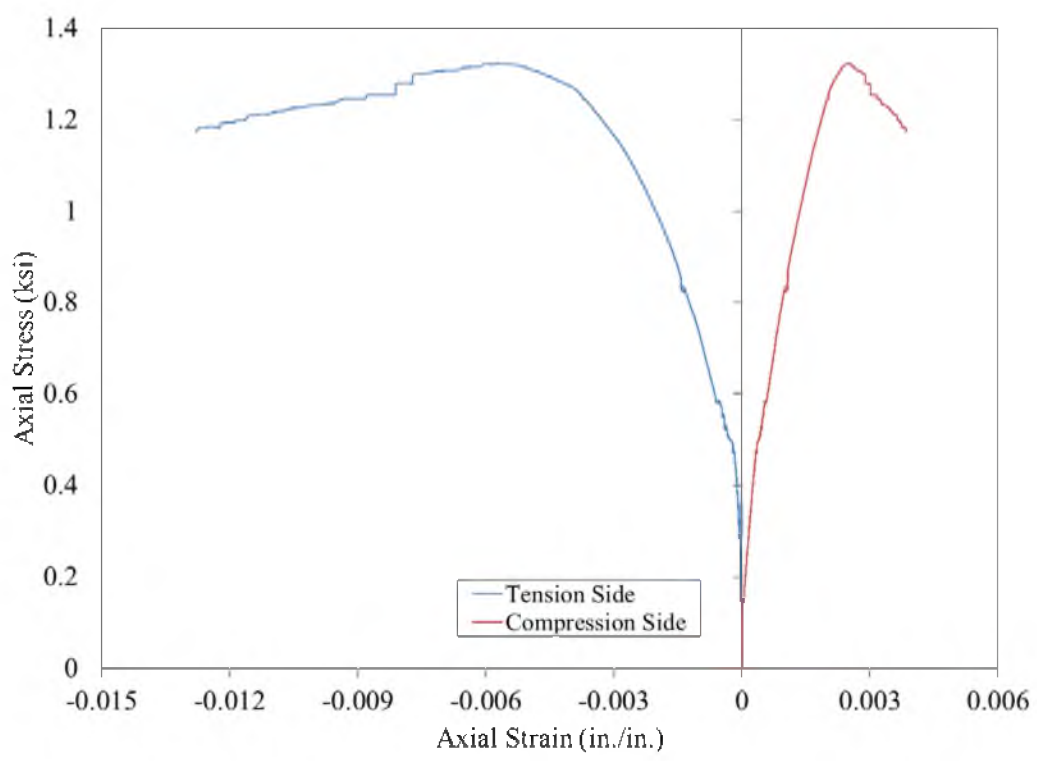


Figure 2.39: Axial stress vs. axial strain curve for column #9T-SG4

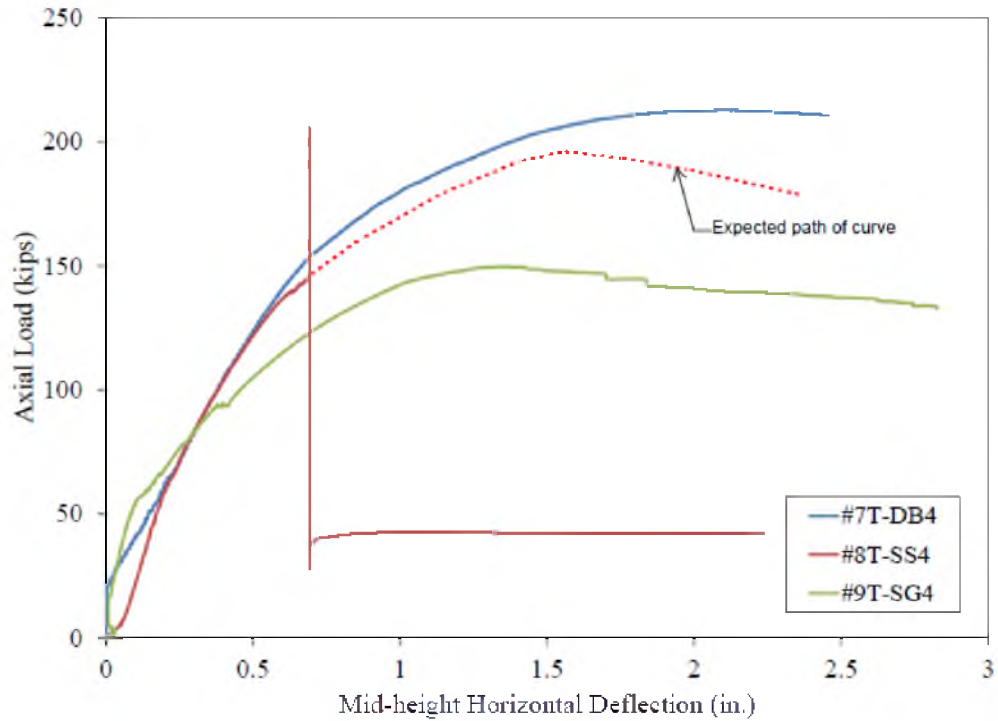


Figure 2.40: Comparison of load-deflection curves for columns #7T-DB4, #8T-SS4, and #9T-SG4

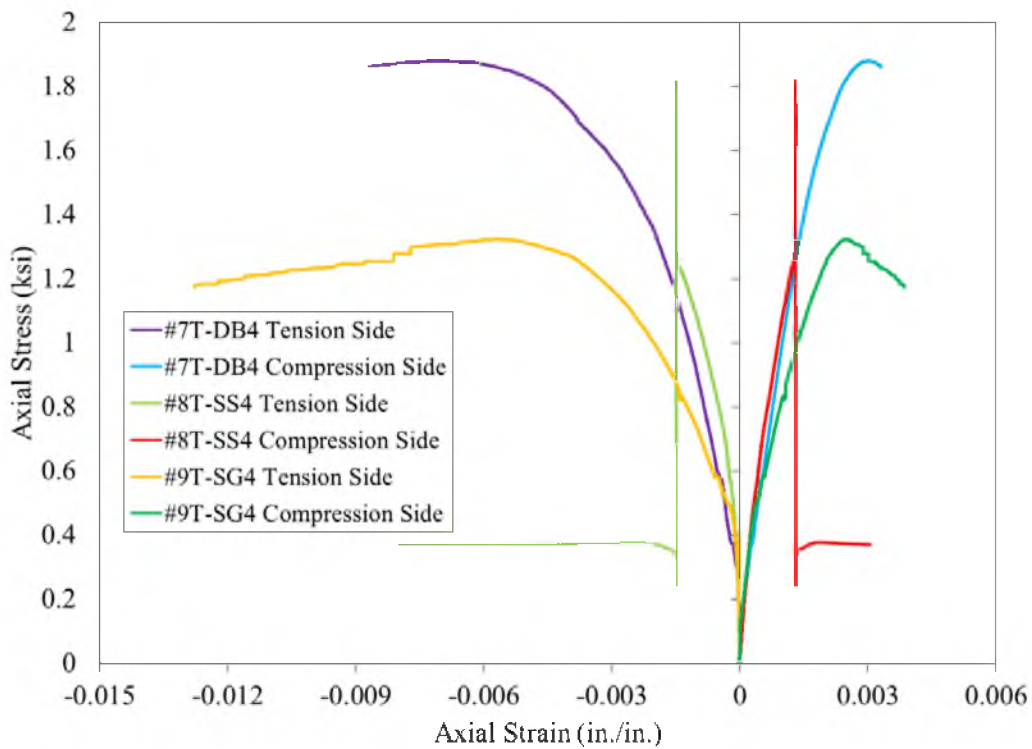


Figure 2.41: Comparison of axial stress vs. axial strain curves for columns #7T-DB4, #8T-SS4, and #9T-SG4

## CHAPTER 3

### ANALYTICAL CONFINEMENT MODEL FOR FRP-SPIRAL-CONFINED CONCRETE

An analytical confinement model has been developed and is proposed for describing the axial strength and stress-strain relationship for FRP-spiral-confined circular columns based on a modified Willam and Warnke (1975) plasticity model. It has been shown that the Willam-Warnke five-parameter failure criterion can provide good representation of experimental results over a wide range of stress combinations to define the ultimate stress values for concrete. In past years many have attempted to use the Mander et al. (1988) model to represent the behavior of FRP-confined concrete columns but in many cases were found to be lacking because it was solely based on the presence of a constant confining stress throughout the loading progression. This is reasonable for steel-confined concrete where the steel yields but not so for FRP-confined concrete where the confining stress increases continuously in an elastic manner until failure. Yan and Pantelides (2006) proposed a confinement model for use with externally wrapped FRP-confined concrete that accounted for such elastic behavior utilizing the Willam-Warnke criterion and was found to provide reasonable representation of the confined concrete. The methodology used in the present study also incorporates such elastic behavior, which will be described in more detail in the following sections.

### 3.1 Plasticity Theory Overview

Only a brief overview of highlighted equations and concepts of the Willam-Warnke methodology are presented. Greater details of the plasticity model theory and its application with the five-parameter failure criterion are presented by Willam and Warnke (1975) and Yan (2005).

Concrete in confined concrete columns is subjected to confining pressure due to the hoop strains developed in the confining reinforcement. As a result, spiral-confined concrete subjected to an applied compression load is in a state of triaxial stresses. For purposes of the present study,  $\sigma_1$  represents the axial compressive stress applied on the specimen and  $\sigma_2$  and  $\sigma_3$  represent the confining stress in the x and y directions produced by the FRP confinement (with compressive stress being negative). These stresses can be depicted in a three-dimensional stress space as shown in Figure 3.1.

The straight line ON shown in Figure 3.1 makes the same angle with each of the coordinate axes and the state of stress for every point on this line is such that  $\sigma_1 = \sigma_2 = \sigma_3$ . As a result, every point on line OA corresponds to a hydrostatic state of stresses. It is also important to note that along this line the deviatoric stresses, which are defined as  $(2\sigma_1 - \sigma_2 - \sigma_3)/3$ , are equal to zero. Point P, having the stress component  $\sigma_1$ ,  $\sigma_2$  and  $\sigma_3$ , represents a point of an arbitrary state of stress. The stress vector OP can be broken into two components: component ON on the hydrostatic axis and component NP on the deviatoric plane which is perpendicular to the hydrostatic axis. Component ON relates to the mean normal stress, or hydrostatic stress,  $\sigma_a$ , which is expressed as

$$\sigma_a = \frac{\sigma_1 + \sigma_2 + \sigma_3}{3} \quad (3.1)$$

The length of stress vector ON is equal to  $|\sqrt{3}\sigma_a|$ . The length of stress vector NP on the deviatoric plane can be expressed as

$$\rho = \sqrt{3} \tau_{oct} \quad (3.2)$$

where  $\tau_{oct}$  is the octahedral shear stress, which can be expressed in terms of  $\sigma_1$ ,  $\sigma_2$  and  $\sigma_3$  as

$$\tau_{oct} = \frac{1}{3} \left[ (\sigma_1 - \sigma_2)^2 + (\sigma_2 - \sigma_3)^2 + (\sigma_3 - \sigma_1)^2 \right]^{1/2} \quad (3.3)$$

From the previous two equations,  $\rho$  can be rewritten as

$$\rho = \frac{1}{\sqrt{3}} \left[ (\sigma_1 - \sigma_2)^2 + (\sigma_2 - \sigma_3)^2 + (\sigma_3 - \sigma_1)^2 \right]^{1/2} \quad (3.4)$$

The mean shear stress  $\tau_a$  can be expressed using the shear stress vectors as (Willam and Warnke 1975; Chen and Han 1982)

$$\tau_a = \frac{1}{\sqrt{15}} \left[ (\sigma_1 - \sigma_2)^2 + (\sigma_2 - \sigma_3)^2 + (\sigma_3 - \sigma_1)^2 \right]^{1/2} \quad (3.5)$$

Therefore, from Eqs. (3.4) and (3.5), the relation between  $\tau_a$  and  $\rho$  is

$$\tau_a = \frac{1}{\sqrt{5}} \rho \quad (3.6)$$

The octahedral normal stress  $\sigma_{oct}$ , on the face of the octahedron, can be expressed as

$$\sigma_{oct} = \frac{\sigma_1 + \sigma_2 + \sigma_3}{3} \quad (3.7)$$

It is interesting to note that the quantity  $\sigma_{oct}$  is equal to the mean normal stress  $\sigma_a$ .

The projection of the deviatoric stress vector NP on a deviatoric plane is

represented in Figure 3.2, where  $\sigma_1'$ ,  $\sigma_2'$ , and  $\sigma_3'$  are the projections of axes  $\sigma_1$ ,  $\sigma_2$ , and  $\sigma_3$  shown in Figure 3.1, and NP is the projection of the deviatoric stress vector NP.

The angle  $\theta$  of a stress point on the deviatoric plane can be expressed as

$$\theta = \cos^{-1} \left( \frac{2\sigma_1 - \sigma_2 - \sigma_3}{\sqrt{2} [(\sigma_1 - \sigma_2)^2 + (\sigma_2 - \sigma_3)^2 + (\sigma_3 - \sigma_1)^2]^{1/2}} \right) \quad (3.8)$$

Based on the assumptions that concrete is an isotropic, hydrostatic-pressure dependent material, the general shape of an ultimate surface representing the failure criterion can be represented as depicted in Figure 3.3(a) with its cross-sectional shape in the deviatoric plane as depicted in Figure 3.3(b) and its meridians in the meridian plane as depicted in Figure 3.3(c). The ultimate stress surface cross-sections are the intersection curves between this surface and a deviatoric plane, which is perpendicular to the hydrostatic axis where  $\sigma_a$  is constant.

### 3.2 Willam and Warnke (1975) Five-Parameter Concrete Model

The Willam and Warnke (1975) five-parameter ultimate surface was utilized to develop the failure criterion used in the present study because it accounts for concrete under a state of multiaxial stresses. The ultimate stress values for a given stress ratio  $\sigma_1 : \sigma_2 : \sigma_3$  are defined by the ultimate surface, which is an upper bound of attainable states of stresses. These are not simply failure points but rather combinations of ultimate stresses or maximum stress values. It is essentially a combination of the Mohr-Coulomb shear strength criterion and the traditional Rankine maximum tensile strength criterion.

The normalized mean normal stress,  $\bar{\sigma}_a$ , and the normalized mean shear stress,

$\overline{\tau}_a$ , can be expressed as

$$\overline{\sigma}_a = \frac{\overline{\sigma}_a}{f'_{co}} \quad (3.9)$$

$$\overline{\tau}_a = \frac{\overline{\tau}_a}{f'_{co}} \quad (3.10)$$

where  $f'_{co}$  is the unconfined concrete strength.

Considering the projection of the ultimate surface on the meridian plane for which  $\overline{\sigma}_a$  is the X axis and  $\overline{\tau}_a$  is the Y axis and the assumption that both the compression meridian and the tensile meridian are parabolic functions of  $\overline{\sigma}_a$ , the following expressions can be derived for the tensile meridian  $\rho_t$

$$\overline{\tau}_a = a_0 + a_1 \overline{\sigma}_a + a_2 \overline{\sigma}_a^2 \quad (3.11)$$

and for compression meridian  $\rho_c$

$$\overline{\tau}_a = b_0 + b_1 \overline{\sigma}_a + b_2 \overline{\sigma}_a^2 \quad (3.12)$$

where  $a_0, a_1, a_2, b_0, b_1, b_2$  are material constants.

By utilizing the definitions of  $\rho_t$  and  $\rho_c$  and substituting Eqs. (3.6), (3.9), and (3.10) into Eqs. (3.11) and (3.12) the Willam-Warnke model can also be expressed for the tensile meridian  $\rho_t$  as

$$\frac{\rho_t}{\sqrt{5} f'_{co}} = a_0 + a_1 \overline{\sigma}_a + a_2 \overline{\sigma}_a^2 \quad (3.13)$$

and for compression meridian  $\rho_c$

$$\frac{\rho_c}{\sqrt{5}f'_{co}} = b_0 + b_1\overline{\sigma_a} + b_2\overline{\sigma_a}^2 \quad (3.14)$$

As shown from these equations, the Willam-Warnke model is determined by the six material coefficients  $a_0, a_1, a_2, b_0, b_1, b_2$ . As seen in Figure 3.3(c), the tensile and compression conditions must intersect at the same point on the normal mean stress (hydrostatic) axis, which means that  $a_0 = b_0$ . Consequently, the failure criterion of this model can be determined by five parameters (or material coefficients)  $a_0$  (or  $b_0$ ),  $a_1, a_2, b_1$ , and  $b_2$ . These material coefficients can then be determined such that the best-fit curves of  $\rho_t$  and  $\rho_c$  pass through a group of experimental points.

### 3.3 Axial Strength of FRP-Confined Concrete and the Modified Willam-Warnke Model

It has been demonstrated that the Willam-Warnke five-parameter failure criterion can provide a good representation of experimental results over a wide range of stress combinations. Ideally the five parameters, or material constants, should be obtained from experimental data that reasonably represent the actual state of stress and plasticity characteristics of the material in consideration.

For concrete columns confined by circular reinforcement the confining stresses  $\sigma_2$  and  $\sigma_3$  are symmetrical. With the observation that  $\sigma_3 = \sigma_2$  and utilizing Eqs. (3.4) and (3.9),  $\rho$  can be expressed as

$$\rho = \sqrt{\frac{2}{3}} \left( \frac{\sigma_2 - \sigma_1}{f'_{co}} \right) \quad (3.15)$$

In addition, Eq. (3.14) can be rewritten as

$$\rho_c = \sqrt{5} f'_{co} \left( b_0 + b_1 \overline{\sigma_a} + b_2 \overline{\sigma_a}^2 \right) \quad (3.16)$$

Since  $\rho = \rho_c$  for circular confined columns, equating Eq. (3.15) to Eq. (3.16) gives

$$\sqrt{\frac{2}{3}} \left( \frac{\sigma_2 - \sigma_1}{f'_{co}} \right) = \sqrt{5} f'_{co} \left( b_0 + b_1 \overline{\sigma_a} + b_2 \overline{\sigma_a}^2 \right) \quad (3.17)$$

By relabeling the ultimate axial stress  $\sigma_1$  as  $f'_{cc}$ , and the confining stress  $\sigma_2$  as  $f_l$ , Eq.

(3.17) can be rewritten as

$$\sqrt{\frac{2}{3}} \left( \frac{f_l - f'_{cc}}{f'_{co}} \right) = \sqrt{5} f'_{co} \left( b_0 + b_1 \left( \frac{f'_{cc} + 2f_l}{3f'_{co}} \right) + b_2 \left( \frac{f'_{cc} + 2f_l}{3f'_{co}} \right)^2 \right) \quad (3.18)$$

where the ultimate axial strength  $f'_{cc} = \sigma_1$  and  $f_l = \sigma_2 = \sigma_3$ . This can be conveniently rewritten in the following form (for the mean coordinate system) similar to that presented by Bing et al. (2001) (for the octahedral coordinate system):

$$f'_{cc} = f'_{co} \left( \left( \frac{3(b_1 \frac{\sqrt{15}}{3} + \sqrt{2})}{2b_2 \frac{\sqrt{15}}{3}} \right) + \sqrt{\left( \frac{3(b_1 \frac{\sqrt{15}}{3} + \sqrt{2})}{2b_2 \frac{\sqrt{15}}{3}} \right)^2 - \frac{9b_0}{b_2} - \frac{9\sqrt{2}}{b_2 \frac{\sqrt{15}}{3}} \frac{f_l}{f'_{co}} - 2 \frac{f_l}{f'_{co}}} \right) \quad (3.19)$$

Note that the material coefficients are multiplied by  $\frac{\sqrt{15}}{3}$  to convert from the octahedral coordinate system used by Bing et al. (2001) to the mean coordinate system used in the present study.

By using concrete triaxial tests performed by Schickert and Winkler (1977) and material properties suggested by Elwi and Murray (1979), Mander et al. (1988) proposed the ultimate axial strength of concrete columns confined by steel spirals or circular hoops could be predicted with the following equation:

$$f'_{cc} = \left( -1.254 + 2.254 \sqrt{1 + 7.940 \frac{f_l}{f'_{co}} - 2 \frac{f_l}{f'_{co}}} \right) f'_{co} \quad (3.20)$$

For columns utilizing high-strength concrete, it has been found that the effectiveness of confinement decreases for concrete with a higher compressive strength. Accordingly, Bing et al. (2001) proposed the following equation to be used for predicting the ultimate axial strength of columns utilizing high-strength concrete confined with transverse steel reinforcement:

$$f'_{cc} = \left( -0.413 + 1.413 \sqrt{1 + 11.4 \frac{f_l}{f'_{co}} - 2 \frac{f_l}{f'_{co}}} \right) f'_{co} \quad (3.21)$$

For columns with hardening behavior (which was the type of behavior exhibited in the columns of the present study), Yan and Pantelides (2006) proposed the ultimate axial strength of concrete columns confined externally with FRP-wrap could be predicted with the following equation:

$$f'_{cc} = \left( -4.322 + 4.721 \sqrt{1 + 4.193 \frac{f_l}{f'_{co}} - 2 \frac{f_l}{f'_{co}}} \right) f'_{co} \geq f'_{co} \quad (3.22)$$

### 3.3.1 Axial Strength of FRP-Confined Normal- and High-Strength Concrete

The goal was to develop the model using experimental data from as many specimens as possible that represent the actual state of stress and plasticity characteristics of the material under consideration. For the present study, the material constants  $b_0$ ,  $b_1$ , and  $b_2$  from Eq. (3.14) were determined from a regression analysis utilizing 64 triaxial compression test failure data points obtained from the present study, Mohamed et al.

(2014), Afifi et al. (2013a, 2013b), Pantelides et al. (2013a), Yan and Pantelides (2006), Ansari and Li (1998), and Imran and Pantazopoulou (1996). All tests had been performed on circular specimens and included concrete strengths ranging from  $f'_c = 2,200$  psi to  $f'_c = 15,600$  psi, but due to the limited number of tests and confinement range available for specimens confined with internal FRP spirals, specimens confined with lower levels of external FRP wrap/strips and hydraulically applied confining fluid were also included. Thirty-one of these tests utilized internal FRP (GFRP and CFRP) spiral confining reinforcement (the present study, Mohamed et al. 2014, Afifi et al. 2013a, 2013b and Pantelides et al. 2013a), five tests utilized external FRP confining wrap (Yan and Pantelides 2006), and 28 tests utilized a hydraulically-applied, pressurized confining fluid (Ansari and Li 1998; Imran and Pantazopoulou 1996).

Due to the observation that FRP-spiral confining bars exhibited less effective confining capabilities due to their lower stiffness as opposed to other confining methods like steel, tests used for the regression analysis were limited to those such that  $\overline{\sigma}_a$  of Eq. (3.9) did not exceed  $|-1.4|$ . This determination is discussed in greater detail in Section 3.3.4. The limiting confining pressure for this restriction can be derived from the following expression:

$$\overline{\sigma}_a = \frac{\sigma_1 + \sigma_2 + \sigma_3}{3f'_{co}} < |-1.4| \quad (3.23)$$

Knowing that  $\sigma_1 = f'_{co}$  and  $\sigma_2 = \sigma_3 = f_l$ , Eq. (3.23) can be rewritten as

$$\frac{f'_{co} + 2f_l}{3f'_{co}} < 1.4 \quad (3.24)$$

By reordering terms, the limiting confining pressure used in the present study can be

expressed in terms of the normalized ultimate confining pressure,  $\frac{f_l}{f'_{co}}$ , such that

$$\frac{f_l}{f'_{co}} < 2.1 - \frac{1}{2} \frac{f'_{co}}{f'_{co}} \quad (3.25)$$

The failure data points, consisting of the normalized mean normal stress  $\bar{\sigma}_a$  and the normalized mean shear stress  $\bar{\tau}_a$ , for the case satisfying Eq. (3.23), are shown in Figure 3.4. According to the stipulation of Eq. (3.23), this resulted in using only data points where  $\bar{\sigma}_a < 1.4$  as shown in the figure. The regression curve from Mander et al. (1988) is also shown for comparison. A regression analysis of the present research data points shows that a best-fit curve through these points can be described by the general equation,  $y = 0.1199 - 0.8032x - 0.2155x^2$ . From Eq. (3.14) for the compression meridian, the material constant parameters can be extracted as  $b_0 = 0.1199$ ,  $b_1 = -0.8032$ , and  $b_2 = -0.2155$ . Using these parameters Eq. (3.19) can be rewritten as

$$f'_{cc} = \left( -2.03 + 3.03 \sqrt{1 + 5.00 \frac{f_l}{f'_{co}}} - 2 \frac{f_l}{f'_{co}} \right) f'_{co} \quad (3.26)$$

Eq. (3.26) represents the proposed general equation to predict the ultimate axial strength of concrete columns confined with internal FRP-spiral confining bars for a full range of concrete strengths.

### 3.3.2 Axial Strength of FRP-Confined High-Strength Concrete

A regression analysis was also performed utilizing only high-strength concrete specimens having an  $f'_c > 8,000$  psi from the 64 triaxial compression tests used in

developing Eq. (3.26). Of the 64 tests, 17 had an  $f'_c > 8,000$  psi. Three utilized internal GFRP-spiral confining reinforcement from the present study, and the remaining 14 utilized a hydraulically applied, pressurized confining fluid performed by Ansari and Li (1998) and Imran and Pantazopoulou (1996). Due to the fewer points available, this contains a less-desirable representation of data points and a lower  $R^2$  value, as shown in Figure 3.5, but is presented here for comparison. The material constant parameters were found to be  $b_0 = 0.1361$ ,  $b_1 = -0.7589$ , and  $b_2 = -0.2039$ . Using these parameters, Eq. (3.19) was rewritten as

$$f'_{cc} = \left( -2.48 + 3.48 \sqrt{1 + 3.98 \frac{f_l}{f'_{co}}} - 2 \frac{f_l}{f'_{co}} \right) f'_{co} \quad (3.27)$$

Eq. (3.27) represents the proposed equation to predict the ultimate axial strength of concrete columns confined with internal GFRP-spiral confining bars for high-strength concrete only.

### 3.3.3 Modified Axial Strength of FRP-Confined Normal- and High-Strength Concrete

It was also of further interest to perform a regression analysis on a full range of concrete strengths but with even a more restrictive confining pressure such that

$$\frac{\sigma_a}{f'_{co}} = \frac{\sigma_1 + \sigma_2 + \sigma_3}{3f'_{co}} < |-0.8| \quad (3.28)$$

which, when expressed in terms of the normalized ultimate confining pressure,  $\frac{f_l}{f'_{co}}$ , is

found to be

$$\frac{f_l}{f'_{co}} < 1.2 - \frac{1}{2} \frac{f'_{co}}{f'_{co}} \quad (3.29)$$

Based on the observations of lower confinement effectiveness of the limited number of experimental tests performed on FRP spiral-confined columns and based on estimated calculations of FRP-spiral confinement capacities, it appears that under most conditions the confining pressure of current available FRP-spiral reinforcement would furthermore likely fall under this limit. This is discussed in greater detail in Section 3.3.4. Fifty-one of the original 64 test failure data points fell in this category. Thirty-one tests utilized internal FRP (GFRP and CFRP) spiral confining reinforcement (Afifi et al. 2013a, 2013b; Pantelides et al. 2013a; Mohamed et al. 2014; the present study), two tests utilized external FRP confining wrap (Yan and Pantelides 2006), and 18 tests utilized a hydraulically applied, pressurized confining fluid (Ansari and Li 1998; Imran and Pantazopoulou 1996). Figure 3.6 shows the data points where  $\overline{\sigma}_a < |-0.8|$ . Based on a regression analysis of these data points, the material constant parameters were found to be  $b_0 = 0.0833$ ,  $b_1 = -0.9701$ , and  $b_2 = -0.3909$ , and Eq. (3.19) was rewritten as

$$f'_{co} = \left( -0.47 + 1.47 \sqrt{1 + 11.74 \frac{f_l}{f'_{co}}} - 2 \frac{f_l}{f'_{co}} \right) f'_{co} \quad (3.30)$$

Eq. (3.30) represents the present study's modified proposed equation to predict the ultimate axial strength of concrete columns confined with internal FRP-spiral confining bars for a full range of concrete strengths.

### 3.3.4 Comparison of Axial Strength Equations

Figure 3.7 shows a comparison of all failure data point trendlines with the actual failure data points plotted categorized by the type of confinement provided. It is interesting to note the close grouping of FRP-spiral confined columns, which included both GFRP and CFRP-spirals at the lower end of the data field. Figure 3.8 shows the comparison with only the trendlines of the present study.

As seen in Figures 3.7 and 3.8, all specimens with FRP-spiral confinement had a value of  $\overline{\sigma}_a$  less than 0.4, which was considerably less than the maximum assumed limits of 1.4 and 0.8 imposed in Sections 3.3.1 and 3.3.2. Calculations, however, were performed using Eqs. (3.26) and (3.30) to also estimate potential upper limit values of  $\overline{\sigma}_a$  that could be achieved with FRP-spirals based on the information currently available regarding the behavior of FRP-spirals. The procedure of determining the values of 1.4 and 0.8 was somewhat of an iterative method because the equations used were based on an initially assumed maximum value for  $\overline{\sigma}_a$ . It was also somewhat subjective due to the uncertainty of the variables that  $\overline{\sigma}_a$  depends upon (i.e., initial unconfined concrete strength, maximum achievable spiral strain, etc.).

Keeping this in perspective, an example of a potential upper limit value of  $\overline{\sigma}_a$ , not exceeding 1.4, is the hypothetical situation of a #4 CFRP spiral with a modulus of elasticity of 22,000 ksi at 1.5 in. pitch and 12 in. diameter and maximum spiral strain of 0.003 (0.001 or less was typically observed in the present study) with  $f'_c = 2,500$  psi, which produces a  $\overline{\sigma}_a$  value of approximately 1.3 using Eq. (3.26). An example of a

potential upper limit value of  $\overline{\sigma}_a$ , not exceeding 0.8, is the hypothetical situation of a #4 CFRP spiral with a modulus of elasticity of 22,000 ksi at 2 in. pitch and 12 in. diameter and maximum spiral strain of 0.0025 with  $f'_c = 4,500$  psi, which produces a  $\overline{\sigma}_a$  value of approximately 0.7 using Eq. (3.30). It was also observed that two specimens used from Yan and Pantelides (2006) that had external wrap placed in strips as opposed to continuously had  $\overline{\sigma}_a$  values of approximately 0.8 or less, which would behave similarly to an FRP-spiral. Based on these observations, the values of 1.4 and 0.8 were assumed reasonable for use in the present research. Further research is needed to better quantify the validity of these assumptions.

Figure 3.9 shows a comparison between the ultimate axial strength models of the present study (Eq. (3.26), Eq. (3.27) and Eq. (3.30)) to that of Mander et al. (1988). The failure data points are also plotted to provide perspective as to their location along these curves. Figure 3.10 shows only the ultimate axial strength models of the present study with the failure data points. The low effectiveness of confinement can be seen in these figures by the close grouping of the FRP-spiral-confined columns near the bottom of the curves. The average normalized confining pressure,  $\frac{f_l}{f'_c}$ , of the data points of these specimens was 0.006 with a maximum of 0.02 and a minimum of 0.0007.

As seen in Figure 3.9, the curve from Eq. (3.26) follows a closer but flatter version of the Mander et al. (1988) curve, which is derived only for internal steel reinforcement confinement. This can be attributed to the lower effectiveness of confinement that the internal FRP-spiral provides due to its lower modulus of elasticity in comparison to that expected in similarly confined columns utilizing steel spirals. Also,

the curve from Eq. (3.26) is much shallower than the steeper Yan and Pantelides (2006) curve for external FRP-wrap confinement. This likewise can be attributed to the lower ratios of confinement of internal FRP-spirals in contrast to the potentially high ratios of confinement that can be provided in an FRP wrap. Also, the use of a lower strength concrete ( $f'_c = 2,200$  psi) likely had an influence on the resulting steepness of the curve produced by Yan and Pantelides (2006).

In contrast, the curve from Eq. (3.26) is steeper than that proposed by Bing et al. (2001) for high-strength concrete for steel-confined columns where they also found the effectiveness of confining reinforcing to be reduced with respect to that proposed by Mander et al. (1988) for normal-strength concrete. Eq. (3.30) of the present study actually reflects a more pronounced reduction of influence of confinement in a manner more similar to that of Bing et al. (2001). The lack of available test data of FRP spiral-confined specimens at higher levels of confinement make it difficult to determine whether Eq. (3.26) or Eq. (3.30) more accurately represents the confinement behavior, especially above the point  $\frac{f_l}{f'_{co}} \approx 0.13$  where the two curves begin to deviate from each other. Eq. (3.30) is more conservative and, based on the lower confinement influence observed in currently available FRP-spiral confining reinforcement, would likely be more representative of FRP spiral-confined columns.

#### 3.4 Theoretical Stress-Strain Relationship of FRP-Confined Concrete

In plasticity theory, the size and shape of ultimate surfaces vary continuously from initial yielding to ultimate failure for plasticity models with which the failure

criterion is applied as depicted in Figure 3.11. This works well with the assumption that concrete is an isotropic material and that the ultimate surfaces can be generated using the isotropic rule under the progressive stages of an axial load. Yan and Pantelides (2006), Imran (1994), Mizuno and Hatanaka (1992), and Smith (1987) found that this assumption has shown good results when used to model the compressive behavior of concrete subjected to monotonic loading and therefore has also been used in this study. As shown in Figure 3.11, loading surfaces are defined as the intermediate surfaces where the ultimate surface evolves along a given compressive loading path. Since isotropic rules apply, the loading surfaces are assumed to have the same functional form as the ultimate surface and allows for the use of the same constant values for defining the evolving ultimate surfaces. As a result, the model of Eq. (3.26), Eq. (3.27), or Eq. (3.30) could be used to calculate the axial strength corresponding to any state of FRP confining stress. For example, this could apply for a different spiral pitch or for CFRP-spirals, which have a much higher modulus of elasticity ( $\approx 20,000,000$  psi) than the GFRP-spirals used in the present study ( $\approx 3.2$  times greater). Figure 3.12 shows a generic schematic of how the stress-strain relation for unconfined concrete can be improved by the implementation of lateral confinement.  $f'_{\infty}$  and  $f'_{\infty}$  represents the maximum stress for unconfined and confined concrete, respectively, and  $\varepsilon'_{\infty}$  and  $\varepsilon'_{\infty}$  represent the correlating strains at the maximum states of stress for unconfined and confined concrete, respectively.

The formation and expansion of microcracks largely determines the response of concrete subjected to triaxial states of stress. Imran (1994) showed that the evolution of microcracks governs concrete brittleness, ductility, dilatancy, and failure modes. All of these conditions in general depend on the triaxial state of stress in the concrete. Due to

the elastic behavior of the internal GFRP-spirals and the use of high-strength concrete, the stress-strain curves for the specimens in this study (Chapter 2) exhibited a continuous hardening behavior with little or no postpeak degradation after obtaining maximum axial stress. This type of behavior can be reasonably represented by the uniaxial stress-strain relationships for concrete as proposed by Popovics (1973), which is adopted in this study. As rearranged by Yan and Pantelides (2006), the Popovics model defines the relation between the axial stress,  $f_c$ , and strain,  $\varepsilon_c$ , of confined concrete with this type of hardening behavior as

$$f_c = \frac{E_0 \varepsilon_c}{1 + (K - 1) \left( \frac{\varepsilon_c}{\varepsilon'_{cc}} \right)^r} \quad (3.31)$$

where  $E_0$  = initial modulus of elasticity, and the parameters  $r$  and  $K$  are defined as

$$r = \frac{K}{K - 1} \quad (3.32)$$

$$K = \frac{E_0}{E_s} \quad (3.33)$$

where

$$E_s = \frac{f'_{cc}}{\varepsilon'_{cc}} \quad (3.34)$$

and  $f'_{cc}$  is the ultimate axial stress as defined in Section 3.3. The ultimate axial strain,  $\varepsilon'_{cc}$ , can be determined by the following equation as proposed by Imran and Pantazopoulou (1996):

$$\varepsilon'_{cc} = \varepsilon'_{co} \left( 6 \left( \frac{f'_{cc}}{f'_{co}} - 0.83 \right) \right) \quad (3.35)$$

where  $\varepsilon'_{co}$  is the axial strain corresponding to the axial strength of the unconfined concrete  $f'_{co}$ , which can be estimated by the following equation proposed by Popovics (1973):

$$\varepsilon'_{co} = 2.7 \times 10^{-4} \times \sqrt[4]{f'_{co}} \quad (3.36)$$

where  $f'_{co}$  is expressed in pounds per square inch (psi). A general depiction of the stress-strain curve for unconfined concrete is shown in Figure 3.12 and for confined concrete in Figures 3.12 and 3.13.

As shown in Figure 3.13 and Eqs. (3.31) through (3.34), the Popovics curve can be defined by the initial modulus of elasticity,  $E_0$ , and the peak stress and strain,  $f'_{cc}$  and  $\varepsilon'_{cc}$ . It represents a stress-strain curve that exhibits a hardening relationship where failure occurs at the peak stress and strain. This hardening relationship is also referred to as the hardening rule in plasticity theory, which defines the uniaxial compressive loading path as shown in Figure 3.11 (a). It also defines the change of the hardening properties of concrete during the course of plastic flow as well as the change in the loading surface.

### 3.5 Internal FRP-Spiral Confining Pressure

The method to determine the ultimate confining pressure  $f_l$  for a column confined with internal spirals can be accomplished following a method prescribed by Mander et al. (1988), which followed an approach similar to Sheikh and Uzumeri (1980). Let  $f'_l$  be the spiral produced confining pressure, which can be derived from the free-

body diagram of a half-section of the column as shown in Figure 3.14. As shown, the spiral provides hoop tension, which exerts a uniform lateral pressure  $f'_l$  on the concrete core. The equilibrium of forces requires

$$2A_{sp}f_{sp} = f'_l s d_s \quad (3.37)$$

which can be rewritten as

$$f'_l = \frac{2A_{sp}f_{sp}}{s d_s} \quad (3.38)$$

where  $A_{sp}$  is the cross-sectional area of the spiral,  $s$  is the center-to-center spacing of the spiral, and  $d_s$  is the diameter of confinement provided by the spiral as shown in Figure

3.15.  $f_{sp}$  is the ultimate strength of the spiral, which for FRP reinforcement can be calculated by

$$f_{sp} = E_{sp} \varepsilon_u \quad (3.39)$$

where  $E_{sp}$  is the modulus of elasticity of the spiral and  $\varepsilon_u$  is the ultimate strain of the spiral at failure.

The maximum pressure from the confining spiral can only be exerted effectively on that part of the concrete core where the confining stress has fully developed due to arching action as shown in Figure 3.15 (a). As shown, the arching action is assumed to occur between the levels of the spiral, such that halfway between the spirals, the area of ineffectively confined concrete will be largest, and the area of effectively confined concrete,  $A_e$ , will be the smallest. Due to the fact that not all of the concrete of a column with internal spirals is effectively confined, a confinement effectiveness coefficient,  $k_e$ , is suggested by Mander et al. (1988) to help account for this as follows

$$k_e = \frac{A_e}{A_{cc}} \quad (3.40)$$

where

$$A_e = \frac{\pi}{4} \left( d_s - \frac{s'}{4} \right)^2 = \frac{\pi}{4} d_s^2 \left( 1 - \frac{s'}{4d_s} \right)^2 = \frac{\pi}{4} d_s^2 \left[ 1 - \frac{s'}{2d_s} + \left( \frac{s'}{4d_s} \right)^2 \right] \quad (3.41)$$

which by neglecting the higher order term, which is much less than one, allows Eq. (3.41)

to be rewritten as

$$A_e = \frac{\pi}{4} d_s^2 \left( 1 - \frac{s'}{2d_s} \right) \quad (\text{spiral}) \quad (3.42)$$

and

$$A_{cc} = A_c - A_{lr} \quad (3.43)$$

where

$$A_c = \frac{\pi}{4} d_s^2 \quad (3.44)$$

and  $A_{lr}$  equals the total area of the longitudinal reinforcement,  $d_s$  is the diameter of confinement provided by the spiral (center-to-center of the spiral), and  $s'$  is the clear space between levels of the spirals as shown in Figure 3.15. In a similar manner, for reference only,  $A_e$  for circular hoops can be found to be

$$A_e = \frac{\pi}{4} d_s^2 \left( 1 - \frac{s'}{2d_s} \right)^2 \quad (\text{circular hoop}) \quad (3.45)$$

To account for the difference between the actual concrete core and the effectively confined concrete core, Mander et al. (1988) suggests that the ultimate confining pressure  $f_l$  be multiplied by the confinement effectiveness coefficient  $k_e$  such that the effective

ultimate confining pressure  $f_l$  is

$$f_l = k_e f'_l \quad (3.46)$$

where  $k_e$  is derived from Eq.(3.40) and  $f'_l$  is derived from Eq. (3.38).

### 3.6 Implementation of Internal FRP-Confined Concrete Model

Conventional concrete confinement models, like the Mander et al. (1988) model, assume that the confining pressure is constant after yielding. This is based on the assumption that the confining element, namely steel reinforcement, yields and behaves in a perfectly plastic manner, which provides a constant confining pressure. For FRP confinement, however, this assumption is not applicable because FRP reinforcement exhibits linear elastic behavior up to failure. As a result, the confining pressure from an FRP confining element,  $f_l$ , also varies linearly until failure. Therefore, the ideal implementation of an FRP-confined concrete model must take that into consideration and account for a different level of confining pressure depending on what level of strain the FRP confining element is subjected to at a given level of stress. Figure 3.16 shows a comparison between a simplified, elastic-plastic stress-strain curve for steel as opposed to an elastic stress-strain curve for CFRP or GFRP reinforcement.

A stress-strain curve model for FRP-confined concrete can be developed based on Eq. (3.31) for a concrete column with a given amount of confinement pressure,  $f_l$ . The general shape of the curve follows the Popovics model (Figure 3.13), which is defined by the initial modulus of elasticity,  $E_0$ , and the peak stress and strain,  $f'_{cc}$  and  $\varepsilon'_{cc}$ . The initial modulus of elasticity,  $E_0$ , can be taken as equal to the modulus of elasticity of the

concrete in compression,  $E_c$  ( $E_0 = E_c$ ). The value of  $f'_{cc}$  can be derived from Eq. (3.26), Eq. (3.27), or Eq. (3.30), where  $f_l$  is the effective ultimate confining pressure from Eq. (3.46), and  $\varepsilon'_{cc}$  can be obtained from Eq. (3.35).

### 3.7 Axial Load Capacity of Internal FRP-Confined Concrete Columns

The proposed confinement model can be used to estimate the maximum load capacity for concrete columns reinforced with internal FRP confinement spirals and steel and/or FRP longitudinal bars. The estimated maximum load capacity  $P_c$  can be found with the following equation:

$$P_c = f'_{cc} A_{cc} + f_y A_{st} + \varepsilon_{FRP} E_{FRP} A_{FRP} \quad (3.47)$$

where  $f'_{cc}$  is derived from Eq. (3.26), Eq. (3.27), or Eq. (3.30),  $A_{cc}$  is the area of the concrete core as calculated by Eq. (3.43),  $f_y$  and  $A_{st}$  are the yield strength and area of longitudinal steel bars, respectively,  $\varepsilon_{FRP}$  is the axial strain in the longitudinal FRP bars at maximum load,  $E_{FRP}$  is the modulus of elasticity of the longitudinal FRP bars, and  $A_{FRP}$  is the area of longitudinal FRP bars. If  $\varepsilon_{FRP}$  is not known, it can be estimated as 0.003 in./in. as observed in the present study and Pantelides et al. (2013a). This equation uses the assumption that the concrete cover outside the concrete core spalls away in the failure region and carries no load when the maximum axial load is reached. Therefore, this assumption applies when the concrete core is sufficiently confined such that

$$\frac{f'_{cc}}{f'_{co}} > \frac{A_{lc}}{A_{cc}} \quad (3.48)$$

where  $f'_{co}$  is the unconfined concrete strength and  $A_{lc}$  is the total net concrete area of

the column cross-section ( $A_{cc}$  plus the area of concrete cover). Otherwise, if this condition is not satisfied, then the contributing axial strength from the concrete will be governed by the unconfined concrete strength  $f'_{co}$  over the total net concrete area  $A_{tc}$ , and the following equation will apply:

$$P_c = f'_{co} A_{tc} + f_y A_{st} + \epsilon_{FRP} E_{FRP} A_{FRP} \quad (3.49)$$

Table 3.1 shows the analytical axial load capacity for the short columns of the present study (#1S-DB0, #2S-SS0, and #3S-SG0) in comparison to the experimental test axial load capacities and similarly for four columns of Pantelides et al. (2013a) experimental tests (#9HYBCTL, #10HYBCTL, #13GLCTL and #14GLCTL). As shown in the table, two of the three columns of the present study had analytically predicted axial loads between 92% to 102% of the experimental test axial loads. The analytical load of specimen #1S-DB0 was 12% greater than that of the experimental load, but this was due to the premature failure of this column as observed and noted in Section 2.5. The analytically predicted axial loads for the four columns of Pantelides et al. (2013a) were all between 96% to 107% of the experimental test axial loads.

Table 3.1: Summary of analytical and experimental test load capacities of the short columns of the present study and four columns of Pantelides et al. (2013a)

Specimen	$f'_{co}$ (psi)	** $f'_{cc}$ (psi)	$A_{st}$ (in. <sup>2</sup> )	$A_{FRP}$ (in. <sup>2</sup> )	$A_{cc}$ (in. <sup>2</sup> )	$A_{tc}$ (in. <sup>2</sup> )	Eq. (3.47), $P_c$ (kips)	***Eq. (3.49), $P_c$ (kips)	Test Max. Load (kips)
#1S-DB0	13,000	13,125	1.2	1.86	53.7	110.0	816	1,542	1,376
#2S-SS0	13,000	13,000	1.2	0	55.5	111.9	799	1,531	1,498
#3S-SG0	13,000	13,000	0	1.86	54.9	111.2	749	1,481	1,602
*#9HYBCTL	5200	5960	0.8	0	55.9	77.7	385	455	426
*#10HYBCTL	5200	5960	0.8	0	55.9	77.7	385	455	445
*#13GLCTL	5200	5960	0	1.24	55.5	77.3	354	425	444
*#14GLCTL	5200	5960	0	1.24	55.5	77.3	354	425	402

\* Column from Pantelides et al. (2013a)

\*\* Eq. (3.30) was used to calculate  $f'_{cc}$

\*\*\* Controls because Eq. (3.48) is not satisfied

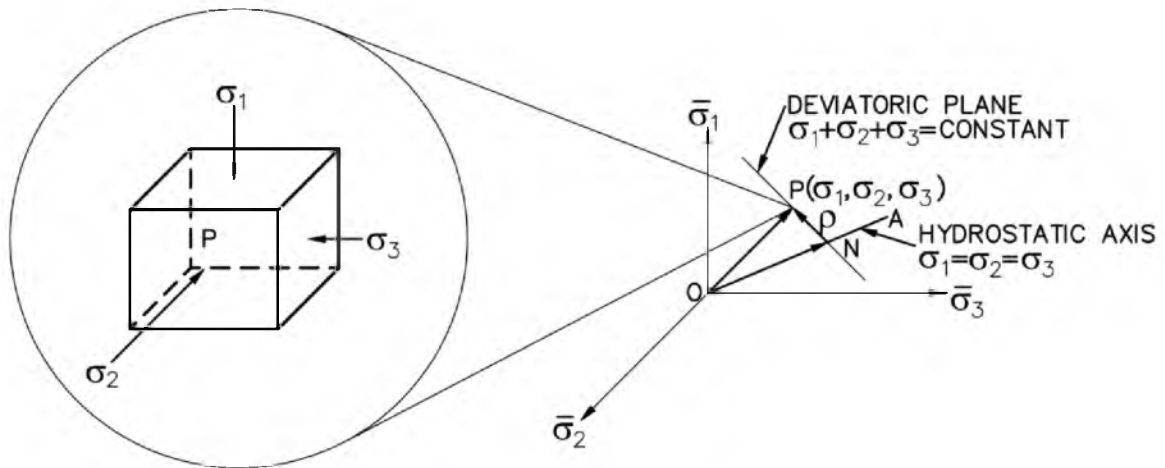


Figure 3.1: Three-dimensional stress space

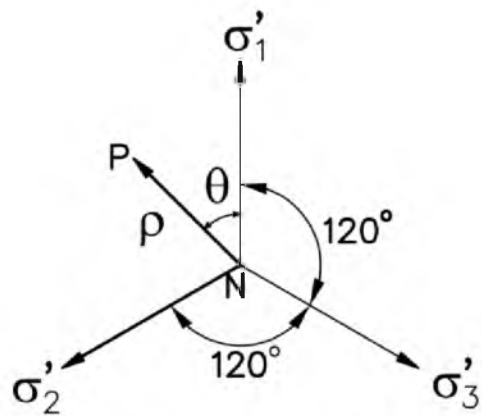
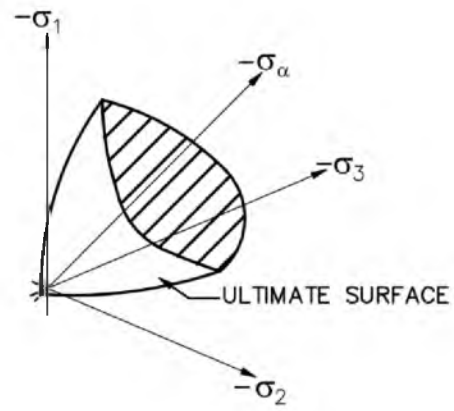
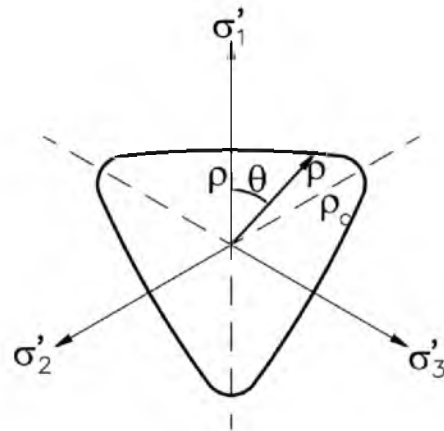


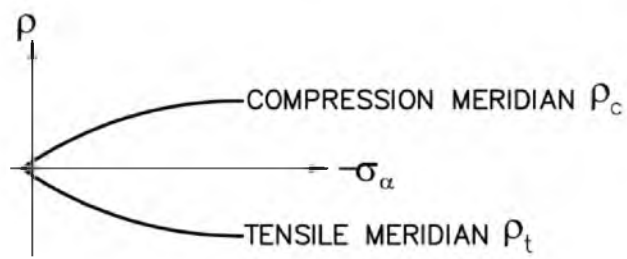
Figure 3.2: State of stress at a point projected on a deviatoric plane



(a)



(b)



(c)

Figure 3.3: Willam-Warnke ultimate surface:  
 (a) three-dimensional view; (b) deviatoric section;  
 (c) meridian section on  $\rho$ - $\sigma_\alpha$  plane

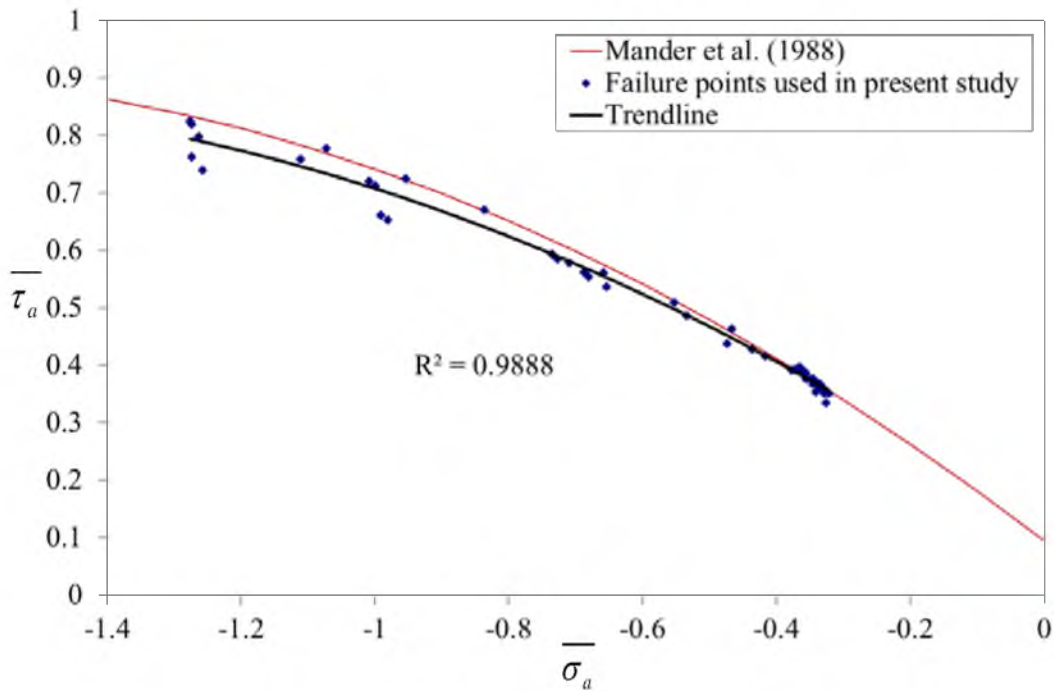


Figure 3.4: Failure data points for triaxial compression concrete tests  
 – normal- and high-strength concrete ( $\bar{\sigma}_a < |-1.4|$ )

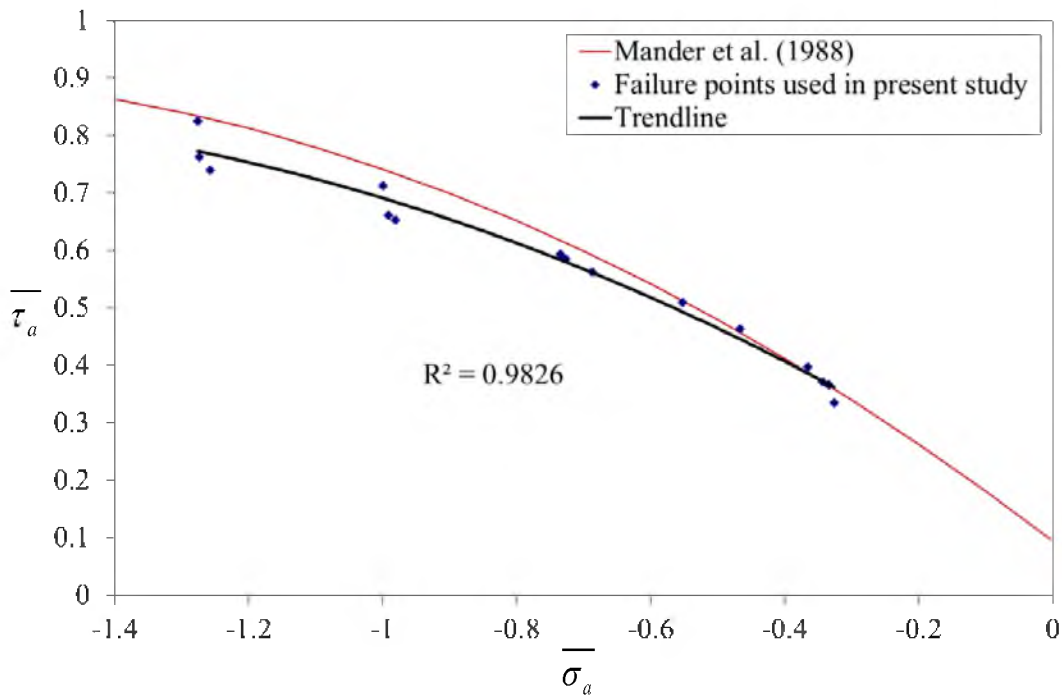


Figure 3.5: Failure data points for triaxial compression concrete tests  
 – high-strength concrete  $> 8,000$  psi ( $\bar{\sigma}_a < |-1.4|$ )

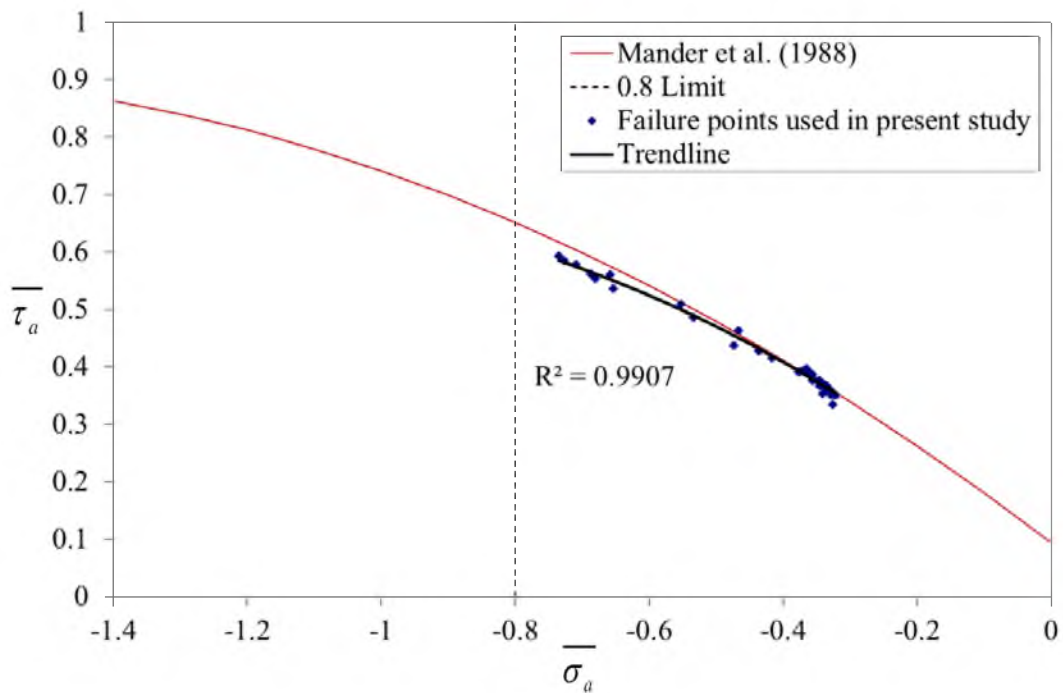


Figure 3.6: Failure data points for triaxial compression concrete tests  
– normal- and high-strength concrete ( $\bar{\sigma}_a < |-0.8|$ )

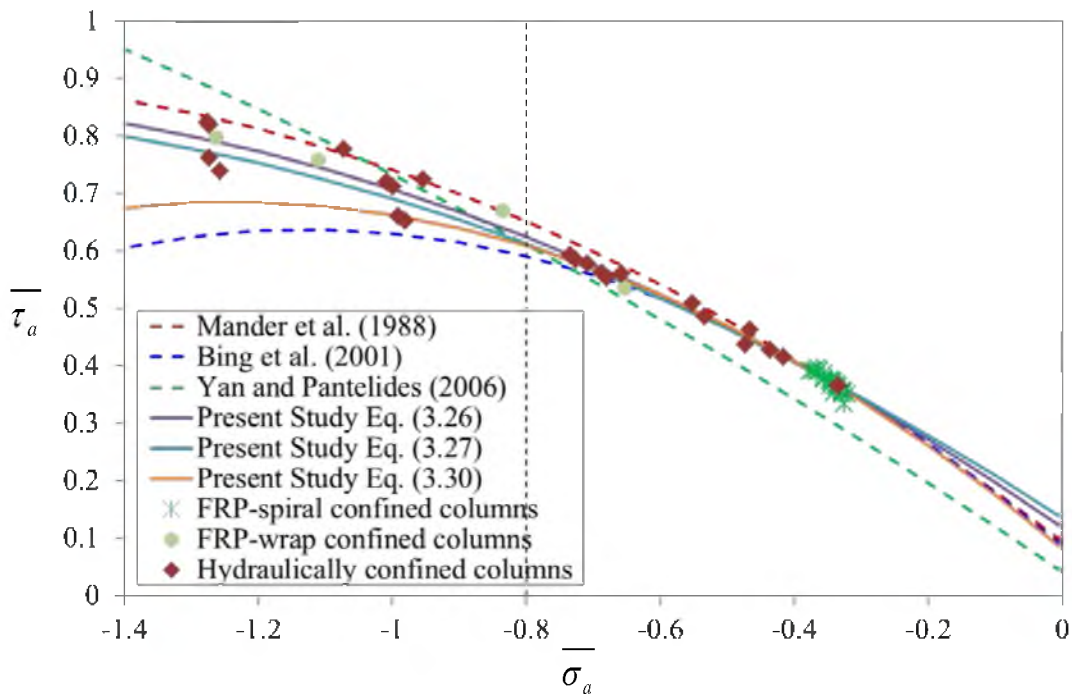


Figure 3.7: Failure data points for triaxial compression concrete tests – comparison of all curves

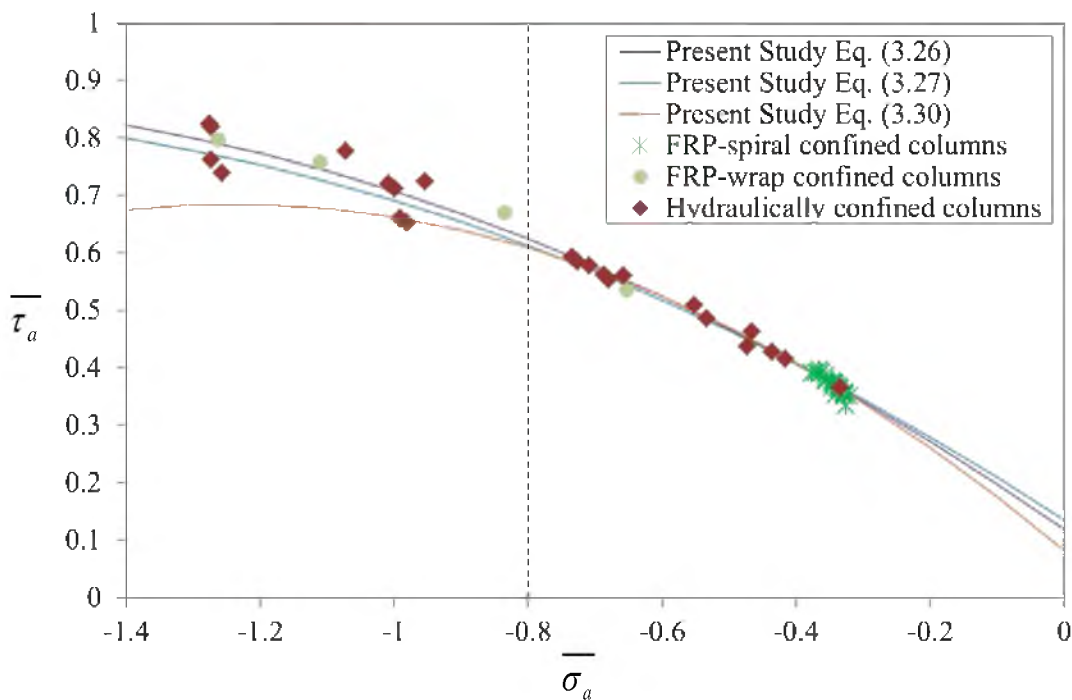


Figure 3.8: Failure data points for triaxial compression concrete tests – comparison of present study curves

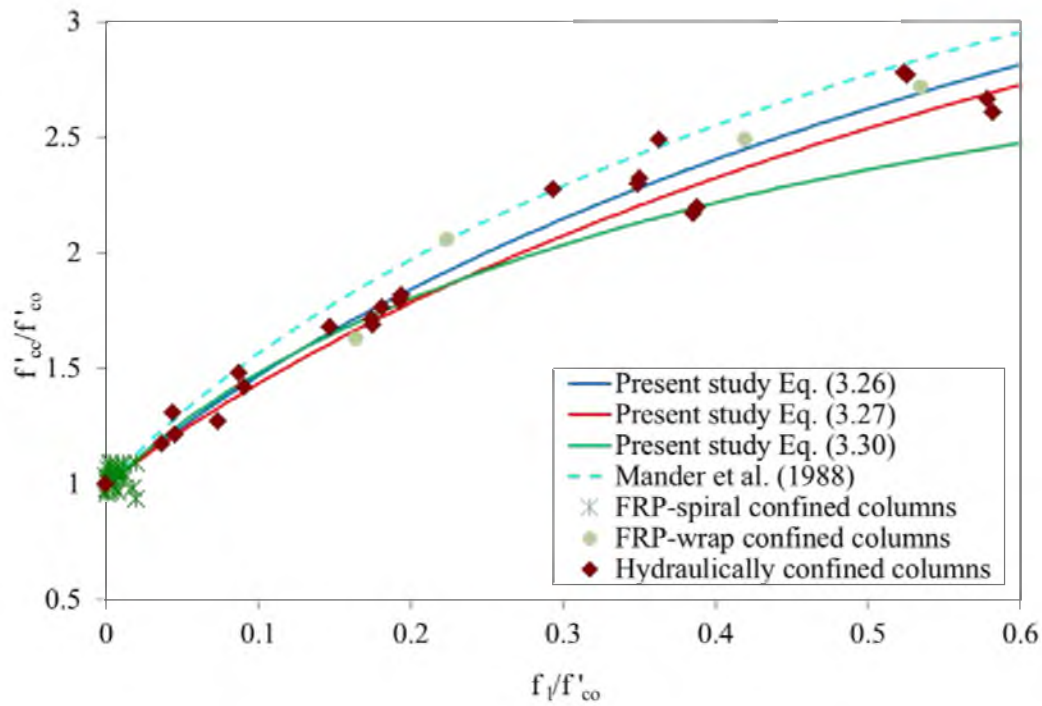


Figure 3.9: Comparison of different axial strength models for confined concrete

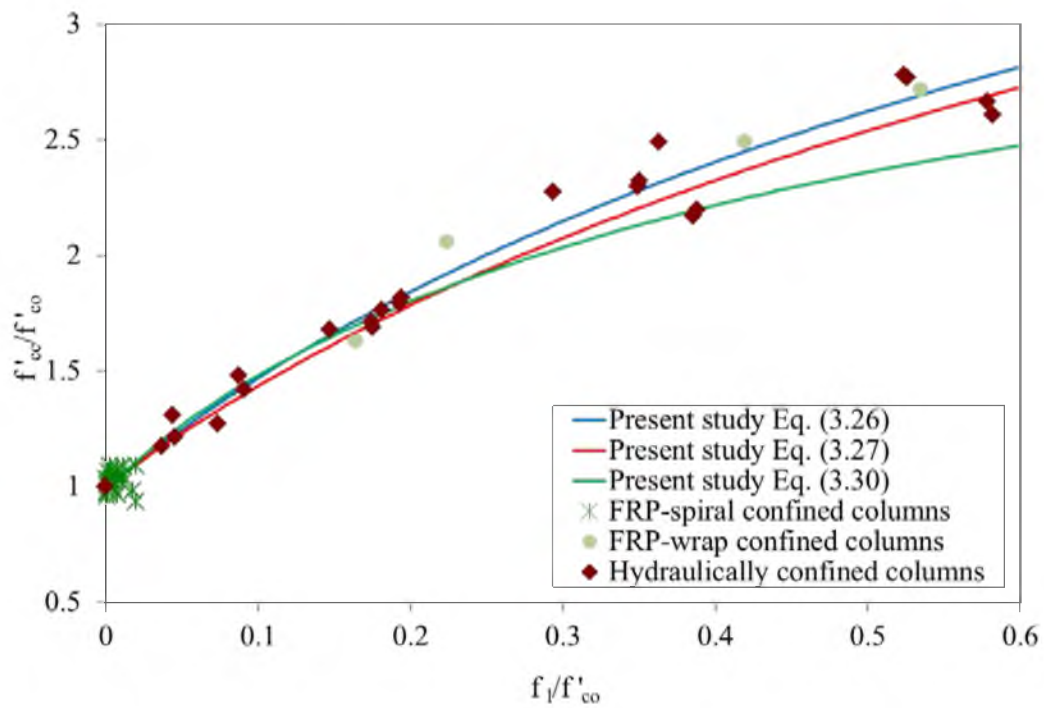


Figure 3.10: Comparison of different axial strength models for confined concrete

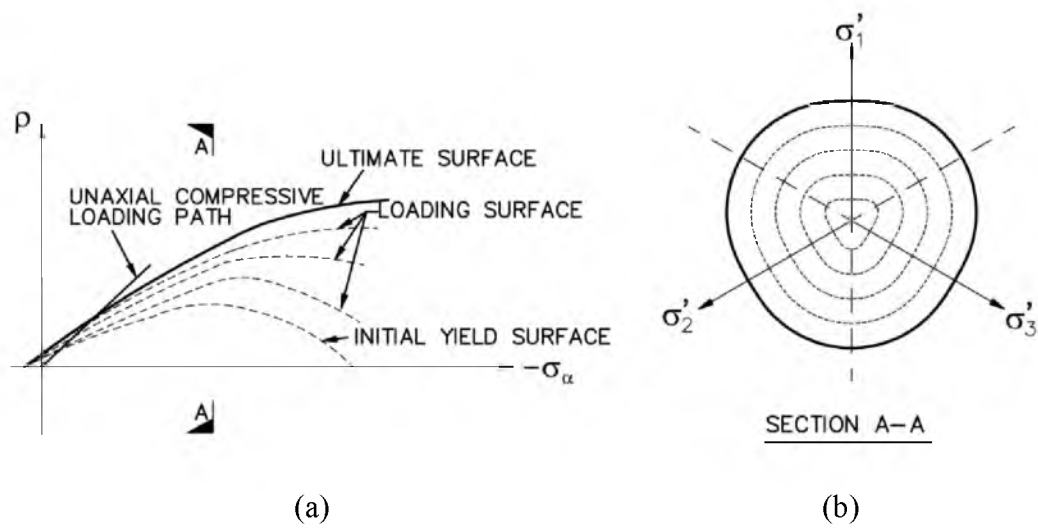


Figure 3.11: Evolution of loading surfaces:  
 (a) loading surfaces in the meridian plane;  
 (b) loading surfaces in the deviatoric plane (section A-A)

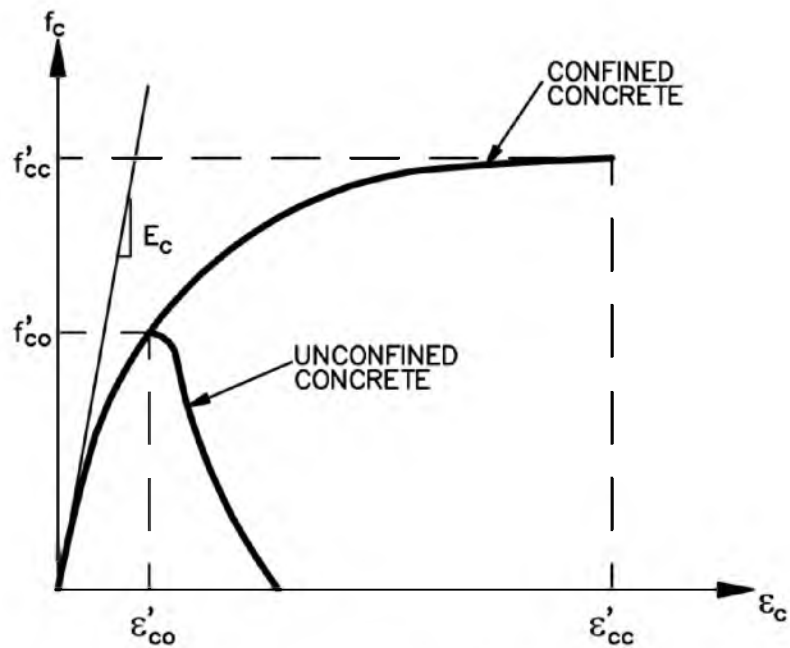


Figure 3.12: Generic stress-strain relation for unconfined and confined concrete

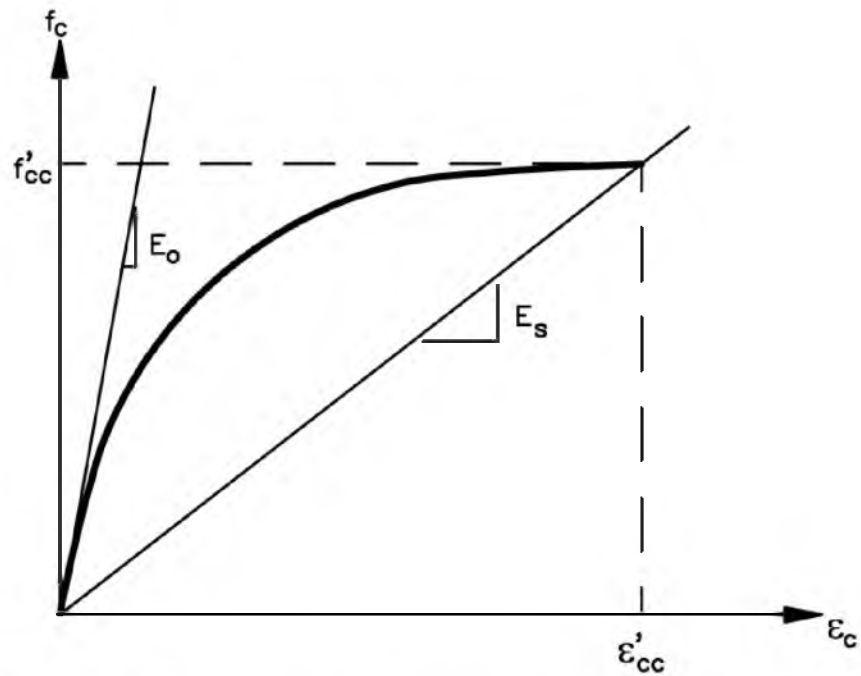


Figure 3.13: Stress-strain curve for concrete with hardening behavior

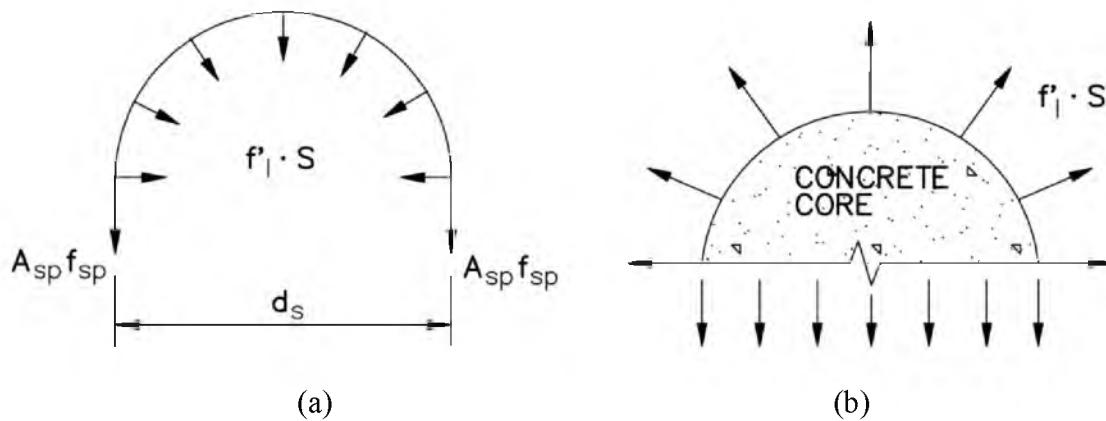
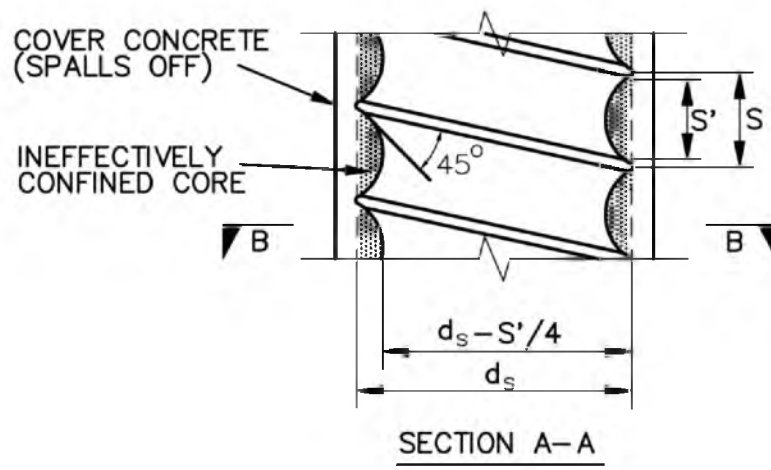
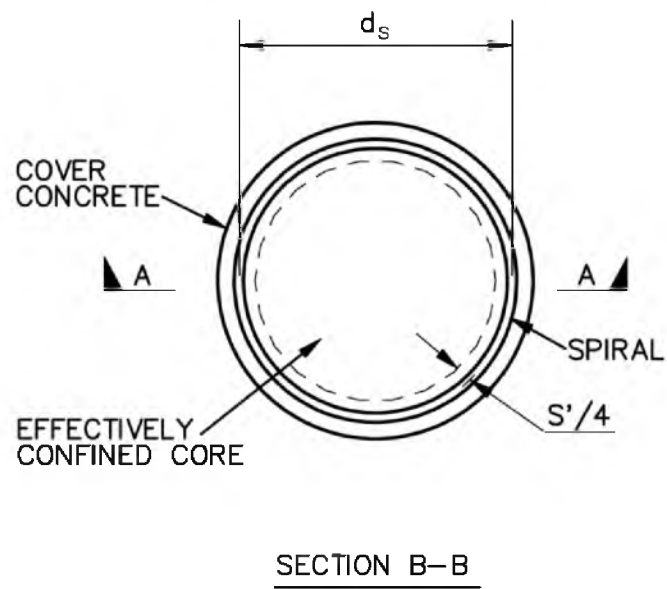


Figure 3.14: Half-body diagram at interface between spiral and concrete core:  
 (a) forces in spiral and spiral forces acting on concrete core;  
 (b) forces of concrete core acting on spiral



(a)



(b)

Figure 3.15: Effectively confined core for spiral reinforcement:  
 (a) elevation view; (b) cross-section view

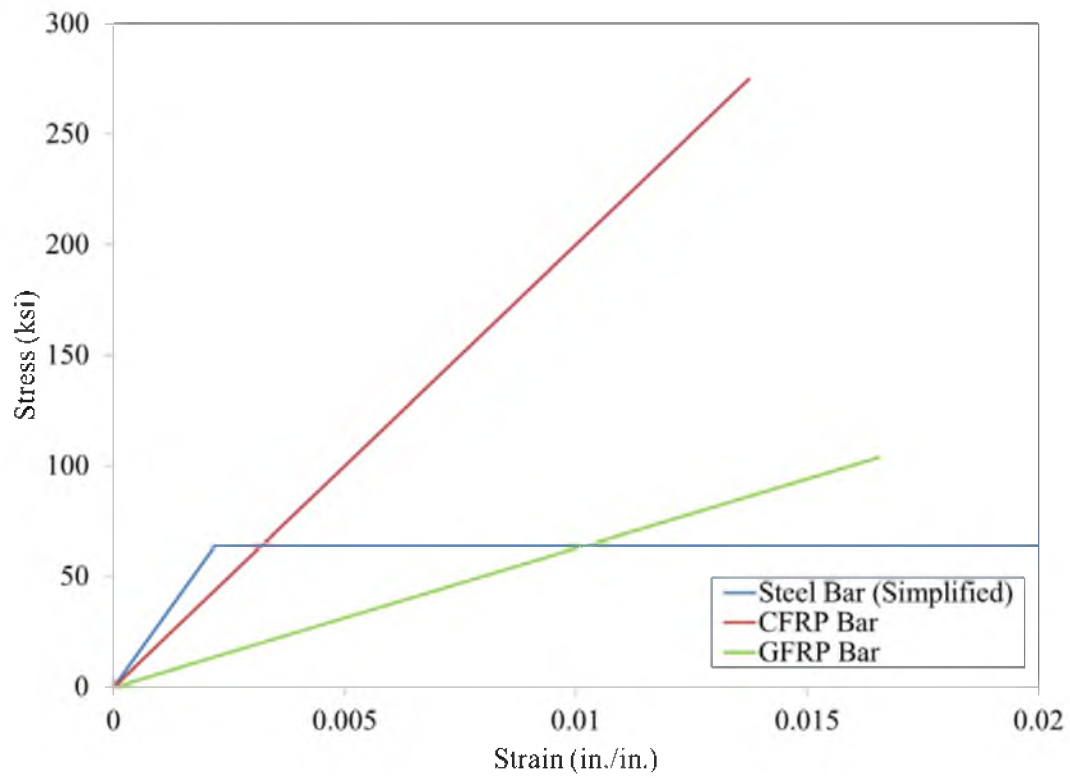


Figure 3.16: Simplified stress-strain curves for steel, CFRP, and GFRP reinforcement

## CHAPTER 4

### ANALYTICAL BUCKLING MODEL FOR SLENDER FRP- SPIRAL-CONFINED CIRCULAR COLUMNS

An analytical model, based on a numerical integration method, has been developed to describe the load-deflection (axial load vs. lateral deflection) behavior for slender FRP-spiral-confined circular columns. The proposed method of analysis is based on the numerical integration method originally proposed by Newmark (1943) and widely adopted in the analysis of steel columns (Shen and Lu 1983), reinforced concrete columns (Pfrang and Siess 1961; Cranston 1972) and composite columns (Choo et al. 2006; Tikka and Mirza 2006).

Jiang and Teng (2012) used this approach to develop an analytical load-deflection model for analyzing slender circular columns confined with external FRP reinforcement (FRP wrap). The incorporation of the Lam and Teng (2003) stress-strain model enabled them to produce reasonable predictions of load-deflection behavior of externally FRP-confined slender columns with respect to actual test results. A similar approach was taken in the present study to develop an analytical load-deflection model for analyzing slender circular columns confined with internal FRP-spiral reinforcement.

#### 4.1 Column Cross-Sectional Analysis

The first step to adapting the numerical integration method is the need to incorporate a cross-sectional analysis of the concrete column. A column that is subjected to combined bending and axial compression experiences a cross-sectional strain gradient. In the traditional analysis of conventional steel reinforced concrete columns it is commonly assumed that the stress-strain curve of the concrete in an eccentrically loaded column is the same as that of concrete under concentric compression. It can reasonably be assumed that this assumption would also apply to concrete columns reinforced with internal FRP reinforcement.

As a result the cross-sectional analysis procedure will be similar to that used for conventional steel reinforced concrete columns, the only difference being the incorporation of a stress-strain curve that represents the type of column being analyzed. Chapter 3 provides a proposed stress-strain model for internal FRP-spiral-confined concrete columns that can be used for this purpose. The cross-section is divided into several small horizontal slices as shown in Figure 4.1 over which numerical integration can be performed to calculate the equilibrium of the section.

Full composite action is assumed to occur between the concrete and reinforcement. Plane sections are assumed to remain plane and the tensile strength of concrete is ignored. Longitudinal reinforcement is incorporated into the horizontal slices that are identified for the analysis. Transverse and confining reinforcement are incorporated indirectly through the stress-strain model used for the analysis.

The axial load  $N$  and bending moment  $M$  carried by the cross-section at any stage of loading can be found by integrating the stresses over the cross-section as shown in

Figure 4.1 as follows:

$$N = \int_{\lambda_c=R-x_n}^R \sigma_c b_c (d\lambda_c) + \sum_{i=1}^n (\sigma_{vi} - \sigma_c) A_{vi} \quad (4.1)$$

$$M = \int_{\lambda_c=R-x_n}^R \sigma_c b_c \lambda_c (d\lambda_c) + \sum_{i=1}^n (\sigma_{vi} - \sigma_c) A_{vi} (R - d_{vi}) \quad (4.2)$$

where  $b_c$  is the width of the section at a distance  $\lambda_c$  from the reference axis (R.A.),  $R$  is the column radius, and  $x_n$  is the depth of the neutral axis (N.A.).  $\sigma_{vi}$  is the stress in the  $i^{\text{th}}$  slice of longitudinal reinforcement with  $d_{vi}$  being the corresponding distance from the reference axis and  $A_{vi}$  the corresponding cross-sectional area of the longitudinal reinforcement. The compressive stress of concrete  $\sigma_c$  can be determined from the appropriate concrete stress-strain model that is being used for the column as previously described. Likewise the stress of the reinforcement  $\sigma_{vi}$  can be determined from appropriate stress-strain models based on the material properties of the reinforcement being used. Eqs. (4.1) and (4.2) are applicable for any stage of loading. When the strain at the extreme concrete compression fiber reaches the maximum axial strain of the stress-strain model for the concrete, then it is assumed that the ultimate limit state of the column has been reached due to crushing failure of the concrete. Likewise, if the capacity of the tension elements of the section is unable to develop the force required to resist the moment demand, then it is assumed that the ultimate limit state of the column has been reached due to tension failure of the reinforcement.

## 4.2 Slender Column Buckling Model

The analytical model used allows for the consideration of eccentric loads applied at both ends of the column. Pinned-pinned end conditions were used for the analysis, which simulated the manner in which the specimens of the present study were tested in the lab. The analytical model and numerical integration methodology used are explained in the following sections.

### 4.2.1 General Approach

Four basic steps were utilized in applying the numerical integration method for the analytical model of analyzing slender columns, which followed a similar approach utilized by Jiang and Teng (2012) in their study of slender columns with FRP confining wraps. The approach presented by Jiang and Teng (2012) was adapted for the present study to be used for slender columns utilizing internal FRP-spirals as well as internal FRP and steel longitudinal bars. The steps are as follows:

1. Divide the column length ( $L$ ) equally into a desirable number of segments with each given a length  $\Delta L$  as shown in Figure 4.2.
2. Identify a reference grid point at each end of each segment and divide the cross-section of the column into a desirable number of slices parallel to the column axis as shown in Figure 4.1. This allows for the use of the cross-sectional analysis methodology as described in Section 4.1.
3. For a given axial load, find the lateral displacement at each grid point in an iterative manner through the axial load-moment-curvature relationship, the cross-sectional analysis and the numerical integration function of the column.

4. Obtain the full load-deflection (axial load vs. lateral deflection) curve of the column by repeating Step 3 in an incremental manner, using either a force-controlled or deflection-controlled method, over the full range of axial loads for the column.

The force-controlled method uses an iteration method that increases the axial load by small increments, whereas the deflection-controlled method uses an iteration method that increases the deflection of a particular grid point by small increments. It was found that it was more effective to use the force-controlled method for developing the ascending branch of the load-deflection curve, while it was more effective to use the deflection-controlled method for developing the descending branch of the curve. This approach essentially provides a representation of a column's attempt to follow a load-deflection path utilizing the minimum amount of strain energy.

This numerical integration methodology was incorporated in the present study utilizing a computer program developed with the Microsoft Excel 2010 Visual Basic for Applications programming language. The accuracy of the analysis is affected by a number of factors such as the number of segments the column is divided into, the number of horizontal slices the cross-section is divided into, and the tolerances adopted in the analysis. For the models in this study the column cross-sections were divided into at least 12 horizontal slices and the column height was divided into at least 12 segments, which was found to provide refined enough results without incurring unnecessarily excessive computer run-times.

The two key elements for generating the full range load-deflection curve are the axial load-moment-curvature relationship and the numerical integration function, which

will be discussed in greater detail in the following sections.

#### 4.2.2 Axial Load-Moment-Curvature Relationship

The axial load-moment-curvature relationship is the first of the two key elements required for the numerical integration method. A specific moment-curvature curve can be created for a given column cross-section subjected to a given axial load  $N$ . This curve can be developed using the cross-section analysis approach as described in Section 4.1. Figure 4.3 shows an example of two moment-curvature curves derived for a sample column for two different axial load conditions. This is typically generated by specifying a number of reasonable strain values for the extreme compression fiber of concrete  $\varepsilon_c$  up to its ultimate compressive strain  $\varepsilon'_{cc}$  for a given axial load. For each selected strain value the depth of the neutral axis  $x_n$  is varied until the applied axial load  $N$  equals the resultant axial force acting on the cross-section as calculated from Eq. (4.1). For purposes of the present study, it was assumed that the solution process converged when the difference between the applied axial load and the resultant axial load was within 0.4 lbs. Once the neutral axis  $x_n$  is determined, the bending moment  $M$  can be calculated from Eq. (4.2), and the curvature  $\phi$  can be calculated from Eq. (4.3) as depicted in Figure 4.1:

$$\phi = \frac{\varepsilon_c}{x_n} \quad (4.3)$$

As shown in Figure 4.1  $f'_{cc}$  is the maximum attainable stress at the ultimate compressive strain  $\varepsilon'_{cc}$  as determined by the stress-strain model used for the analysis. For the columns of the present study, the stress-strain model used was based on the confinement

model derived in Chapter 3.

#### 4.2.3 Numerical Integration Function for Column Deflection

The numerical integration function is the second of the two key elements required for the numerical integration method. This is derived using the assumption that the lateral deflection of the column is very small compared to the total height of the column. Therefore, curvature can be taken as the second order derivative of the lateral deflection of the column. Using the central difference equation, Jiang and Teng (2012) derived the relationship between the lateral deflection and the curvature to be

$$-\phi_{(i)} = \frac{f_{(i+1)} - 2f_{(i)} + f_{(i-1)}}{(\Delta L)^2} \quad (4.4)$$

where  $\phi_{(i)}$  and  $f_{(i)}$  are the curvature and lateral deflection at the  $i^{\text{th}}$  grid point, respectively, and  $i = 2, 3, \dots, (m - 1)$ . In Eq. (4.4)  $i$  is the index of the grid point and  $(m - 1)$  is the number of segments that the column has been equally divided into as shown in Figure 4.2. For convenience Eq. (4.4) can be rewritten as

$$f_{(i+1)} = 2f_{(i)} - f_{(i-1)} - \phi_{(i)}(\Delta L)^2 \quad (4.5)$$

which is the numerical integration function used to find the lateral deflection of the column.

#### 4.2.4 Deriving the Ascending Branch of the Load-Deflection Curve

The ascending branch of the load-deflection curve is generated through a method of increasing the axial load by small increments. For a given axial load  $N$ , the first order moment at each grid point can be calculated as

$$M_{1,(i)} = N \cdot e_{(i)} \quad (4.6)$$

where  $M_{1,(i)}$  and  $e_{(i)}$  are the first order moment and the initial eccentricity at the  $i^{\text{th}}$  grid point, respectively. The initial eccentricity follows a linear distribution between  $e_{(1)}$  and  $e_{(m)}$ , where  $e_{(1)} = e_1$  and  $e_{(m)} = e_2$  as shown in Figure 4.2. If the lateral deflection  $f_{(i)}$  of the column is known, the second order moment can be expressed as

$$M_{2,(i)} = N \cdot f_{(i)} \quad (4.7)$$

resulting in the total moment given by

$$M_{(i)} = M_{1,(i)} + M_{2,(i)} = N(e_{(i)} + f_{(i)}) \quad (4.8)$$

To begin the process of the analysis, a value for  $f_{(2)}$  needs to be assumed. This assumed value can be zero or any reasonably small value. At this grid point, the bending moment  $M_{(2)}$  can be determined from Eq. (4.8), and the associated curvature  $\phi_{(2)}$  can be found through the cross-sectional analysis and Eq. (4.3). Moment-curvature curves can be derived from the cross-sectional analysis, which provides the relationship needed between moment and curvature as shown in the example of Figure 4.3. Knowing that  $f_{(1)} = 0$  at the pinned end of the column and having obtained values for  $M_{(2)}$  and  $\phi_{(2)}$ , the lateral displacement of grid point  $f_{(3)}$  can be calculated using Eq. (4.5). This procedure can be repeated to obtain the lateral deflection of the remaining grid points  $f_{(4)}$  through  $f_{(m)}$ . Once  $f_{(m)}$  is calculated it needs to be examined to see if it is equal to zero ( $f_{(m)} = 0$ ) since it is located at the other pinned end of the column. If this is the case then the column is in equilibrium, and the correct lateral deflection of the column has been found. If  $f_{(m)} \neq 0$ , then the assumed value for  $f_{(2)}$  needs to be adjusted and the procedure

repeated until  $f_{(m)} = 0$  is satisfied. Shen and Lu (1983) suggested the new value of  $f_{(2)}$  could be taken as

$$f_{(2)}(new) = f_{(2)}(previous) - \frac{f_{(m)}}{m-1} \quad (4.9)$$

For the present study, the solution was considered to be acceptable if the calculated value of  $f_{(m)}$  was less than  $10^{-6}$  in.

This analysis procedure works to determine the lateral deflection of a column for a single value of axial load. To create the full ascending branch of the load-deflection curve, the procedure needs to be repeated for a series of successively increasing load increments. The methodology proposed by Jiang and Teng (2012) for selecting the load increments was also used for the present study. This consisted of selecting an initial load increment of  $0.1N_{u1}$ , where  $N_{u1}$  is the axial load capacity of the column section when subjected to concentric compression given as

$$N_{u1} = f'_{cc} A_{nc} + f_y A_v \quad (4.10)$$

where  $A_{nc}$  is the net cross-sectional area of the concrete (total column cross-section minus  $A_v$ ),  $A_v$  is the area of longitudinal reinforcement,  $f'_{cc}$  is the maximum concrete compressive strength, and  $f_y$  is the yield or maximum strength of the longitudinal reinforcement.

Eventually the situation occurs where the applied load exceeds the maximum moment that the column can sustain. This occurs when the moment at any grid point as calculated by Eq. (4.8) exceeds the maximum moment allowed as calculated by the cross-sectional moment-curvature analysis for the given load. When this is the situation, the

iteration process needs to restart from the previous load level, and the load increased by a smaller load increment of  $0.01N_{u1}$  for subsequent load steps. Once again, the situation will occur where the applied load exceeds the maximum moment that can be sustained by the column, at which time the same procedure needs to repeat again with another reduced load increment by a factor of 10. This process repeats until the load increment is eventually reduced to  $10^{-6}N_{u1}$ . The maximum load for which a convergent solution of the lateral deflection can be found is then taken to be the axial load capacity of the column  $N_u$ .

To assist in the generation of the descending branch of the load-deflection curve, the corresponding value of  $f_{(2)}$  for the maximum converging load  $N_u$  is recorded as a reference displacement value  $f_{ref}$  such that  $f_{ref} = f_{(2)}$ .

#### 4.2.5 Deriving the Descending Branch of the Load-Deflection Curve

A column's load-deflection curve does not always have a descending branch but typically does if a column is slender enough to experience a stability failure. If this is the case, the descending branch of the load-deflection curve is generated through a method of increasing the deflections by small increments beyond what was obtained from the ascending branch of the curve. The procedure is similar to that used for generating the ascending branch with the main difference being that the goal is to find the correct axial load for a given value of  $f_{(2)}$ . This is described in more detail in what follows using the procedure proposed by Jiang and Teng (2012).

An initial deflection increment of  $0.1f_{ref}$  is used resulting in a prescribed value of

$f_{(2)}$  such that  $f_{(2)} = 1.1f_{ref}$ . The value of  $N_u$  from the ascending branch calculation can be used as the initial assumed value for the corresponding axial load. The procedure described in the previous section, Section 4.2.4, can be used to calculate the corresponding deflected configuration, which should result in a negative calculated value for  $f_{(m)}$  because the actual axial load must be smaller than  $N_u$ . The assumed axial load is then successively reduced at increments of  $0.01N_u$  until a positive calculated value for  $f_{(m)}$  is achieved. Once a positive calculated value is achieved, the correct axial load can then be determined by using the bisection method. This is accomplished by setting the last two assumed values of the axial load to be the upper and lower bounds in the bisection method. Figure 4.4 shows this method for the first increment. The example shown in the figure follows the following methodology:

1. Find PT. 1 where  $f_{(2)} = 1.1f_{ref}$  and  $N = N_u$ 
  - a.  $f_m(N_u)$  is negative; therefore, descending branch exists. Continue iteration by decreasing axial load by  $0.01N_u$ .
2. Find PT. 2 where  $f_{(2)} = 1.1f_{ref}$  and  $N = 0.99N_u$ 
  - a.  $f_m(0.99N_u)$  is negative; therefore, continue iteration by decreasing axial load by  $0.01N_u$ .
3. Find PT. 3 where  $f_{(2)} = 1.1f_{ref}$  and  $N = 0.98N_u$ 
  - a.  $f_m(0.98N_u)$  is positive; therefore, curve occurs between PT. 2 and PT. 3. Initiate bisection method between PT. 2 and PT. 3. Increase axial load half way between PT. 2 and PT. 3 by  $0.005N_u$ .
4. Find PT. 4 where  $f_{(2)} = 1.1f_{ref}$  and  $N = 0.985N_u$

- a.  $f_m(0.985N_u)$  is positive; therefore, continue bisection method between PT. 2 and PT.4. Increase axial load half way between PT. 2 and PT. 4 by  $0.0025N_u$ .
5. Find PT. 5 where  $f_{(2)} = 1.1f_{ref}$  and  $N = 0.9875N_u$
- a.  $f_m(0.9875N_u)$  is negative but is within convergence tolerance; therefore, use values at PT. 5 as the converged axial load and deflection values.

The axial load calculated from this method is the solution for the current deflection increment and is used as the initial value for the next increment.

Eventually the situation occurs where the analysis is unable to find a convergent solution. This occurs when the moment at any grid point as calculated by Eq. (4.8) exceeds the maximum moment allowed as calculated by the cross-sectional moment-curvature analysis for the given axial load. When this is the situation, the iteration process needs to restart from the previous value of  $f_{(2)}$  and increased by a smaller deflection increment of  $0.01f_{ref}$ . The entire process is repeated until the increment is reduced to  $10^{-6}f_{ref}$ .

### 4.3 Slender Column Analytical Buckling Model Verification

The analytical buckling model developed for the present study was compared against other studies to verify the accuracy of the model. It was first compared against the analytical buckling model of Cranston (1972) for square columns. Next it was compared against the experimental tests performed on square columns by Kim and Yang (1995) and Claeson and Gylltoft (1998). It was then desired to check the model for use with circular columns. Analytical results for circular columns were not available in

Cranston's analysis, so the present model was compared against experimental tests performed on circular columns by Fitzwilliam and Bisby (2006) and Ranger and Bisby (2007).

It should be noted that many variables can affect the accuracy of the results of an experimental test, which should be considered when attempting to replicate an experimental test with a theoretical model. Some of the variables of an experimental test that can affect the accuracy of the results include the setup of the data collection system, the setup of the testing configuration and how accurately it represents theoretical conditions (i.e., pinned-pinned end conditions, eccentricity, etc.), the procedures for conducting the test, the uniformity and quality of the construction of the specimens and materials, and so forth.

Some of the variables that can affect the accuracy of the results of a theoretical model were previously mentioned in Section 4.2.1, but the accuracy also depends on the accuracy of the representation of materials, construction, and setup (i.e., stress-strain curve, concrete and steel strength, reinforcement location, etc.) used in the model compared to that used in the test.

#### 4.3.1 Model Verification with Cranston (1972) Analytical Model

The present model, and its numerical implementation, was first verified against the numerical results of the analytical model of Cranston (1972), which was based on a similar numerical integration approach. Cranston's analysis similarly consisted of finding successive solutions as the load or deflection of the column is increased in steps. The successive solutions were solved in an iterative manner where the column was

segmented, initial proposals made for the deflected shape of the column, and bending moments computed for each end of the segment. The curvature at each end of the segment was computed using an iterative process where the cross-section is divided into slices and then compared with the computed bending moments. After computing the curvatures at all segment ends the deflected shape is calculated and compared with that initially proposed. If they agree, then convergence is assumed; otherwise the process is iterated again.

Four square columns were used for comparison with a cross-section as shown in Figure 4.5 and properties as shown in Table 4.1 as presented in Cranston's study. Table 4.2 shows a more detailed breakout of the actual properties used with the present model. The stress-strain curves used in Cranston's study for concrete and steel reinforcement are shown in Figure 4.6 and were similarly incorporated in the present model. These columns had pinned-pinned end conditions and were eccentrically loaded on one end only.

Cranston (1972) normalized the load-deflection curves using reference values. The midheight lateral deflection of the column was normalized by the depth of the section ( $d = 12$  in.), and the axial load was normalized by the concentric compression axial load capacity  $N_{uo}$  where

$$N_{uo} = f_{c\_design} A_{nc} + f_{y\_design} A_s \quad (4.11)$$

$f_{c\_design}$  is the concrete design strength where

$$f_{c\_design} = \frac{f'_{cc}}{1.5} = 2,000 \text{ psi} \quad (4.12)$$

and  $f_{y\_design}$  is the steel design strength where

$$f_{y\_design} = \frac{f_y}{1.15} = 52,174 \text{ psi} \quad (4.13)$$

as identified in Cranston's study.  $A_{nc}$  and  $A_s$  are the net cross-sectional area of the concrete (total column cross-section minus  $A_s$ ) and area of the steel reinforcement, respectively. Based on this information the normalizing value of  $N_{uo}$  used with the present model for the comparison was  $N_{uo} = 721,500$  psi.

The comparison between the present model and Cranston's study are shown in Figures 4.7 through 4.10 for columns Cranston1 through Cranston4. As can be seen, the values of the present model are in excellent agreement with the values from Cranston (1972) for both material failure (Figures 4.7 and 4.8) and stability failure (Figures 4.9 and 4.10) for rectangular/square columns.

#### 4.3.2 Model Verification with Kim and Yang (1995) Experimental Results

The present model was next compared with the experimental results of Kim and Yang (1995). Thirty square columns were tested in their study having a wide range of concrete strength. Two columns were used for comparison to the present model. The column cross-sections had a width and depth of 3.15 in. (80 mm) with one column having a length of 4.724 ft (1440 mm) and the other column having a length of 7.874 ft (2400 mm). They were reinforced with four longitudinal steel bars each having an area of 0.05 in.<sup>2</sup> (32 mm<sup>2</sup>). They were tested with pinned-pinned end conditions. Table 4.3 provides additional information regarding the column construction as tested and modeled. The column cross-section is similar to that of Cranston's columns shown in Figure 4.5. The

Todeschini et al. (1964) stress-strain curve was assumed for concrete with  $\varepsilon_{cu} = 0.003$  in./in., and a simplified elastic-plastic stress-strain curve was assumed for reinforcing steel as shown in Figure 4.11.

Due to differences often found between the concrete strengths of cylinder tests and actual member tests, the maximum concrete stress of Todeschini's stress-strain curve is typically taken as  $f'_{cc} = 0.9f'_c$ . Due to the observation that Kim and Yang's tests for these columns were potentially obtaining a maximum concrete stress closer to  $f'_{cc} \approx f'_c$ , two load-deflection curves were developed with the present model: first, where  $f'_{cc} = 0.9f'_c$  and second, where  $f'_{cc} = f'_c$ . Comparisons between the present model and Kim and Yang's tests are shown in Figures 4.12 and 4.13. As can be seen in these figures, the present model provides reasonable agreement with the selected tests of Kim and Yang (1995).

#### 4.3.3 Model Verification with Claeson and Gylltoft (1998) Experimental Results

The experimental tests of Claeson and Gylltoft (1998) were also compared with the present model. Claeson and Gylltoft performed experimental tests on 12 square columns with varying concrete strengths and configurations. Six columns were used for comparison to the present model. The first two columns, CG23 and CG24, had a cross-section width and depth of 4.724 in. (120 mm) and a length of 7.87 ft (2,400 mm). The next two columns, CG27 and CG28, had a cross-section width and depth of 7.874 in. (200 mm) and a length of 9.84 ft (3,000 mm). The last two columns, CG31 and CG32, had a cross-section width and depth of 7.874 in. (200 mm) and a length of 13.12 ft

(4,000 mm).

Columns CG23 and CG24 were reinforced with four longitudinal steel bars each having an area of  $0.18 \text{ in.}^2$  ( $113 \text{ mm}^2$ ) and with steel ties having an area of  $0.04 \text{ in.}^2$  ( $28 \text{ mm}^2$ ) spaced at 3.94 in. (100 mm) for CG23 and at 7.09 in. (180 mm) for CG24.

Columns CG27, CG28, CG31, and CG32 were reinforced with four longitudinal steel bars each having an area of  $0.31 \text{ in.}^2$  ( $201 \text{ mm}^2$ ) and with steel ties having an area of  $0.08 \text{ in.}^2$  ( $50 \text{ mm}^2$ ) spaced at 5.11 in. (130 mm) for CG27 and CG31 and at 9.45 in. (240 mm) for CG28 and CG32.

All columns were tested with pinned-pinned end conditions. Table 4.4 provides additional information regarding the column construction as tested and modeled. The column cross-section is similar to that of Cranston's columns shown in Figure 4.5. The Todeschini et al. (1964) stress-strain curve was assumed for the concrete with  $\epsilon_{cu} = 0.003$  in./in., and a simplified elastic-plastic stress-strain curve was assumed for the reinforcing steel as shown in Figure 4.11. Similar to the Kim and Yang's tests, two load-deflection curves were developed with the present model: first, where  $f'_{cc} = 0.9f'_c$ , and second, where  $f'_{cc} = f'_c$ . The comparison between the present model and Claeson and Gylltoft's tests are shown in Figures 4.14 through 4.16. As can be seen in the figures the present model provides reasonable agreement with the selected tests of Claeson and Gylltoft (1998).

#### 4.3.4 Model Verification with Fitzwilliam and Bisby (2006) Experimental Results

Fitzwilliam and Bisby (2006) conducted experimental tests on several circular columns for the purpose of evaluating the behavior of FRP wraps on these columns. Two of 18 columns from this study were selected for comparison to the present model because they were tested without FRP-wrap confinement and had load-deflection data provided.

The columns were circular with a diameter of 6 in. (152 mm), a length of 3.9 ft (1200 mm), and were loaded with an eccentricity of 0.787 in. (20 mm). They were reinforced with four longitudinal steel bars having a bar diameter of 0.25 in. (6.4 mm) and with steel circular ties having a bar diameter of 0.25 in. (6.4 mm) spaced at 3.94 in. (100 mm). They were tested with pinned-pinned end conditions. Table 4.5 provides the details for the column construction as tested and as modeled, and Figure 4.17 shows the column cross-section configuration used in the present model.

The concrete strength was not reported in the article of Fitzwilliam and Bisby (2006), but Jiang and Teng (2012) also used this study to compare values of their model and was able to determine that the maximum concrete strength of the columns without the FRP wrap was 35.5 MPa (5,150 psi). For purposes of this study, this concrete strength was used so that the maximum concrete stress on the stress-strain curve was used as  $f'_{cc} = 5,150$  psi. The Todeschini et al. (1964) stress-strain curve was assumed for the concrete with  $\epsilon_{cu} = 0.003$  in./in., and a simplified elastic-plastic stress-strain curve was assumed for the reinforcing steel as shown in Figure 4.11.

The comparison between the present model and Fitzwilliam and Bisby's tests is shown in Figure 4.18. The present model represents a reasonable agreement with the

tests of Fitzwilliam and Bisby (2006) considering that this is a comparison of a theoretical model to that of actual experimental tests with a somewhat unknown concrete compressive strength. With regards to the potential variability of results in experimental tests, this can be seen with the varying test results shown between columns FB-1 and FB-2 in Figure 4.18, which were technically constructed identically to each another. Also, depending on the test setup, it was found and discussed in Section 2.5 that the circular loading surface of a circular column can affect the actual eccentricity transferred to the column, therefore affecting the final results.

#### 4.3.5 Model Verification with Ranger and Bisby (2007) Experimental Results

Ranger and Bisby (2007) conducted additional experimental tests on circular columns for the purpose of further evaluating the behavior of FRP wraps on these columns. Jiang and Teng (2012) also incorporated these tests in their study. Five of 14 columns from Ranger and Bisby's tests were selected for comparison to the present model. The columns selected also did not contain FRP-wrap confinement and had load-deflection data provided to enable a comparison to data from the present model.

The columns were circular with a diameter of 6 in. (152 mm) and a length of 1.97 ft (600 mm). They were reinforced with four longitudinal steel bars having a bar diameter of 0.25 in. (6.4 mm) and with steel circular ties having a bar diameter of 0.25 in. (6.4 mm) spaced at 3.94 in. (100 mm). They were loaded with varying eccentricities of 0.197 in. (5 mm), 0.394 in. (10 mm), 0.787 in. (20 mm), 1.181 in. (30 mm), and 1.575 in. (40 mm). They were tested with pinned-pinned end conditions. Table 4.6 provides the details for the column construction as tested and modeled and Figure 4.17 shows the

column cross-section configuration used in the present model.

The cylinder concrete strength was reported to be  $f'_c = 4,815$  psi. Due to the observation that Ranger and Bisby's tests for these columns were generally obtaining lower maximum concrete stresses (as compared to the cylinder test), two load-deflection curves were developed with the present model: first, where  $f'_{cc} = 0.9f'_c$ , and second, where  $f'_{cc} = 0.85f'_c$ . The 0.85 factor is also commonly used when converting cylinder concrete strengths to actual member concrete strengths and appears to produce a better representation of the results reported by Ranger and Bisby (2007). The Todeschini et al. (1964) stress-strain curve was assumed for the concrete with  $\epsilon_{cu} = 0.003$  in./in., and a simplified elastic-plastic stress-strain curve was assumed for the reinforcing steel as shown in Figure 4.11.

Comparisons between the present model and Ranger and Bisby's tests are shown in Figure 4.19. The present model represents a reasonable agreement with the tests of Fitzwilliam and Bisby (2006) again considering that this is a comparison of a theoretical model to that of actual experimental tests.

#### 4.3.6 Model Comparison with the Experimental Results of the Present Study

The model developed was used to simulate the results of the experiments of the tall columns conducted in the present study. Chapter 2 describes the construction details of these columns. As reported, these columns had a 12 in. diameter and 12 ft 3 in. height with a concrete strength  $f'_{cc} = 13,000$  psi. For purposes of the analysis, an additional height of 8 in. was added to the column height (12 ft 11 in.) to account for the extra 4 in.

from both the top and bottom of the column to the center of the roller assembly to properly account for the full pinned-pinned height as tested. Also, the column cross-section was divided into 12 slices, and the column height was divided into 12 segments for the analysis which was found to provide a reliable discretization for the model.

#### 4.3.6.1 Load-Deflection Curves #4T-DB1, #5T-SS1, and #6T-SG1

The present model was used to simulate the results of the experiments for columns #4T-DB1, #5T-SS1, and #6T-SG1. As shown in Table 2.2, the recorded maximum concrete strain at failure for these columns was just over 0.003 in./in. for axial strain and between 0.0004 in./in. and 0.0007 in./in. for radial strain. A confinement model analysis was first performed according to Chapter 3, which found the confined concrete strength,  $f'_{cc}$ , to be equal to the unconfined concrete strength,  $f'_{co}$  ( $f'_{cc} = f'_{co} = 13,000$  psi) with essentially no gain in axial strength capacity due to confinement. This was also observed in the tests where the average maximum stress obtained in the short columns was 13,192 psi, or approximately 13,000 psi, which can be partially attributed to the use of high-strength concrete as was manifested by the low radial strains achieved in

the spirals. The  $\frac{f'_{cc}}{f'_{co}}$  ratio derived from the present study's confinement model was

equal to 1.0 for the SS and SG columns utilizing a single spiral and 1.01 for the DB columns utilizing a double spiral. Similar to the observation discussed with Eq. (3.48), this effectively amounts to no increase in axial strength due to the low levels of confinement provided. So, for purposes of this model, the Popovics stress-strain curve was defined with  $f'_{cc} = f'_{co} = 13,000$  psi as the maximum stress, and based on the

observed strains from the tests,  $\varepsilon'_{\infty} = 0.003$  in./in. was used as the maximum axial strain.

These columns were loaded with an eccentricity of 1 in. As discussed in Section 2.5, based on the limitations and imperfections of the test setup, it is likely that the column did not undergo a loading truly at a 1 in. eccentricity. Due to the 2 in. thick steel plate placed on top and bottom of the column, and due to the circular cross-section of the column, the effective eccentricity of the load as it was distributed to the column was likely less than 1 in. Figure 4.20 shows the assumption used for the present study. As shown, it was assumed that the load could transfer through the steel plate up to an additional 2 in. on either side of the greased steel roller assembly due to the 2 in. thickness of the steel plate. Based on the circular loading surface of the column, this results in an approximate calculated effective eccentricity of 0.81 in.

The load-deflection curves using the present model for these columns are shown in Figures 4.21 through 4.24. As shown, curves for both a 1.00 in. eccentricity and an effective 0.81 in. eccentricity have been presented for comparison. Also, two curves are presented for the experimental test: the first according to the data collected in the actual test and the second with the upper portion of the curve transposed 0.4 in. according to the reasoning described in Section 2.5 due to the limitations and imperfections of the test setup (i.e., unparallel bearing interfaces that adversely influence the deflection and thick bearing plates that can disperse load to the opposite side of the intended load placement for small eccentricities). The lower portion of the transposed curve was extrapolated and filled in based on what might be expected due to the shape of the upper portion of the curve.

During the testing phase of these columns, it was observed after the failure of

column #5T-SS1 that the 3 in. steel base of the testing frame had shifted in the opposite direction of the eccentricity approximately 0.5 in. due to the force of the testing failure from the preceding column #4T-DB1 and/or column #5T-SS1. This part of the testing setup was not expected to move, so it was not checked before the testing of column #5T-SS1; thus it is not certain whether column #5T-SS1 was out of plumb (in-plane) the full 0.5 in. or not during its test. It could, however, be a factor as to why in Figure 4.22 the transposed experimental test curve matches the 1.00 in. eccentricity more closely than the 0.81 in. eccentricity as opposed to the curves in Figures 4.21 and 4.23, which match the 0.81 in. eccentricity more closely.

As seen in the figures, the analytical curves developed from the present model produces a similar representation of the experimental curves when considering the transposed curve. Figure 4.24 shows a side-by-side comparison of the modeled curves using the 0.81 in. eccentricity. It can be seen that there is very little differentiation between the three. This is due to the fact that at this low eccentricity, the failure is governed by a material compressive failure. As a result, the slight difference in the maximum axial load is probably due to the difference between the contributions of compressive strength from the longitudinal reinforcement in conjunction with the compressive strength of the concrete. Interestingly, the Type DB column with both steel and GFRP longitudinal bars shows a slightly lower axial load capacity than the Type SS column with only steel longitudinal bars likely because the area from GFRP bars contributes less to the compressive strength than when that area is replaced with concrete.

#### 4.3.6.2 Load-Deflection Curves #7T-DB4, #8T-SS4, and #9T-SG4

The present model was used to simulate the results of the experiments for columns #7T-DB4, #8T-SS4, and #9T-SG4. As shown in Table 2.2, the recorded maximum strains at failure for these columns was between 0.003 in./in. and 0.004 in./in. for the axial strain and between 0.0006 in./in. and 0.001 in./in. for the radial strain. A confinement model analysis was first performed according to Chapter 3, in which it was found that the confined concrete strength,  $f'_{cc}$ , was equal to the unconfined concrete strength,  $f'_{co}$  ( $f'_{cc} = f'_{co} = 13,000$  psi). As mentioned in the previous section, this was also observed in the tests where the average maximum stress obtained in the short columns was 13,192 psi, which can be partially attributed to the use of high-strength concrete as was manifested by the low radial strains achieved in the spirals. The  $\frac{f'_{cc}}{f'_{co}}$  ratio derived from the present study's confinement model was equal to 1.0 for the SS and SG columns utilizing a single spiral and 1.01 for the DB columns utilizing a double spiral. Similar to the observation discussed with Eq. (3.48), this effectively counts for no increase in axial strength due to the low levels of confinement provided. So, for purposes of this model, the Popovics stress-strain curve was defined with  $f'_{cc} = f'_{co} = 13,000$  psi as the maximum stress, and based on the observed strains from the experimental tests,  $\epsilon'_{cc} = 0.004$  in./in. was used as the maximum strain.

These columns were loaded with an eccentricity of 4 in. As discussed in Section 2.5, based on the limitations and imperfections of the test setup, it is likely that the column did not undergo a loading truly at a 4 in. eccentricity. Due to the 2 in. thick steel

plate placed on top and bottom of the circular column, the effective eccentricity of the load as it was distributed to the column was less than 4 in. Figure 4.25 shows the assumption used for the present study. It was assumed that the load transfer through the 2 in. thick steel plate could extend up to 2 in. on either side of the greased steel roller assembly, but would also be an equal distance on either side. Since the edge of the greased steel roller assembly aligned with the edge of the column for this situation, it was assumed to transfer through at the same width as that of the greased steel roller assembly. Based on the loading surface of the column, this results in an approximate calculated effective eccentricity of 3.66 in.

The load-deflection curves using the present model for these columns are shown in Figures 4.26 through 4.29. As shown, curves for both a 4.00 in. eccentricity and an effective 3.66 in. eccentricity have been presented for comparison. As seen in the figures, the analytical curves developed from the present model produce a similar representation of the experimental curves especially when using the effective eccentricity of 3.66 in. In Figure 4.27, the model also helps conveniently fill in the lost information from the experimental test of column #8T-SS4 due to the voltage supply malfunction, helping to fill in what the remainder of the curve should look like. It is interesting to note in this figure how the maximum load from the test (205,600 lbs.) matches fairly closely with the maximum load obtained from the model (206,380 lbs. at a 1.59 in. deflection) using the effective eccentricity of 3.66 in.

Figure 4.29 shows a side-by-side comparison of the modeled curves using the 3.66 in. eccentricity. It can be seen that there is a greater differentiation between the three columns as opposed to the curves for the 0.81 in. eccentricity in Figure 4.24. This

is due to the fact that these columns are governed by a stability failure. These curves give a nice comparison as to the contributing effect of the different types of longitudinal reinforcement in the overall load and deflection capacity of the columns.

As seen, the column with all-GFRP longitudinal reinforcement (#9T-SG4,  $\rho = 1.65\%$ ) is not able to achieve as large of an axial load as the other two columns that have steel longitudinal reinforcement due to the lower compressive strength contribution provided by the GFRP bars. However, the high tensile, elastic characteristics of the GFRP longitudinal bars enable the column to maintain its maximum axial load capacity over a larger range of lateral deflections because its contribution in tensile strength can continue to increase with increased moment-curvature demand due to the larger deflection.

On the other hand, the column with all-steel longitudinal reinforcement (#8T-SS4,  $\rho = 1.06\%$ ) is able to achieve a greater axial load than the column with all-GFRP (#9T-SG4) due to the higher compressive strength contribution provided by the steel bars; however, once the maximum load is achieved, the column begins to lose load capacity with increased deflection (i.e., increased moment-curvature demand) because the longitudinal steel contribution in tensile strength is limited to the maximum yield strength.

The column with both steel and GFRP longitudinal reinforcement (#7T-DB4,  $\rho = 2.71\%$ ) is able to get the best of both worlds with an increased axial load capacity while also maintaining the maximum load over an extended range of lateral deflection until ultimate failure occurs.

#### 4.3.6.3 Axial Load-Moment Interaction Curves DB, SS, and SG Columns

The present model was used to create axial load-moment interaction curves for the DB, SS, and SG columns of the present study.  $f'_{cc} = f'_{co} = 13,000$  psi and  $\epsilon'_{cc} = 0.003$  in./in. was used as the maximum stress and strain, respectively.

Figure 4.30 shows the interaction curve for the DB type column with the modeled load paths for the 0.81 in. and 3.66 in. eccentricities shown along with the actual failure points for all three DB columns from tests in the present study. It should be noted that the plotted failure point for column #4T-DB1 includes the assumed 0.4 in. additional deflection based on the observations as previously discussed. With this consideration, it can be seen in the figure that the three failure points from the tests agree with the predicted interaction curve within statistical expectations.

Figure 4.31 shows the interaction curve for the SS type column with the modeled load paths for the 0.81 in. and 3.66 in. eccentricities shown along with the actual failure points for all three SS columns from tests in the present study. It again should be noted that the plotted failure point for column #5T-SS1 includes the assumed 0.4 in. additional deflection based on the observations as previously discussed. With this consideration, it can be seen in the figure that failure points from the tests agree with the predicted interaction curve within statistical expectations.

Figure 4.32 shows the interaction curve for the SG type column with the modeled load paths for the 0.81 in. and 3.66 in. eccentricities shown along with the actual failure points for all three SG columns from tests in the present study. Once again, it should be noted that the plotted failure point for column #6T-SG1 includes the assumed 0.4 in.

additional deflection based on the observations as previously discussed. With this consideration, it can be seen in the figure that failure points from the tests agree with the predicted interaction curve within statistical expectations.

#### 4.3.6.4 Slender Column Interaction Curves for DB, SS, and SG Columns

The present model was also used to create slender column axial load-moment interaction curves for the DB, SS, and SG columns of the present study for  $kl/r$  slenderness ratios of 0, 25, 50, and 75. The concrete was modeled with  $f'_{cc} = f'_{co} = 13,000$  psi and  $\epsilon'_{cc} = 0.003$  in./in. as the maximum stress and strain, respectively.

Figures 4.33, 4.34, and 4.35 show the slender column interaction curves for the DB, SS, and SG type columns, respectively. It is interesting to note how at zero bending moment the DB and SS columns, which have steel longitudinal reinforcement, attained approximately the same load capacities ( $\approx 1,535$  kips for  $kl/r = 0$ ; 1,490 kips for  $kl/r = 25$ ; 1,350 kips for  $kl/r = 50$ ; and 1,000 kips for  $kl/r = 75$ ) but a larger load capacity than the all-GFRP SG column ( $\approx 1,480$  kips for  $kl/r = 0$ ; 1,430 kips for  $kl/r = 25$ ; 1,290 kips for  $kl/r = 50$ ; and 960 kips for  $kl/r = 75$ ) because of the lower compressive contribution of the GFRP longitudinal bars. On the other hand, it is interesting to note how at zero axial load the DB and SG columns, which have GFRP longitudinal reinforcement, attained larger moment capacities ( $\approx 685$  kips for DB and 530 kips for SG for all  $kl/r$  ratios) as opposed to the SS column ( $\approx 385$  kips for all  $kl/r$  ratios), which only has steel longitudinal reinforcement because of the higher tensile capacity of the GFRP longitudinal bars.

#### 4.4 Parametric Studies Using Present Model

The confinement and buckling models of the present study were used to perform an analysis for four different scenarios: Parametric Studies 1 through 4. Parametric Studies 1, 3, and 4 evaluated a column with a spiral confinement of 12 in. diameter, and Parametric Study 2 evaluated a large-scale column with a spiral confinement of 24 in. diameter.

##### 4.4.1 Parametric Study 1 – GFRP, CFRP, or Steel Spiral

The present model was used to perform analytical studies on several variations of the columns of the present study to provide comparisons and additional insight on the behavior of FRP (GFRP and CFRP) spiral-confined concrete columns. The parameters of the analyses performed were as follows:

1.  $f'_{co} = 6,000$  psi
2.  $f_y = 60,000$  psi
3. Load eccentricity = 3.66 in.
4. Column diameter = 12 in. confined diameter
5. Column height = 12 ft, 11 in.
6. Modulus of elasticity for GFRP bars = 6,280,000 psi
7. Modulus of elasticity for CFRP bars = 20,000,000 psi
8. Modulus of elasticity for steel bars = 29,000,000 psi
9. Spiral confinement
  - a. #4 spiral at 2 in. o.c. pitch utilizing the following material types:
    - i. GFRP

- ii. CFRP
  - iii. Steel
- b. Use  $d_s = 12$  in. center-to-center diameter of confinement
- i. Ignore concrete cover
  - ii. This provides an effective column diameter of 12 in. to match the column diameter in the present study.
10. Spiral radial strain at failure,  $\varepsilon_u = 0.002$  in./in.
- a. This provides for a uniform comparison between the three materials and allows the steel spiral to reach yield strength where  $f_{sp} = f_y = 60,000$  psi.
  - b. Further experimental research is required to determine if this strain can be achieved for FRP-spirals.
    - i. The present study using high-strength concrete found typical radial strains of GFRP-spirals to reach 0.001 in./in. or less at failure.
    - ii. Pantelides et al. (2013a) using normal-strength concrete found radial strains of GFRP-spirals to reach 0.006 in./in. at failure.
    - iii. Mohamed et al. (2014), Afifi et al. (2013a, 2013b) using normal-strength concrete found radial strains of GFRP and CFRP to typically achieve not more than 0.0005 in./in. at failure.
11. Longitudinal reinforcement – use the same three configurations (DB, SS, and SG) used for columns in the present study in the same location as if confined by an 8.5 in. diameter spiral
- a. DB – six #5 GFRP bars and six #4 steel bars
  - b. SS – six #4 steel bars

c. SG – six #5 GFRP bars

12. Concrete confinement model – use confinement model outlined in Chapter 3

assuming the Popovics stress-strain curve with hardening behavior ( $\varepsilon'_{co} = 0.002$  in./in. was assumed).

- a. Yan and Pantelides (2006) found that well-confined circular columns of lower strength concrete exhibit hardening behavior.
- b. Moran and Pantelides (2012) derived an equation to predict hardening behavior for a given level of FRP confinement for which the parameters outlined herein satisfy the expected condition of hardening behavior.

The parameters outlined above resulted in a total of nine model runs: three different types of spiral confinement for three different types of longitudinal reinforcement.

A confinement model analysis was performed according to Chapter 3, which resulted in the following conditions being used in the buckling model analysis for the proposed parametric study:

1. #4 GFRP-spiral confinement at 2 in. pitch

- a.  $f'_{cc} = 1.17 \cdot f'_{co} = 7,020$  psi, obtained from either Eq. (3.26) or Eq. (3.30) of the present model
- b.  $\varepsilon'_{co} = 0.004$  in./in., obtained from Eq. (3.35)

2. #4 CFRP-spiral confinement at 2 in. pitch

- a.  $f'_{cc} = 1.50 \cdot f'_{co} = 9,000$  psi, obtained from either Eq. (3.26) or Eq. (3.30) of the present model
- b.  $\varepsilon'_{co} = 0.008$  in./in., obtained from Eq. (3.35)

3. #4 steel spiral confinement at 2 in. pitch

- a.  $f'_{cc} = 1.82 \cdot f'_{co} = 10,920$  psi, obtained from Eq. (3.20), the equation for steel spiral confinement suggested by Mander et al.(1988)
- b.  $\epsilon'_{cc} = 0.012$  in./in., obtained from Eq. (3.35)

The stress-strain curves obtained from these calculations and used for this study (in addition to those used to model the columns tested in the present study) are presented in Figure 4.36. Results of the parametric study buckling model analysis are presented in Figures 4.37 through 4.42 with the load-deflection curves shown and compared to the analytical load-deflection curves of the columns tested in the present study.

Figure 4.37 shows the curves for the DB type columns. As shown in this figure, there is a modest increase in axial load capacity of approximately 5% with each increased level of confinement (5% increase from GFRP to CFRP and 10% increase from GFRP to steel), but there is a more significant increase in the column's ductility as the lateral deflection capacity increased over 100% from the GFRP-spiral to the CFRP-spiral and nearly 200% from the GFRP-spiral to the steel-spiral.

Figure 4.38 shows the curves for the SS type columns. Similar to the DB columns, there is a modest increase in axial load capacity of approximately 5% with each increased level of confinement (5% increase from GFRP to CFRP and 10% increase from GFRP to steel). Likewise there is a more significant increase in the column's ductility (although not as large of an increase as the DB columns) as the lateral deflection capacity increased over 24% from the GFRP-spiral to the CFRP-spiral and approximately 80% from the GFRP-spiral to the steel-spiral.

Figure 4.39 shows the curves for the SG type columns. Again there is a modest increase in axial load capacity of approximately 5% with each increased level of

confinement (5% increase from GFRP to CFRP and 10% increase from GFRP to steel) but similar to the DB columns, there is a more significant increase in the column's ductility as the lateral deflection capacity increased over 100% from the GFRP-spiral to the CFRP- and steel-spiral. As can be seen, there was not any significant gain in deflection capacity due to the increase in concrete strength when going from the CFRP-spiral to the steel-spiral. This is because the concrete strength is not controlling the moment-curvature capacity of the column at this point but is rather being controlled by the column geometry and the all-GFRP longitudinal bars. On the other hand, as shown in Figure 4.37, the DB column with steel-spirals is able to achieve additional deflection due to the additional moment-curvature capacity of the column resulting from the additional steel longitudinal bars located inside the interior spiral.

Figure 4.40 compares the DB, SS, and SG reinforced columns all reinforced with the GFRP-spiral confinement, Figure 4.41 compares these columns with the CFRP-spiral confinement, and Figure 4.42 compares them with the steel spiral confinement. As can be seen, the columns that have GFRP longitudinal reinforcement (DB and SG) are able to achieve greater lateral deflections due to the improved tensile capacity of GFRP over steel. Also, as previously described, these columns are able to better maintain their load once the lateral deflection extends beyond the deflection obtained at the maximum load. The columns that have steel longitudinal reinforcement (DB and SS) are able to achieve greater axial loads because of their improved compression capacity. The DB columns reinforced with both steel and GFRP longitudinal bars are able to capture the benefits of both with overall improved performance in both axial load and lateral deflection capacity. Also in general, it can be seen that with increased levels of confinement the

columns are able to gain modest increases in axial load capacity but gain more significant increases in ductility as measured by increased deflection capacity.

#### 4.4.2 Parametric Study 2 – Large-Scale Column

The present model was used to perform another analytical study for a large-scale column to provide additional comparisons and insight on the behavior of FRP (GFRP and CFRP) spiral-confined concrete columns. The parameters of the analyses performed were as follows:

1.  $f'_{co} = 6,000$  psi
2.  $f_y = 60,000$  psi
3. Load eccentricity = 3.66 in. and 7.32 in.
  - a. This will provide for a comparison with the 3.66 in. eccentricity used for the previous parametric study as well as for an eccentricity twice as large due to the column being twice the diameter.
4. Column diameter = 24 in. confined diameter
5. Column height = 24 ft
  - a. This will provide for a slenderness ratio approximately equal to 48, which is similar to that of the previous parametric study.
6. Modulus of elasticity for GFRP bars = 6,280,000 psi
7. Modulus of elasticity for CFRP bars = 20,000,000 psi
8. Modulus of elasticity for steel bars = 29,000,000 psi
9. Spiral confinement
  - a. #4 spiral at 4 in. o.c. pitch utilizing the following material types:

- i. GFRP
    - ii. CFRP
    - iii. Steel
  - b. Use  $d_s = 24$  in. center-to-center diameter of confining spiral
    - i. Ignore concrete cover
10. Spiral radial strain at failure,  $\varepsilon_u = 0.002$  in./in.
- a. This provides for a uniform comparison between the three materials and allows the steel spiral to reach yield strength where  $f_{sp} = f_y = 60,000$  psi.
  - b. Further experimental research is required to determine if this strain can be achieved for FRP-spirals.
11. Longitudinal reinforcement – eight #8 steel bars equally spaced around inside of spiral ( $\rho \approx 1.4\%$ )
12. Concrete confinement model – use confinement model outlined in Chapter 3 assuming the Popovics stress-strain curve with hardening behavior ( $\varepsilon'_{co} = 0.002$  in./in. was assumed)

The parameters outlined above resulted in a total of six model runs: three different types of spiral confinement for two different eccentricities.

A confinement model analysis was performed according to Chapter 3, which resulted in the following conditions being used in the buckling model analysis for the proposed parametric study as follows:

- 1. #4 GFRP-spiral confinement at 4 in. pitch
  - a.  $f'_{cc} = 1.04 \cdot f'_{co} = 6,200$  psi, obtained from either Eq. (3.26) or Eq. (3.30) of the present model

- b.  $\varepsilon'_{cc} = 0.0025$  in./in., obtained from Eq. (3.35)
2. #4 CFRP-spiral confinement at 4 in. pitch
- a.  $f'_{cc} = 1.14 \cdot f'_{co} = 6,800$  psi, obtained from either Eq. (3.26) or Eq. (3.30) of the present model
  - b.  $\varepsilon'_{cc} = 0.0037$  in./in., obtained from Eq. (3.35)
3. #4 steel spiral confinement at 4 in. pitch
- a.  $f'_{cc} = 1.25 \cdot f'_{co} = 7,500$  psi, obtained from Eq. (3.20), the equation for steel spiral confinement suggested by Mander et al. (1988)
  - b.  $\varepsilon'_{cc} = 0.005$  in./in., obtained from Eq. (3.35)

The stress-strain curves obtained from these calculations and used for this study (in addition to those used to model the columns tested in the present study) are presented in Figure 4.43. Results of the parametric study buckling model analysis are presented in Figure 4.44. As can be seen there is less differentiation with the axial load path between the different levels of confinement as was seen in the previous parametric study. This is due to the smaller differentiation of the stress in the stress-strain curves (Figure 4.43). The greatest differentiation is seen in the lateral deflection with each increased level of confinement.

For the case of 3.66 in. eccentricity, there was approximately a 4% increase in axial load capacity with each increased level of confinement (4% increase from GFRP to CFRP and 8% increase from GFRP to steel), which was similar to the previous parametric study. Also, similar to that seen in the previous parametric study, there was a much greater increase in the column's ductility as the lateral deflection capacity increased over 50% with each increased level of confinement (50% increase from GFRP to CFRP

and 100% increase from GFRP to steel).

For the case of 7.32 in. eccentricity, there was an increase of axial load capacity of approximately 6% increase from the GFRP-spiral to the CFRP-spiral and a much smaller additional increase of less than 2% from the CFRP-spiral to the steel spiral. Again there was a much more significant increase in the column's ductility as the lateral deflection increased approximately 55% from the GFRP-spiral to the CFRP-spiral with an additional increase of about 40% from the CFRP-spiral to the steel spiral. As shown in both Parametric Study 1 and 2, the more confinement a column has, the greater it can deflect, which ultimately leads to a greater ability to resist buckling.

In general it can be seen that GFRP- and CFRP-spirals have a lower capacity for confinement as compared with steel due to their lower modulus of elasticity. For this particular parametric study it was of interest to determine what spiral pitch would be required for both the GFRP- and CFRP-spirals to produce the same confinement capacity of the #4 steel spiral at a 4 in. pitch as used in this example. This was determined by using Eq. (3.20) from Mander et al. (1988) for calculating the confinement capacity of a #4 steel spiral at a 4 in. pitch and using either Eq. (3.26) or Eq. (3.30) in the present study (since both equations are very close to the same at lower confinement levels) for calculating the confinement capacity of a #4 GFRP- or #4 CFRP-spiral. It was found that a #4 GFRP-spiral would need to be placed at a pitch of 0.75 in., and a #4 CFRP-spiral would need to be placed at a pitch of 2.25 in. This comparison is shown in Table 4.7. The GFRP-spiral could not be reasonably constructed at this close of a spacing but could be potentially placed in a double hoop configuration similar to that used in the DB columns of the present study at a pitch of 1.5 in. On the other hand, the CFRP-spiral at a

pitch of 2.25 in. seems to be a very reasonable noncorrosive alternative to the steel spiral at a pitch of 4 in.

#### 4.4.3 Parametric Study 3 – Longitudinal Reinforcement

The present model was used to perform another analytical study to provide additional comparisons and insight on the influence of the longitudinal reinforcement (GFRP vs. steel) on the behavior of GFRP spiral-confined concrete columns. The parameters of the analyses performed were as follows:

1.  $f'_{co} = 6,000$  psi
2.  $f_y = 60,000$  psi
3. Load eccentricity = 3.66 in.
4. Column diameter = 12 in. confined diameter
5. Column height = 12 ft 11 in.
6. Modulus of elasticity for GFRP bars = 6,280,000 psi
7. Modulus of elasticity for steel bars = 29,000,000 psi
8. Spiral confinement
  - a. #4 GFRP spiral at 2 in. o.c. pitch
  - b. Use  $d_s = 12$  in. center-to-center diameter of confinement
    - i. Ignore concrete cover
    - ii. This provides an effective column diameter of 12 in. to match the column diameter in the present study.
9. Spiral radial strain at failure,  $\epsilon_u = 0.002$  in./in.
  - a. Further experimental research is required to determine if this strain can be

achieved for GFRP-spirals.

10. Longitudinal reinforcement – use the steel and GFRP configurations (SS and SG) used for columns in the present study in the same location as if confined by an 8.5 in. diameter spiral
  - a. SS – six #4 steel bars
  - b. SG – six #5 GFRP bars
  - c. SS x 2 – twelve #4 steel bars
  - d. SG x 2 – twelve #5 GFRP bars

11. Concrete confinement model – use confinement model outlined in Chapter 3 assuming the Popovics stress-strain curve with hardening behavior ( $\epsilon'_{co} = 0.002$  in./in. was assumed)

The parameters outlined above resulted in a total of four model runs: one type of spiral confinement for four different types of longitudinal reinforcement.

A confinement model analysis was performed according to Chapter 3, which resulted in the following conditions being used in the buckling model analysis for the proposed parametric study:

4. #4 GFRP-spiral confinement at 2 in. pitch
  - a.  $f'_{cc} = 1.17 \cdot f'_{co} = 7,020$  psi, obtained from either Eq. (3.26) or Eq. (3.30) of the present model
  - b.  $\epsilon'_{co} = 0.004$  in./in., obtained from Eq. (3.35)

The stress-strain curve obtained from these calculations and used for this study can also be viewed in Figure 4.36 from Parametric Study 1. Results of the parametric study buckling model analysis are presented in Figure 4.45.

For both types of columns (steel longitudinal and GFRP longitudinal), there was approximately a 32% increase in axial load when the longitudinal reinforcement was doubled. The column with double the GFRP longitudinal reinforcement ( $A_s = 3.72$  sq. in.) had an axial load that was still less (93%) than that achieved with the column without doubling the steel longitudinal reinforcement ( $A_s = 1.20$  sq. in.) even though it had approximately 3 times the area of longitudinal reinforcement. This validates the observation that GFRP longitudinal reinforcement has a lower compressive contribution to the overall axial load capacity of a column than steel longitudinal reinforcement.

#### 4.4.4 Parametric Study 4 – Compressive Concrete Strength

The present model was used to perform another analytical study to provide additional comparisons and insight on the influence of the concrete strength on the behavior of GFRP spiral-confined concrete columns. The parameters of the analyses performed were as follows:

1. Concrete strength

a.  $f'_{co} = 6,000$  psi

b.  $f'_{co} = 13,000$  psi

2.  $f_y = 60,000$  psi

3. Load eccentricity = 3.66 in.

4. Column diameter = 12 in. confined diameter

5. Column height = 12 ft 11 in.

6. Modulus of elasticity for GFRP bars = 6,280,000 psi

7. Modulus of elasticity for steel bars = 29,000,000 psi

8. Spiral confinement
  - a. #4 GFRP spiral at 2 in. o.c. pitch
  - b. Use  $d_s = 12$  in. center-to-center diameter of confinement
    - i. Ignore concrete cover
    - ii. This provides an effective column diameter of 12 in. to match the column diameter in the present study.
9. Spiral radial strain at failure,  $\varepsilon_u = 0.002$  in./in.
  - a. Further experimental research is required to determine if this strain can be achieved for GFRP-spirals.
10. Longitudinal reinforcement – use the steel and GFRP configurations (SS and SG) used for columns in the present study in the same location as if confined by an 8.5 in. diameter spiral
  - a. SS – six #4 steel bars
  - b. SG – six #5 GFRP bars
11. Concrete confinement model – use confinement model outlined in Chapter 3 assuming the Popovics stress-strain curve with hardening behavior ( $\varepsilon'_{co} = 0.002$  in./in. was assumed)

The parameters outlined above resulted in a total of four model runs: one type of spiral confinement for two different types of longitudinal reinforcement and two different types of concrete strength.

A confinement model analysis was performed according to Chapter 3, which resulted in the following conditions being used in the buckling model analysis for the proposed parametric study:

5. #4 GFRP-spiral confinement at 2 in. pitch

a.  $f'_{co} = 6,000$  psi

i.  $f'_{cc} = 1.17 \cdot f'_{co} = 7,020$  psi, obtained from either Eq. (3.26) or Eq.

(3.30) of the present model

ii.  $\varepsilon'_{cc} = 0.004$  in./in., obtained from Eq. (3.35)

b.  $f'_{co} = 13,000$  psi

i.  $f'_{cc} = 1.07 \cdot f'_{co} = 13,910$  psi, obtained from either Eq. (3.26) or Eq.

(3.30) of the present model

ii.  $\varepsilon'_{cc} = 0.003$  in./in., obtained from Eq. (3.35)

Results of the parametric study buckling model analysis are presented in Figure 4.46.

For both types of columns (steel longitudinal and GFRP longitudinal), there was approximately a 50% increase in axial load when the concrete strength was increased from 6,000 psi to 13,000 psi (117% increase in concrete strength). The column with GFRP longitudinal reinforcement and 13,000 psi concrete strength had an axial load that was approximately 6% greater than the column with steel longitudinal reinforcement and 6,000 psi concrete. This again validates the observation that steel longitudinal reinforcement has a greater compressive contribution to the overall axial load capacity of a column than GFRP longitudinal reinforcement.

Table 4.1: Summary of Cranston (1972) specimens used for comparison

Specimen	$f'_{cc}$ * (psi) [MPa]	$f_y$ (psi) [MPa]	$\rho_s$ %	d'/d	$e_1/e_2$	$e_2/d$	L/d
Cranston1	3,000 [20.7]	60,000 [414]	6	0.7	0	0.5	15
Cranston2						0.5	25
Cranston3						0.1	40
Cranston4						0.5	40

\*  $f'_{cc}$  is the maximum stress on the stress-strain curve

Table 4.2: Detail of properties used for Cranston specimens with present model

Specimen	d (in.)	L (ft)	$e_1$ (in.)	$e_2$ (in.)	b (in.)	$A_{nc}$ (in. <sup>2</sup> )	$A_s$ (in. <sup>2</sup> )
Cranston1	12	15	0	6	12	135.38	8.62
Cranston2		25		6			
Cranston3		40		1.2			
Cranston4		40		6			

Table 4.3: Summary of Kim and Yang (1995) specimens used for comparison

Specimen	$f'_c$ (psi) [MPa]	$f_y$ (psi) [MPa]	b (in.) [mm]	d (in.) [mm]	L (ft) [mm]	d'/d	$\rho_s$ %	e <sub>1</sub> (in.) [mm]	e <sub>2</sub> (in.) [mm]
KY60L2-1	3,700 [25.5]	56,130 [387]	3.15 [80]	3.15 [80]	4.724	0.625	1.98	0.945 [24]	0.945 [24]
KY60L2-2					[1440]				
KY100L2-1					7.874				
KY100L2-2					[2400]				

Table 4.4: Summary of Claeson and Gylltoft (1998) specimens used for comparison

Specimen	$f'_c$ (psi) [MPa]	$f_y$ (psi) [MPa]	b (in.) [mm]	d (in.) [mm]	L (ft) [mm]	d'/d	$\rho_s$ %	e <sub>1</sub> (in.) [mm]	e <sub>2</sub> (in.) [mm]
CG23	6,237	99,206 [684]	4.724 [120]	4.724 [120]	7.87	0.55	3.2	0.787 [20]	0.787 [20]
CG24	[43]				[2,400]				
CG27	4,786	92,244 [636]	7.874 [200]	7.874 [200]	9.84	0.69	2.1	0.787 [20]	0.787 [20]
CG28	[33]				[3,000]				
CG31	5,366				13.12				
CG32	[37]				[4,000]				

Table 4.5: Summary of properties of Fitzwilliam and Bisby (2006) specimens used for comparison

Specimen	$f'_{cc}$ * (psi) [MPa]	$f_y$ (psi) [MPa]	D (in.) [mm]	L (ft) [mm]	$\rho_s$ %	Concrete Cover (in.) [mm]	$e_2$ (in.) [mm]	$e_2$ (in.) [mm]
FB-1	5,150	103,000	6	3.9	0.71	1 [25]	0.787 [20]	0.787 [20]
FB-2	[35.5]	[710]	[152]	[1200]				

\*  $f'_{cc}$  is the maximum concrete stress on the stress-strain curve

– Todeschini et al. (1964) stress-strain curve assumed/used

Table 4.6: Summary of properties of Ranger and Bisby (2007) specimens used for comparison

Specimen	$f'_{cc}$ * (psi) [MPa]	$f_y$ (psi) [MPa]	D (in.) [mm]	L (ft) [mm]	$\rho_s$ %	Concrete Cover (in.) [mm]	$e_2$ (in.) [mm]	$e_2$ (in.) [mm]
RB-U5	4,000 [27.4]	103,000 [710]	6 [152]	1.97 [600]	0.71	1 [25]	0.197 [5]	0.197 [5]
RB-U10							0.394 [10]	0.394 [10]
RB-U20							0.787 [20]	0.787 [20]
RB-U30							1.181 [30]	1.181 [30]
RB-U40							1.575 [40]	1.575 [40]

\*  $f'_{cc}$  is the maximum concrete stress on the stress-strain curve

– Todeschini et al. (1964) stress-strain curve assumed/used

Table 4.7: Required spiral pitch to achieve equivalent confinement strength based on proposed models

Spiral Material	#4 Steel <sup>*</sup>	#4 CFRP <sup>**</sup>	#4 GFRP <sup>**</sup>
Pitch	4 in.	2.25 in.	0.75 in.

\* Eq. (3.20)

\*\* Eq. (3.26) or Eq. (3.30)

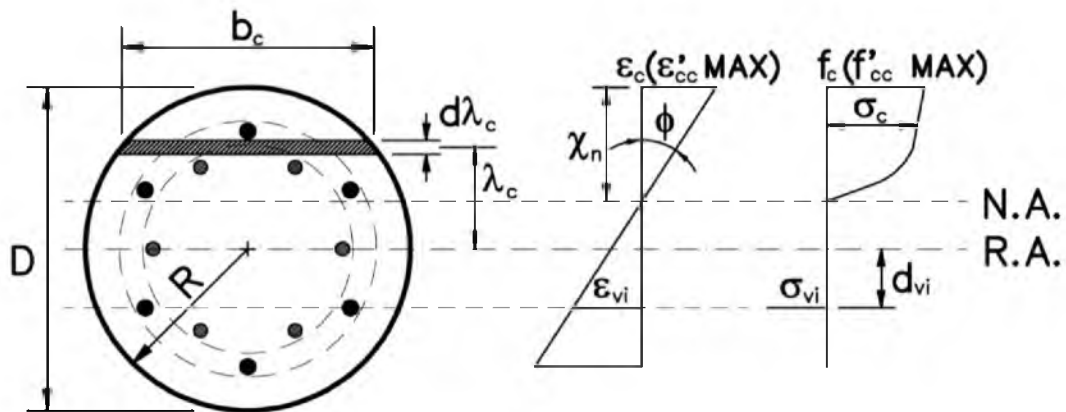


Figure 4.1: Strains and stresses over a circular reinforced concrete cross-section confined by one or more spirals

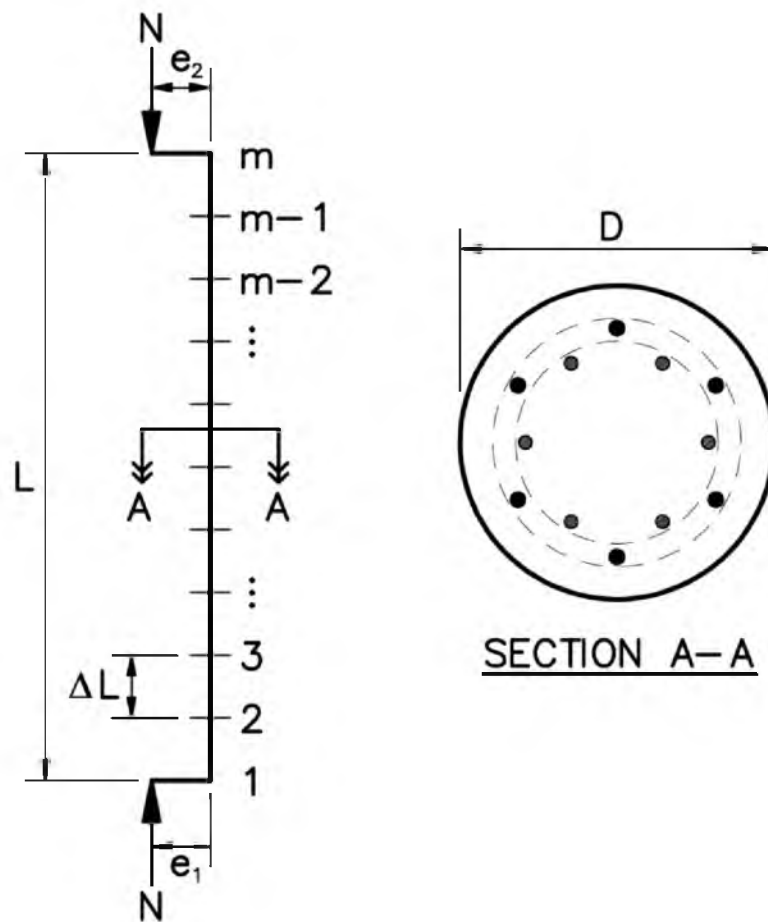


Figure 4.2: Schematic of the theoretical model

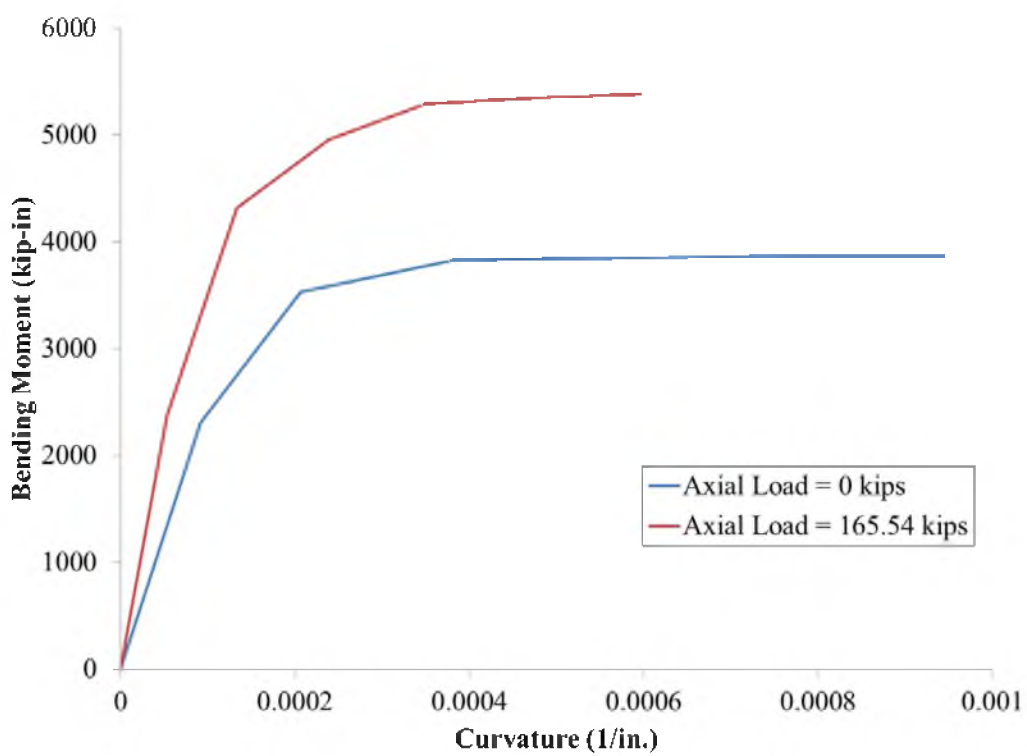


Figure 4.3: Moment-curvature curves for two axial loads of a sample column

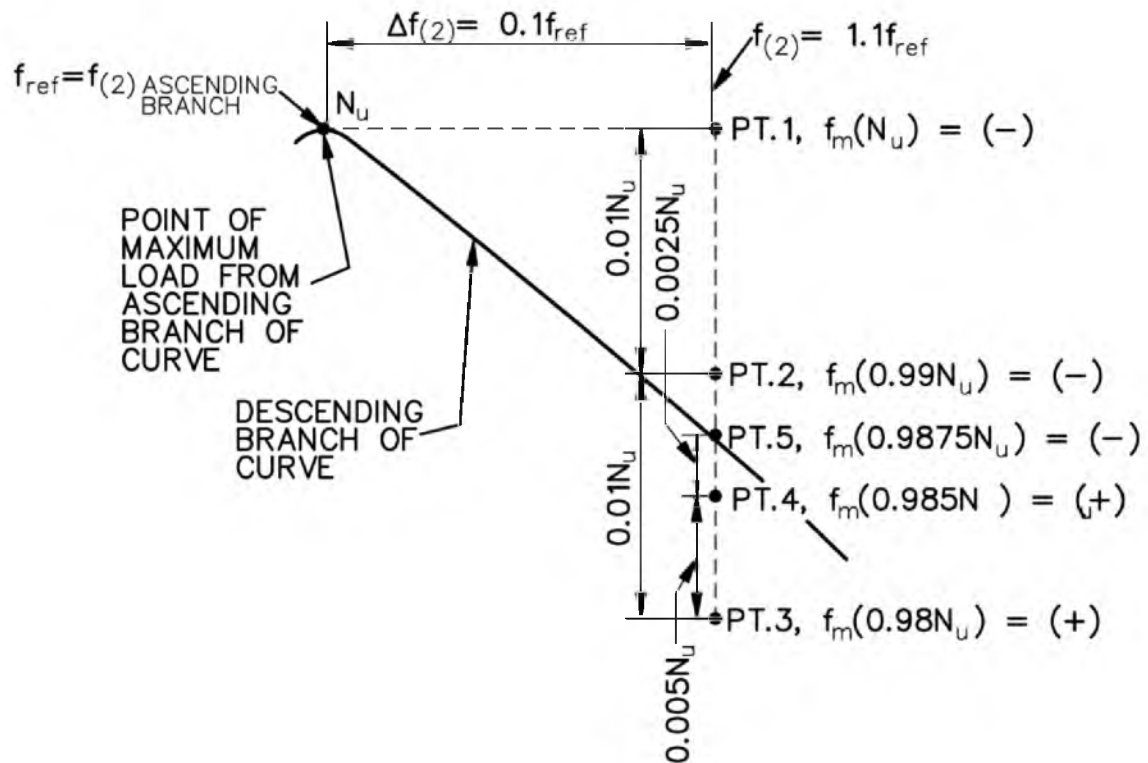


Figure 4.4: Example of bisection method for finding descending branch of load-deflection curve

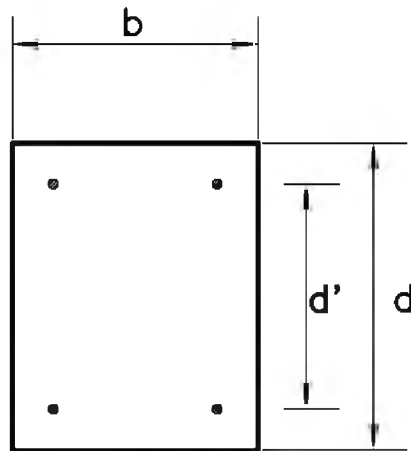


Figure 4.5: Cross-section of Cranston (and other rectangular) columns

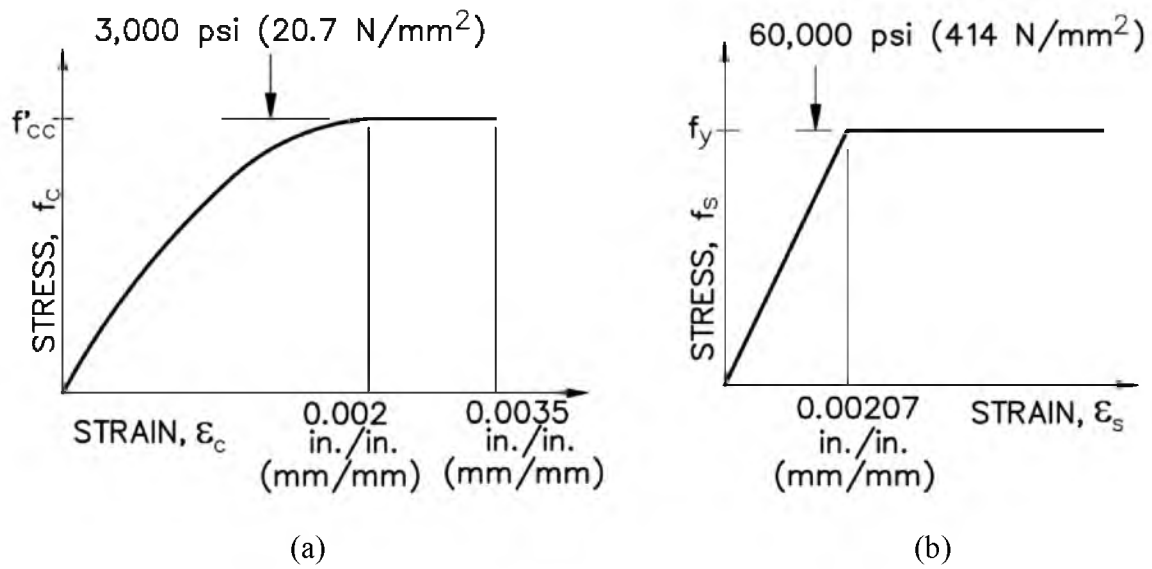


Figure 4.6: Stress-strain curves used for Cranston columns:  
(a) concrete; (b) steel reinforcement

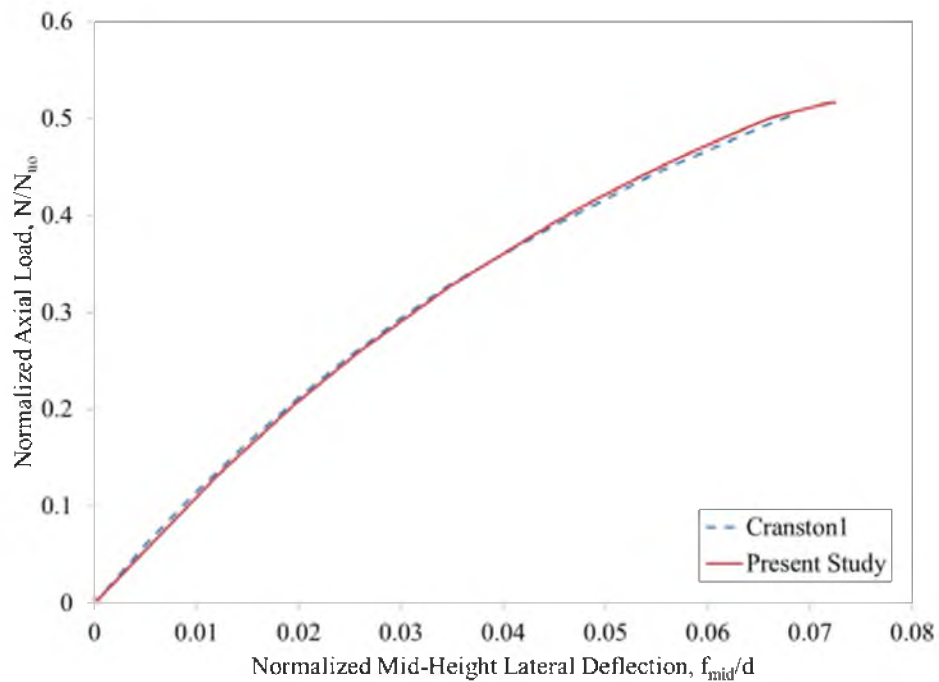


Figure 4.7: Comparison of present model with Cranston's analytical model (Cranston1)

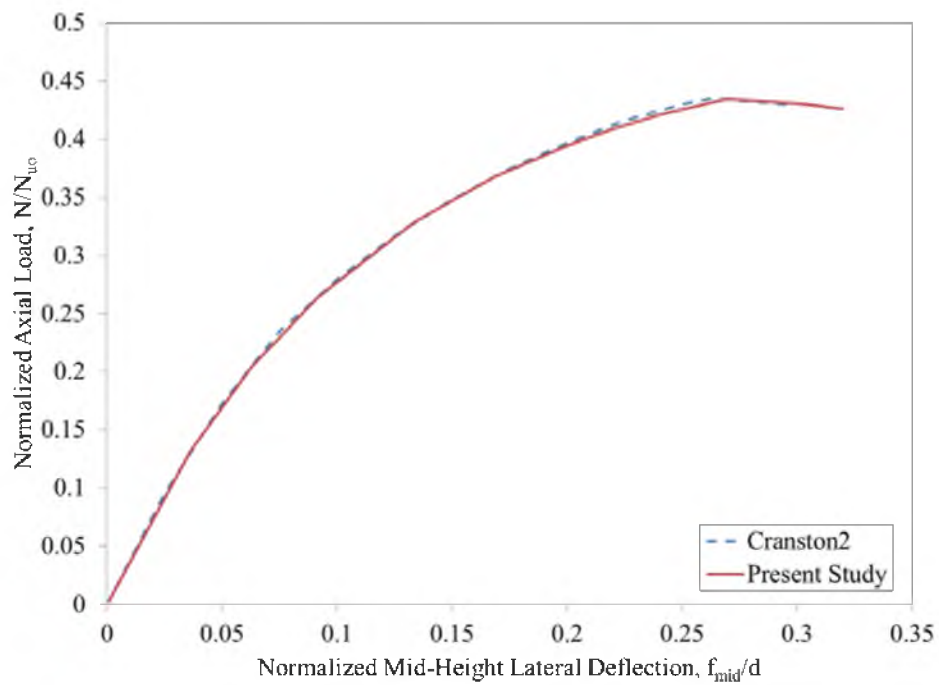


Figure 4.8: Comparison of present model with Cranston's analytical model (Cranston2)

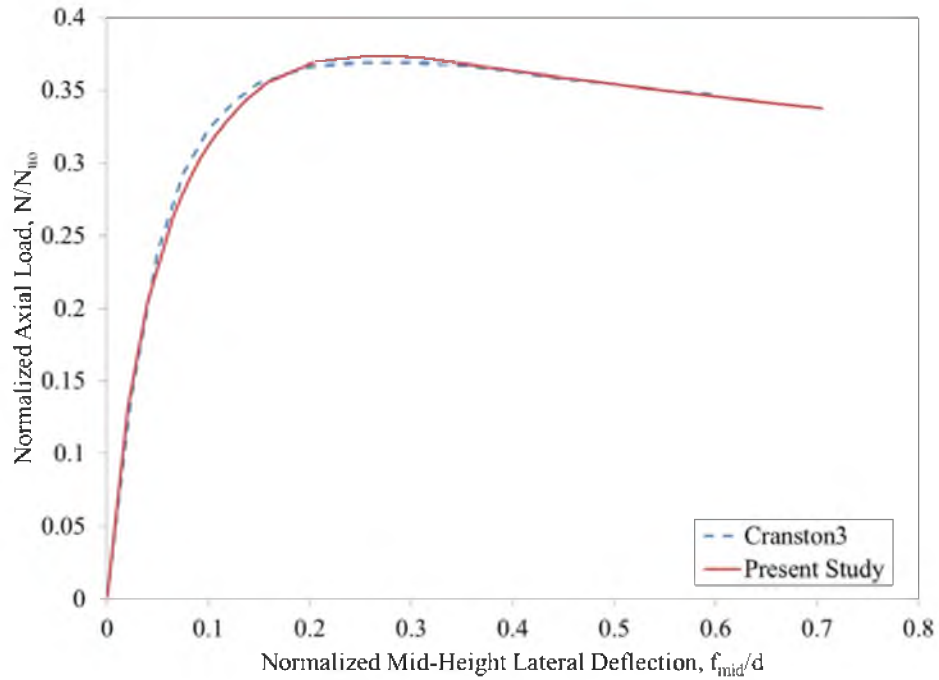


Figure 4.9: Comparison of present model with Cranston's analytical model (Cranston3)

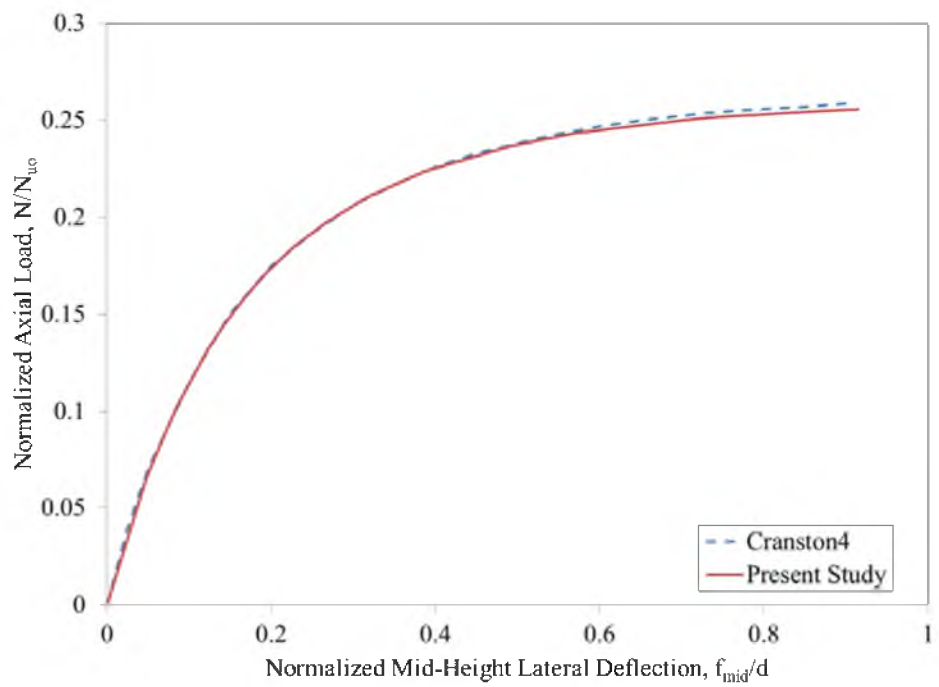


Figure 4.10: Comparison of present model with Cranston's analytical model (Cranston4)

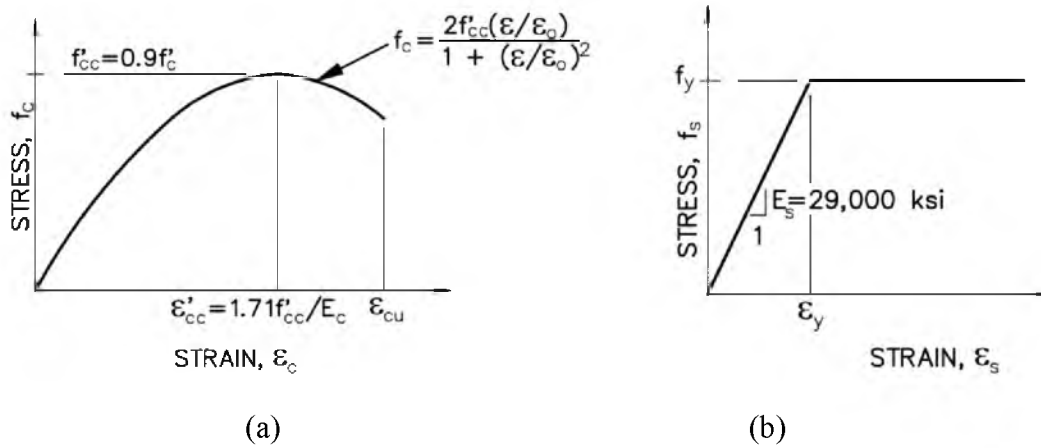


Figure 4.11: Stress-strain curves used for other column comparisons:  
 (a) concrete (Todeschini et al. 1964); (b) steel reinforcement (elastic-plastic)

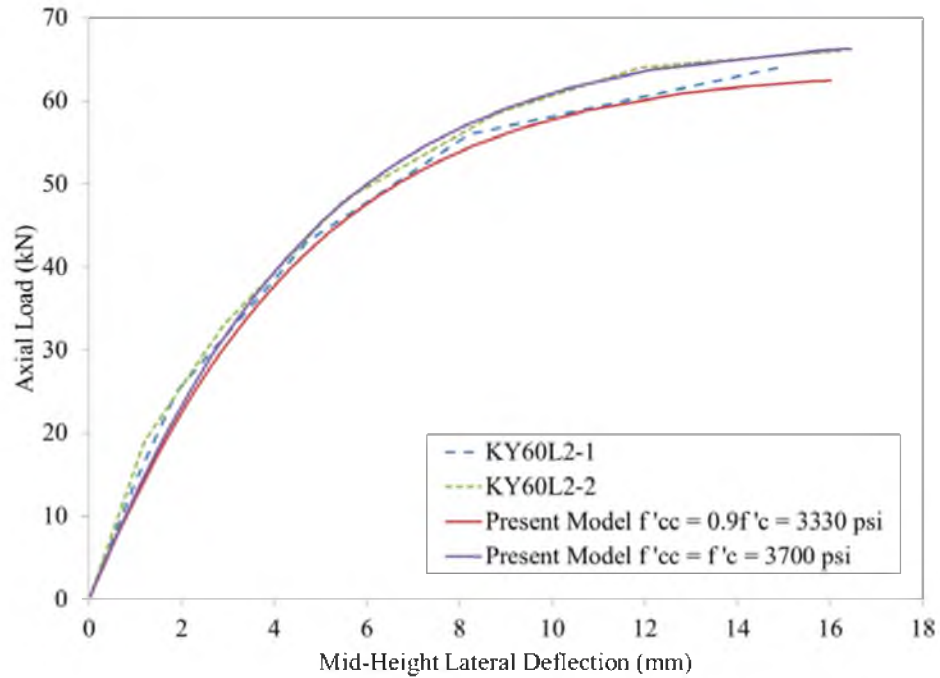


Figure 4.12: Comparison of present model with Kim and Yang's experimental tests (Columns KY60L2-1 and KY60L2-2)

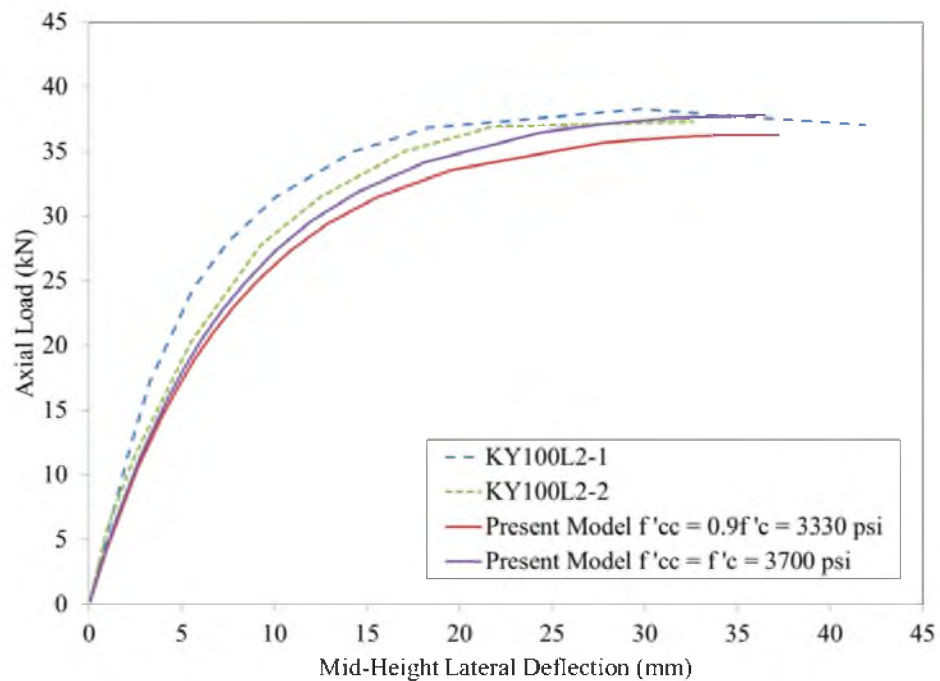


Figure 4.13: Comparison of present model with Kim and Yang's experimental tests (Columns KY100L2-1 and KY100L2-2)

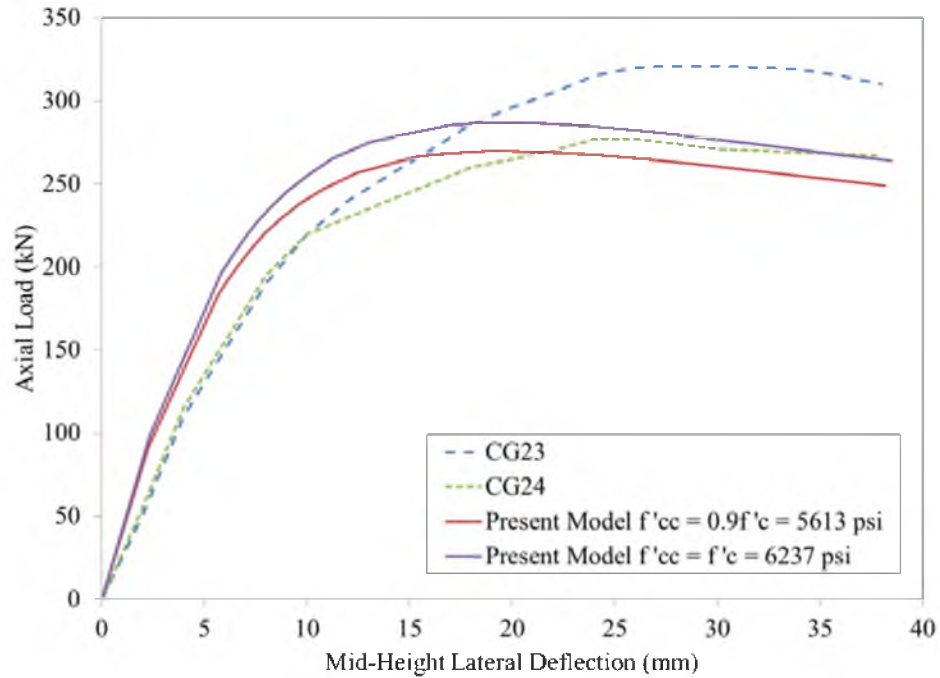


Figure 4.14: Comparison of present model with Claeson and Gylltoft's experimental tests (Columns CG23 and CG24)

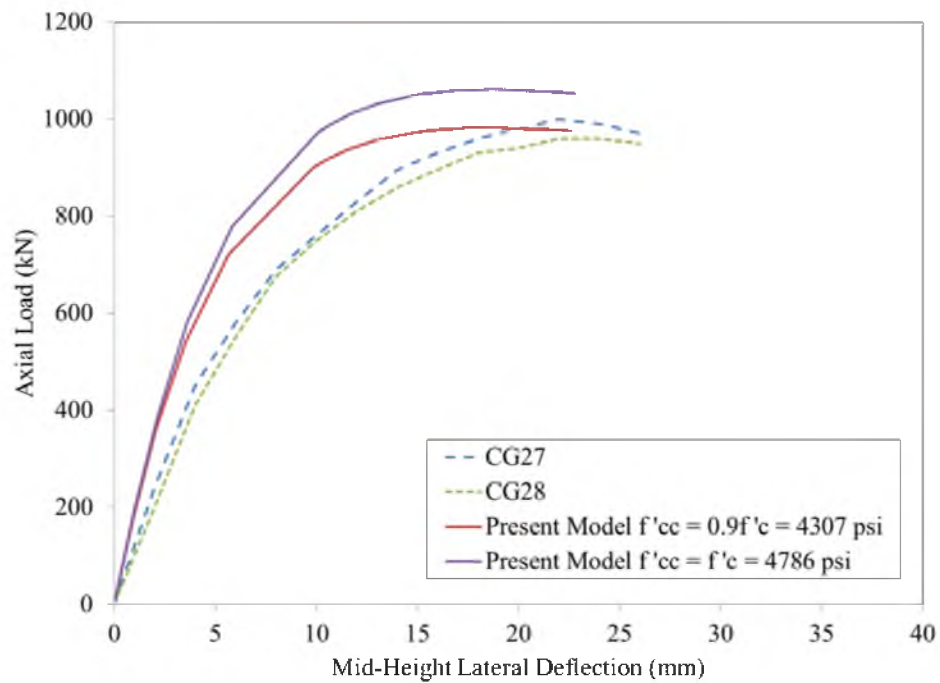


Figure 4.15: Comparison of present model with Claeson and Gylltoft's experimental tests (Columns CG27 and CG28)

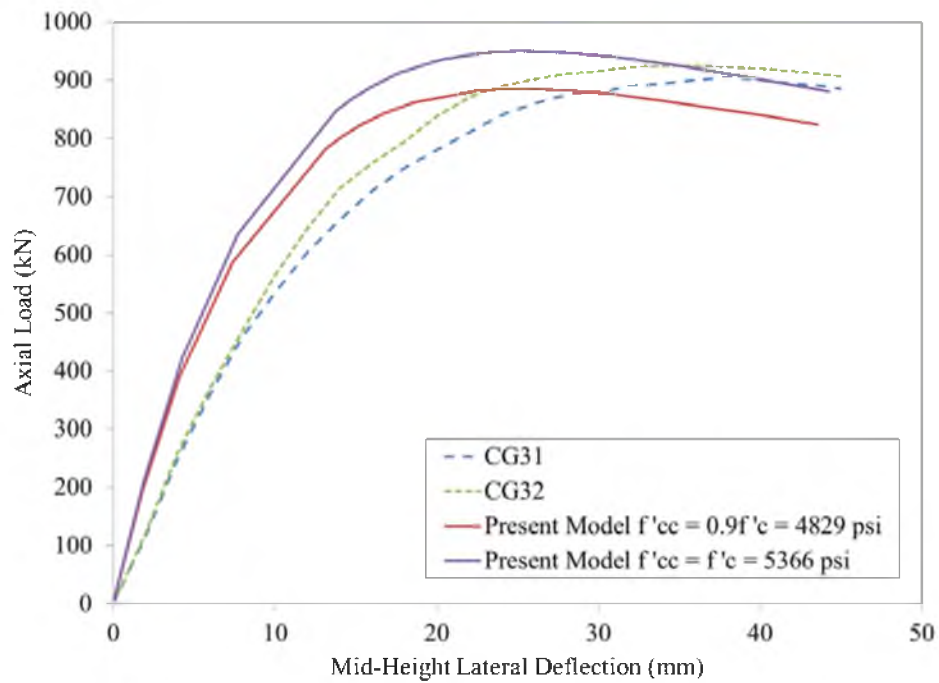


Figure 4.16: Comparison of present model with Claeson and Gylltoft's experimental tests (Columns CG31 and CG32)

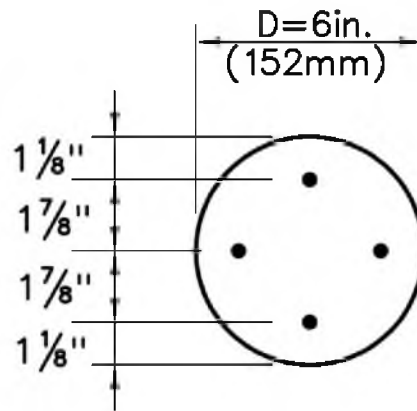


Figure 4.17: Cross-section of Fitzwilliam and Bisby (2006) and Ranger and Bisby (2007) columns

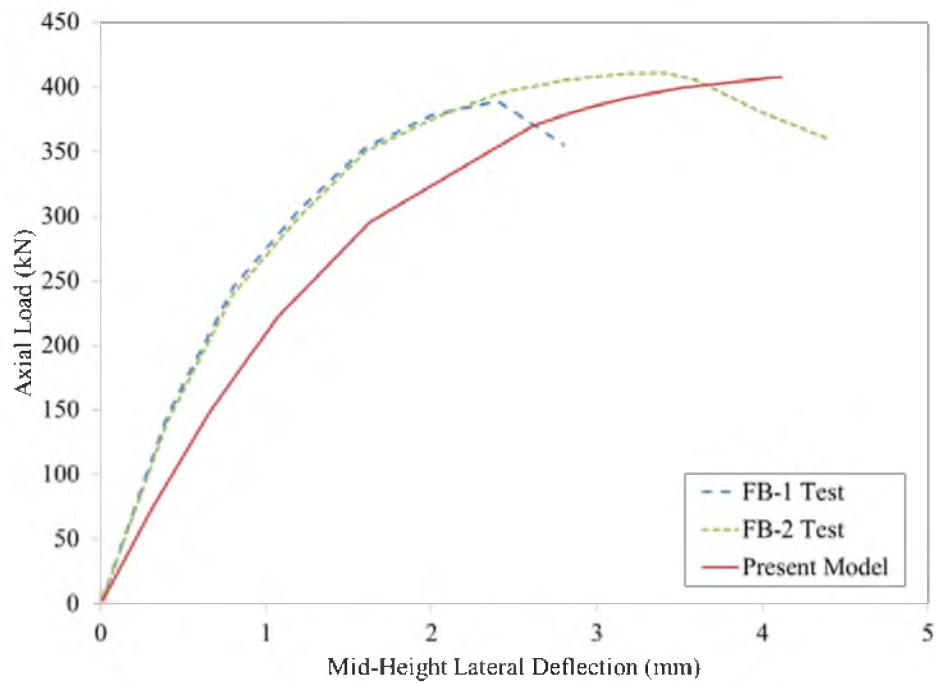
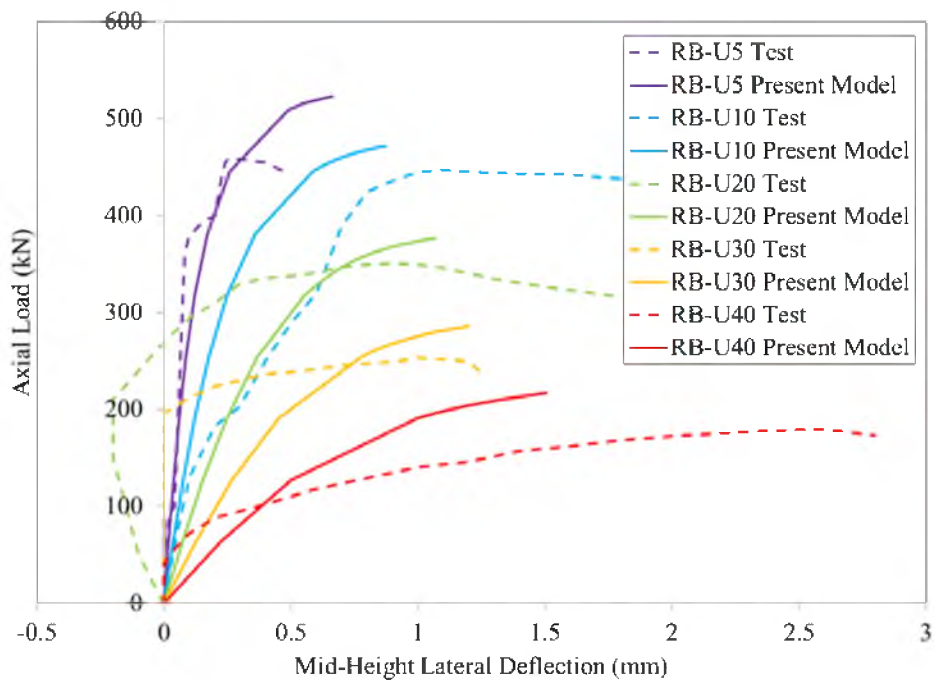
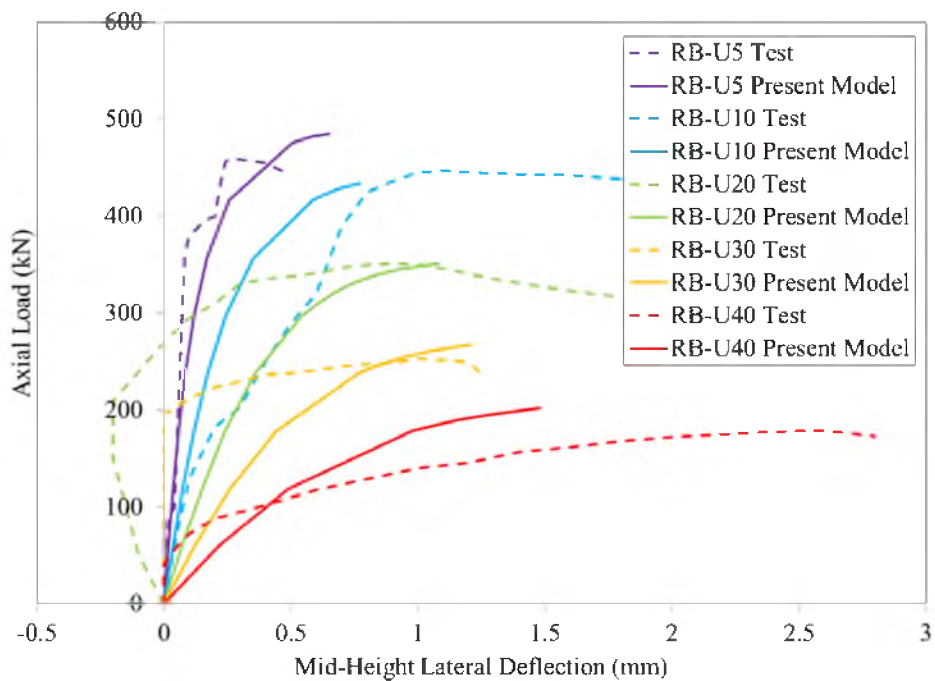


Figure 4.18: Comparison of present model with Fitzwilliam and Bisby's experimental tests (Columns FB1 and FB2)



(a)



(b)

Figure 4.19: Comparison of present model with Ranger and Bisby's experimental tests (Columns RB-U5, RB-U10, RB-U20, RB-U30, and RB-U40):  
 (a)  $f'_{cc} = 0.9f'_c = 4,334$  psi; (b)  $f'_{cc} = 0.85f'_c = 4,093$  psi

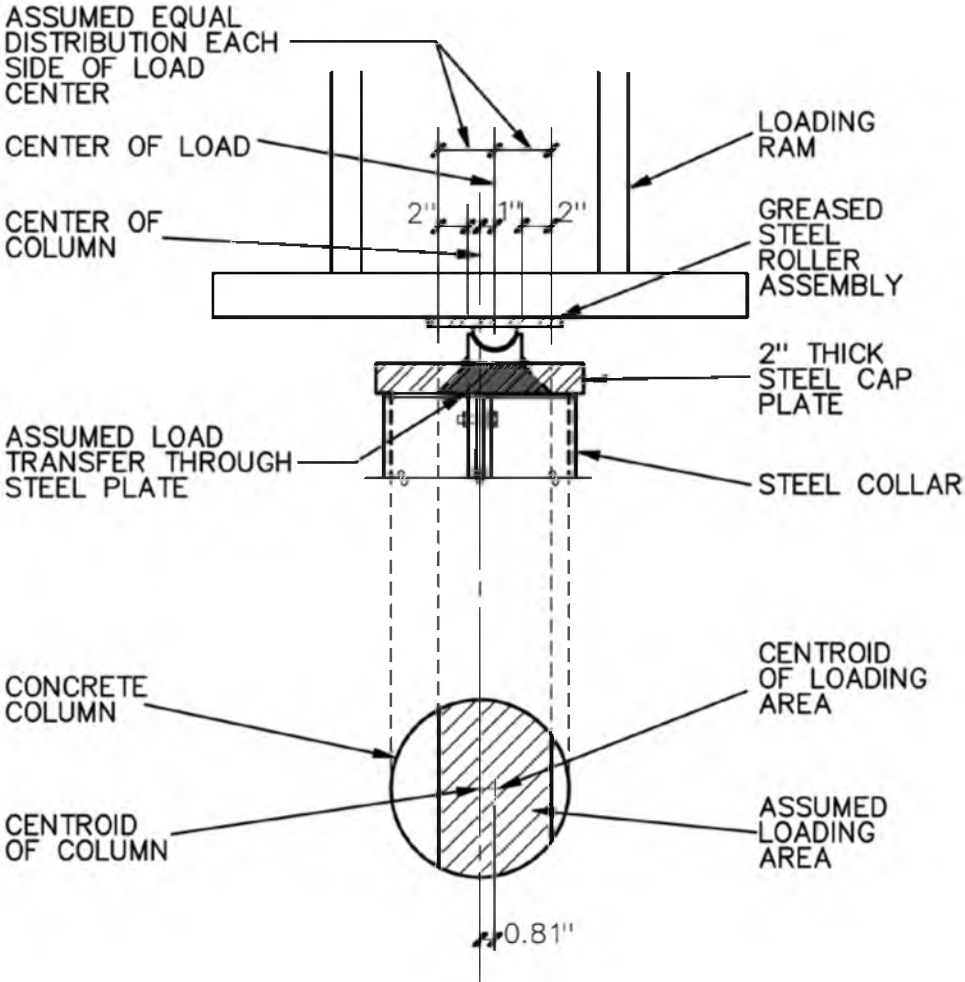


Figure 4.20: Assumed load transfer through steel plate to obtain effective eccentricity of 0.81 in. for columns #4T-DB1, #5T-SS1, and #6T-SG1

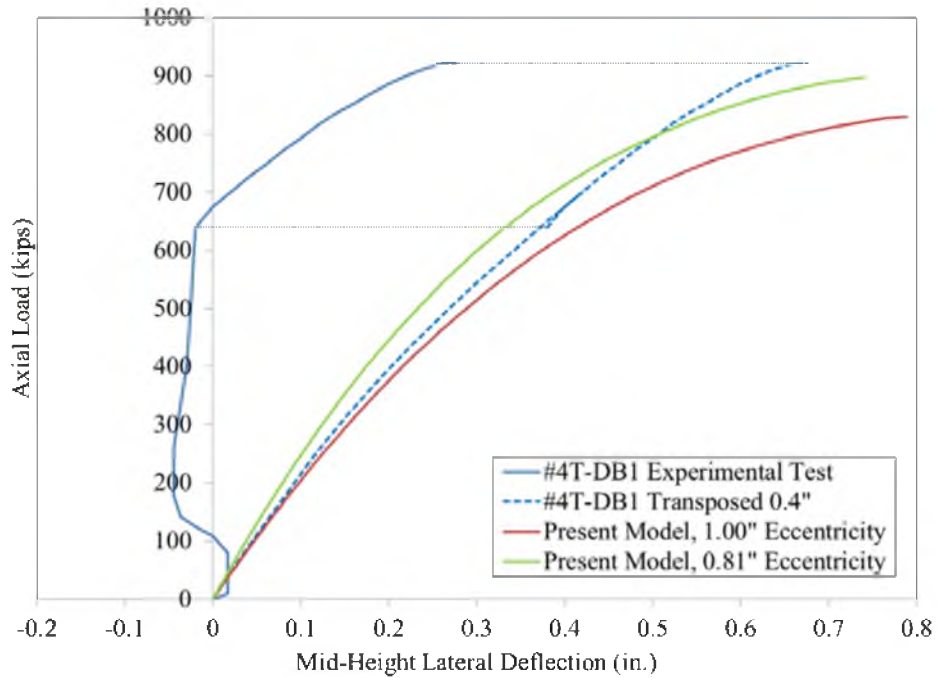


Figure 4.21: Comparison of present model with present experimental test #4T-DB1

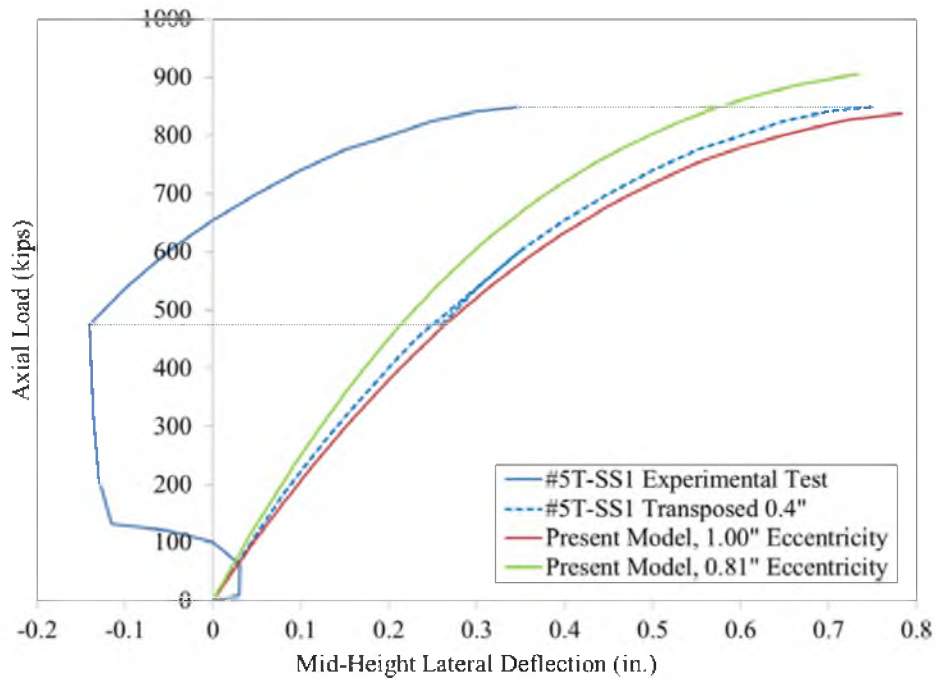


Figure 4.22: Comparison of present model with present experimental test #5T-SS1

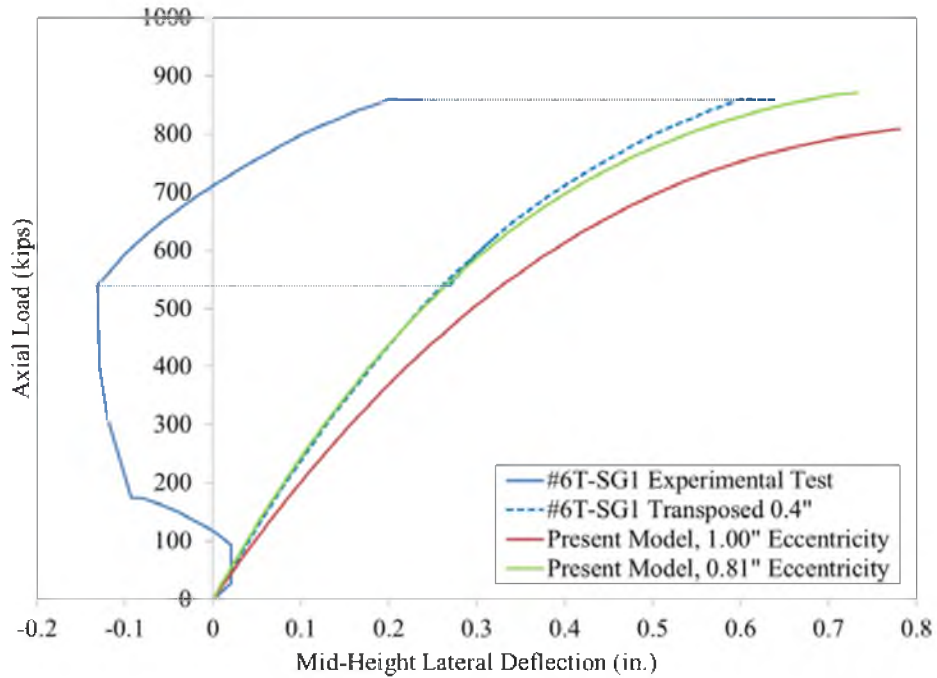


Figure 4.23: Comparison of present model with present experimental test #6T-SG1

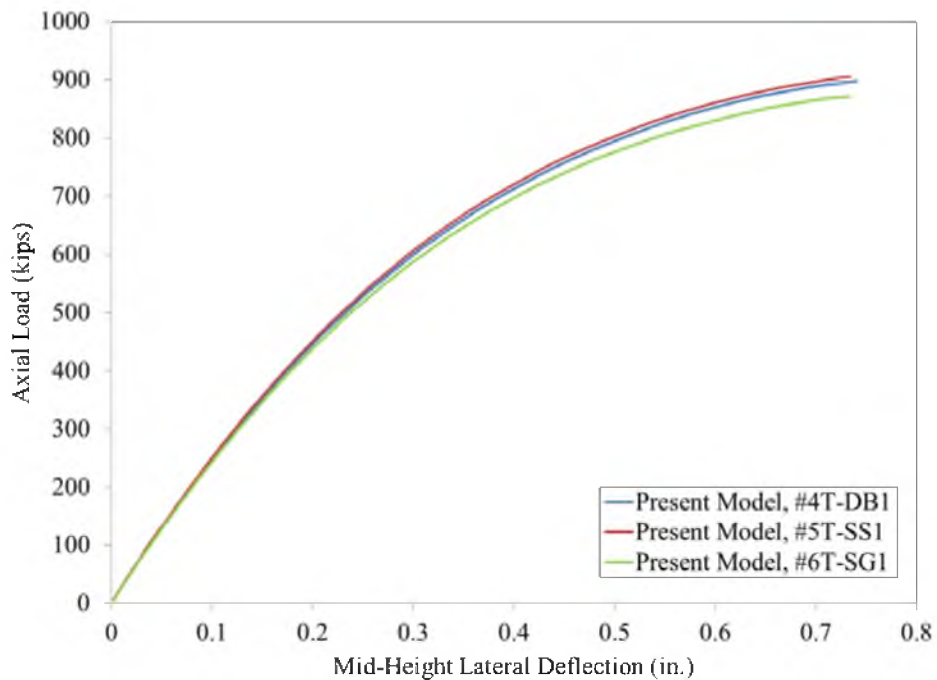


Figure 4.24: Comparison of modeled load-deflection curves for columns #4T-DB1, #5T-SS1, and #6T-SG1 using 0.81 in. eccentricity

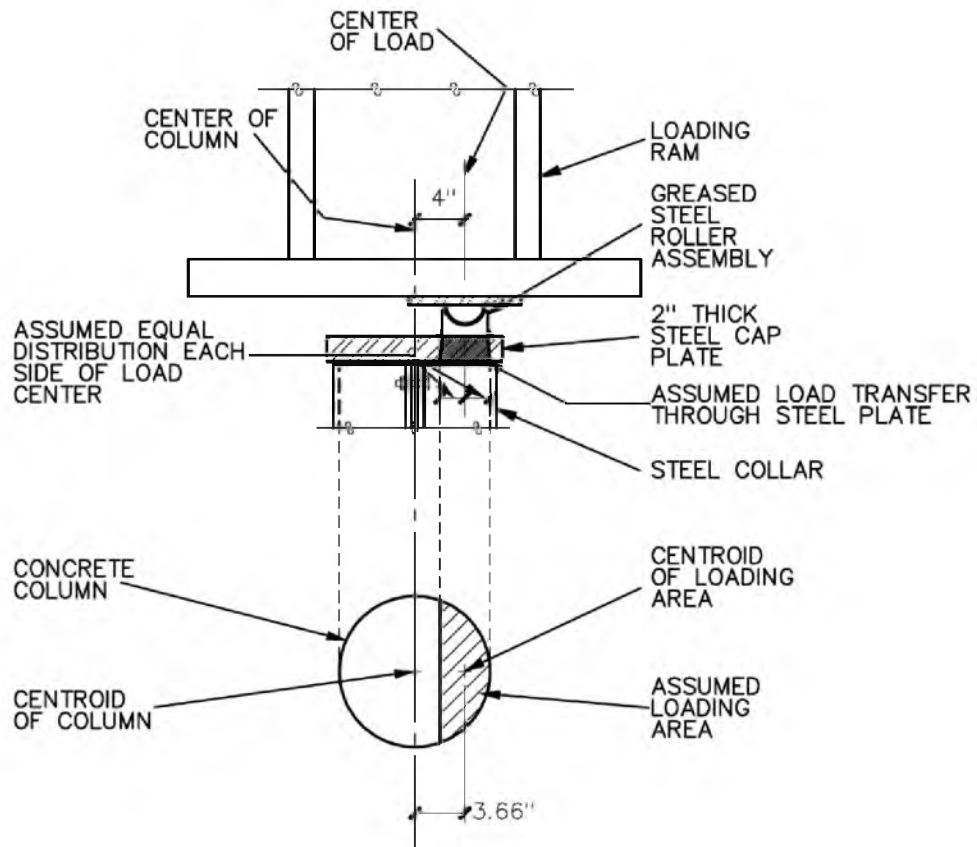


Figure 4.25: Assumed load transfer through steel plate to obtain effective eccentricity of 3.66 in. for columns #7T-DB4, #8T-SS4, and #9T-SG4

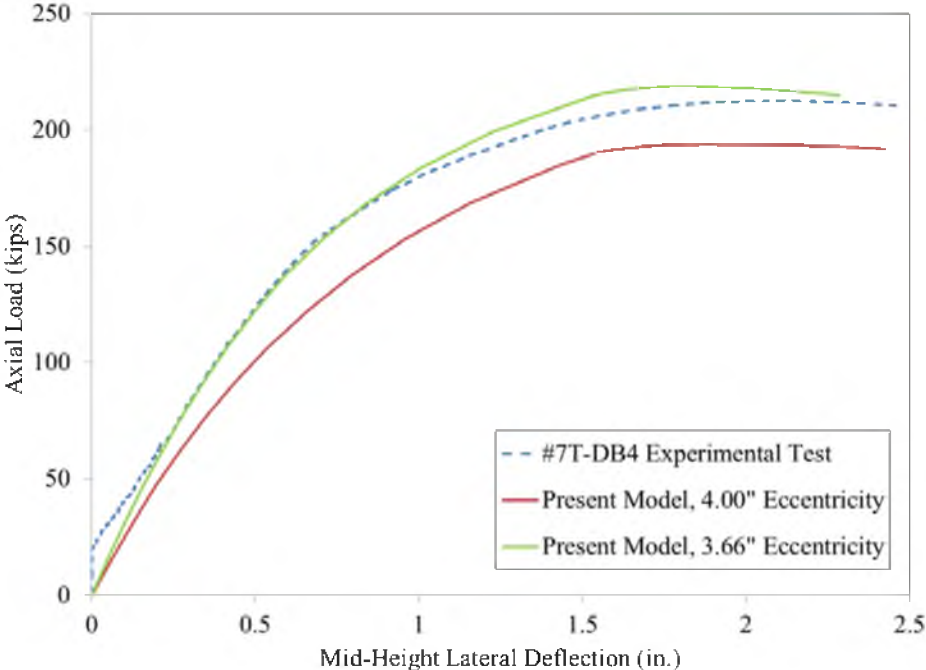


Figure 4.26: Comparison of present model with present experimental test #7T-DB4

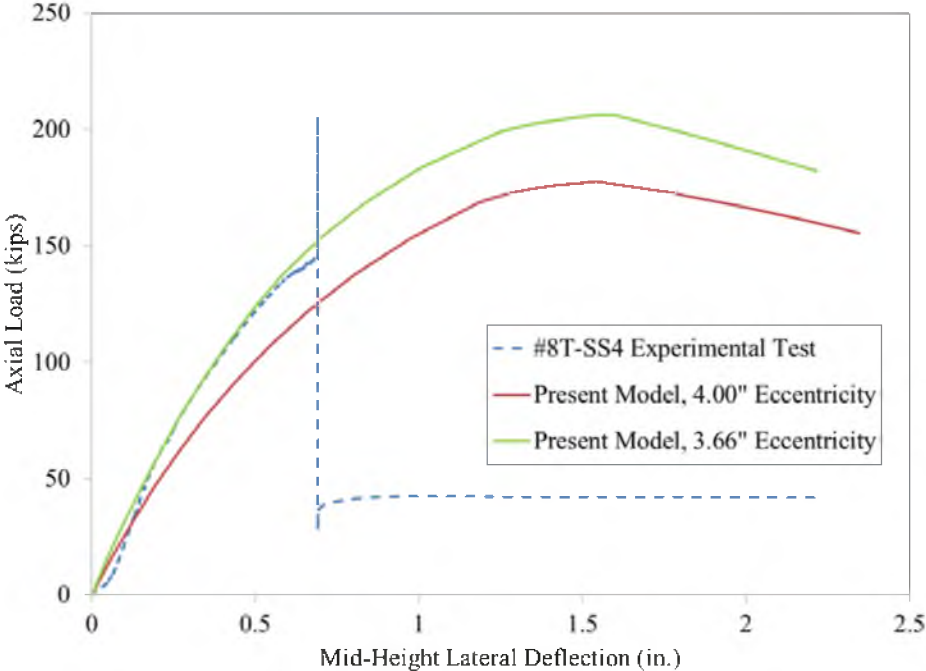


Figure 4.27: Comparison of present model with present experimental test #8T-SS4

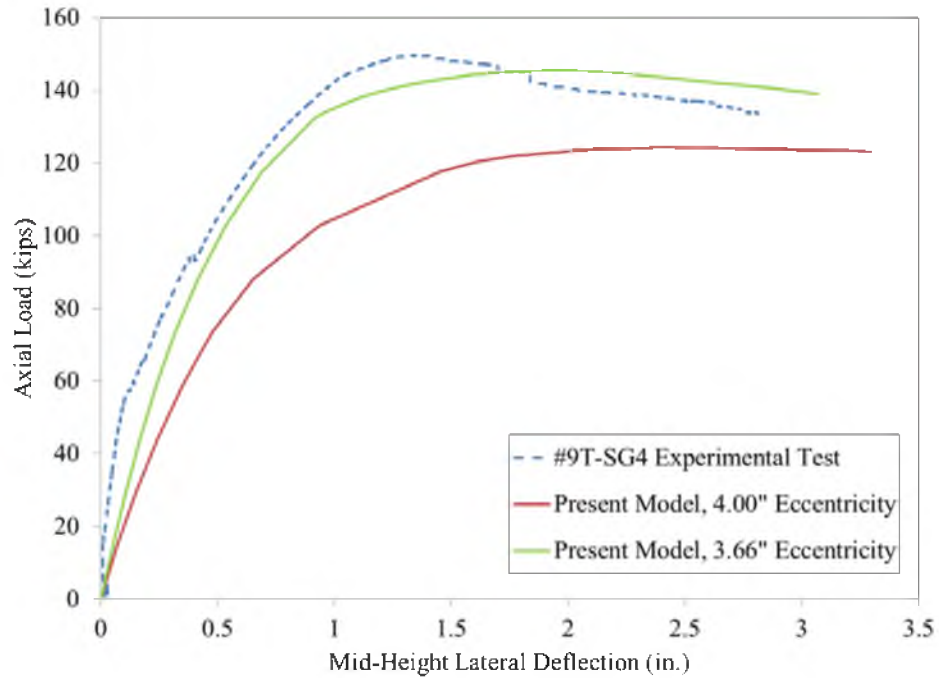


Figure 4.28: Comparison of present model with present experimental test #9T-SG4

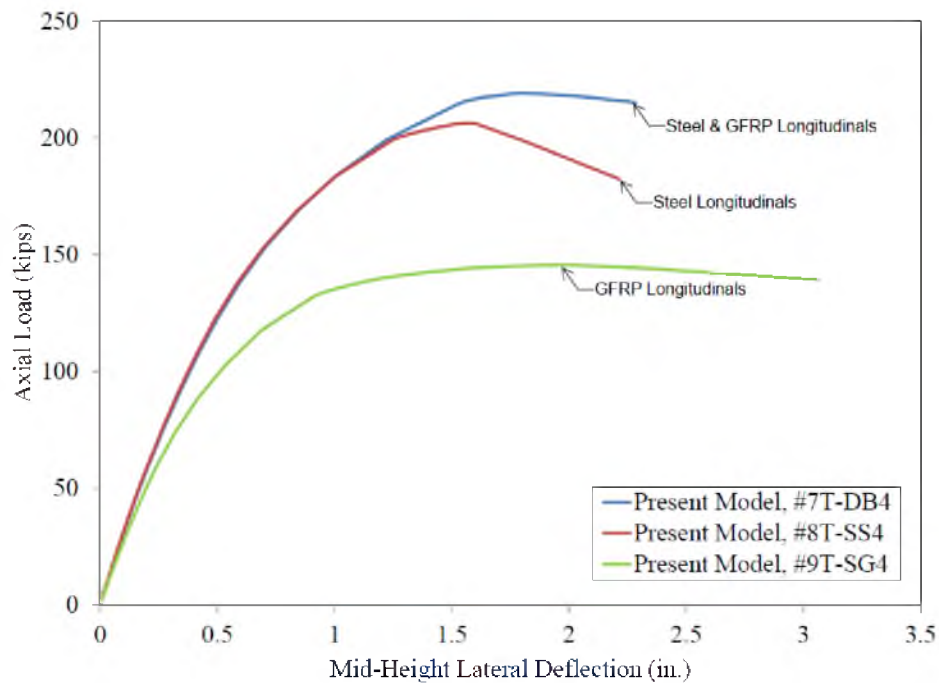


Figure 4.29: Comparison of modeled load-deflection curves for columns #7T-DB4, #8T-SS4, and #9T-SG4 using 3.66 in. eccentricity

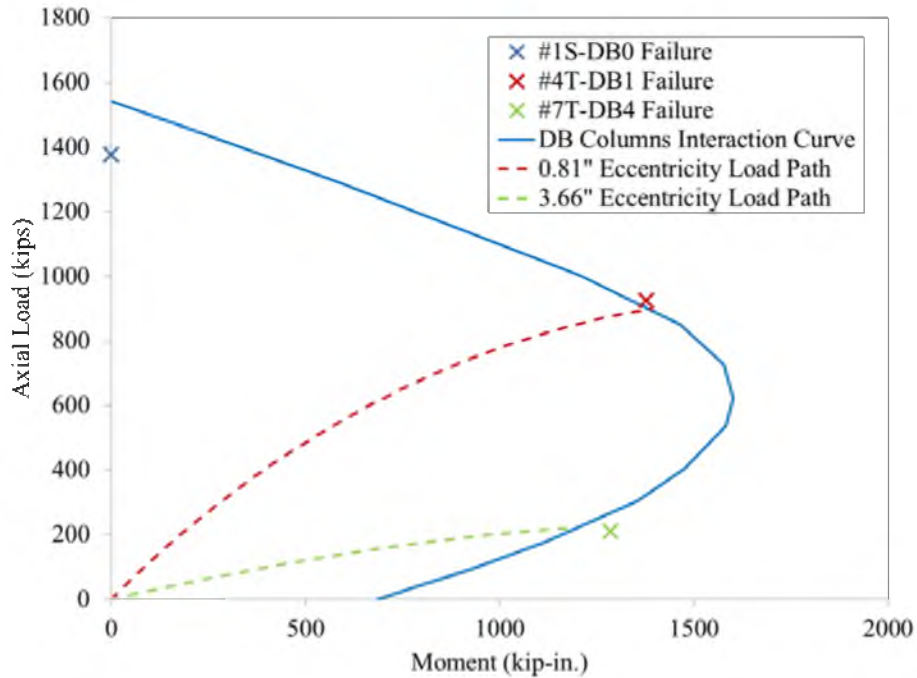


Figure 4.30: Axial load-moment interaction curve for DB columns (steel and GFRP longitudinal bars)

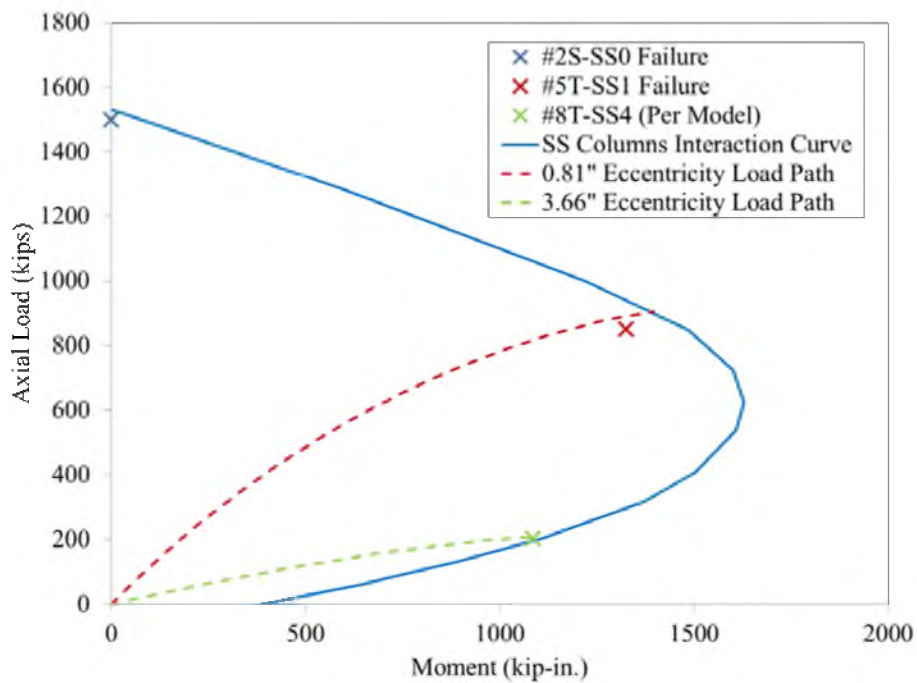


Figure 4.31: Axial load-moment interaction curve for SS columns (steel longitudinal bars)

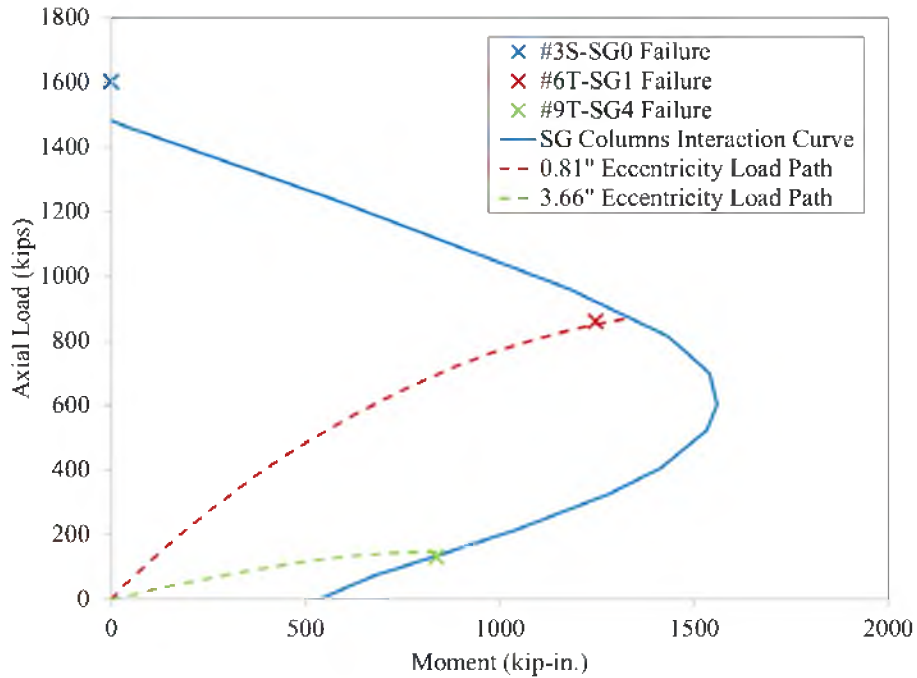


Figure 4.32: Axial load-moment interaction curve for SG columns (GFRP longitudinal bars)

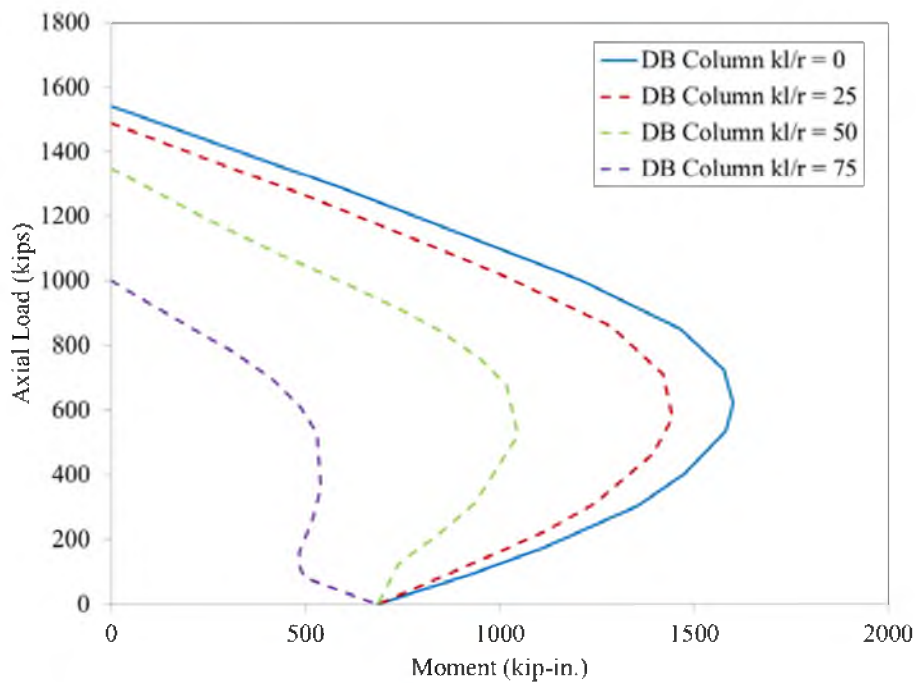


Figure 4.33: Slender column axial load-moment interaction curve for DB columns (steel and GFRP longitudinal bars)

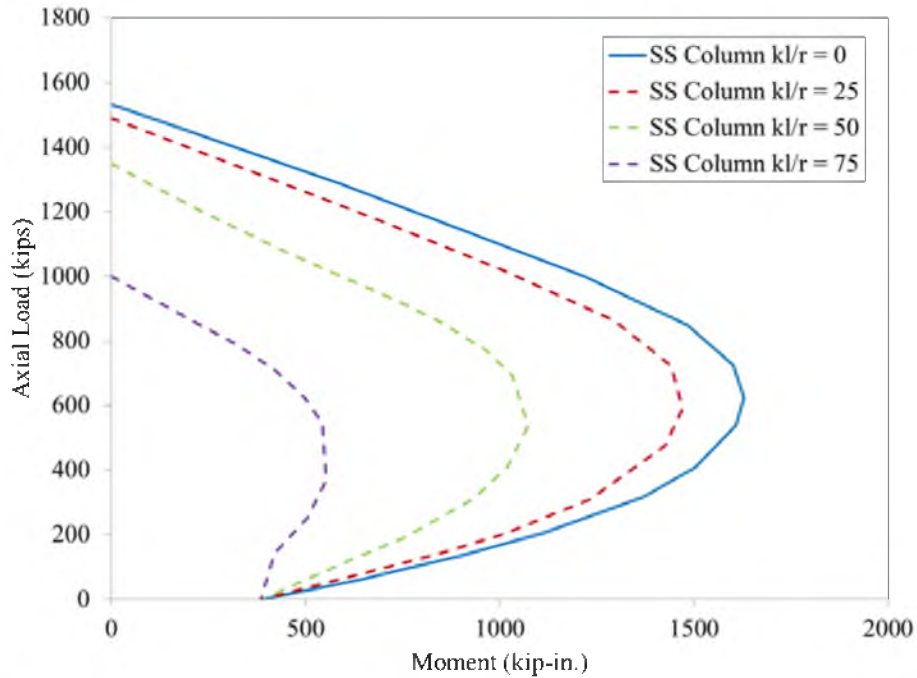


Figure 4.34: Slender column axial load-moment interaction curve for SS columns (steel longitudinal bars)

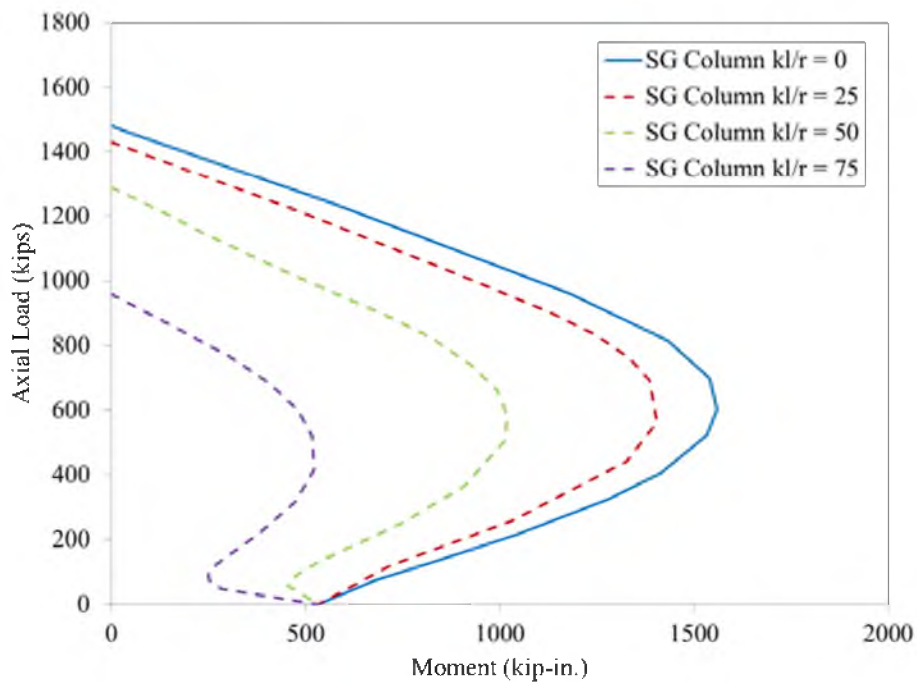


Figure 4.35: Slender column axial load-moment interaction curve for SG columns (GFRP longitudinal bars)

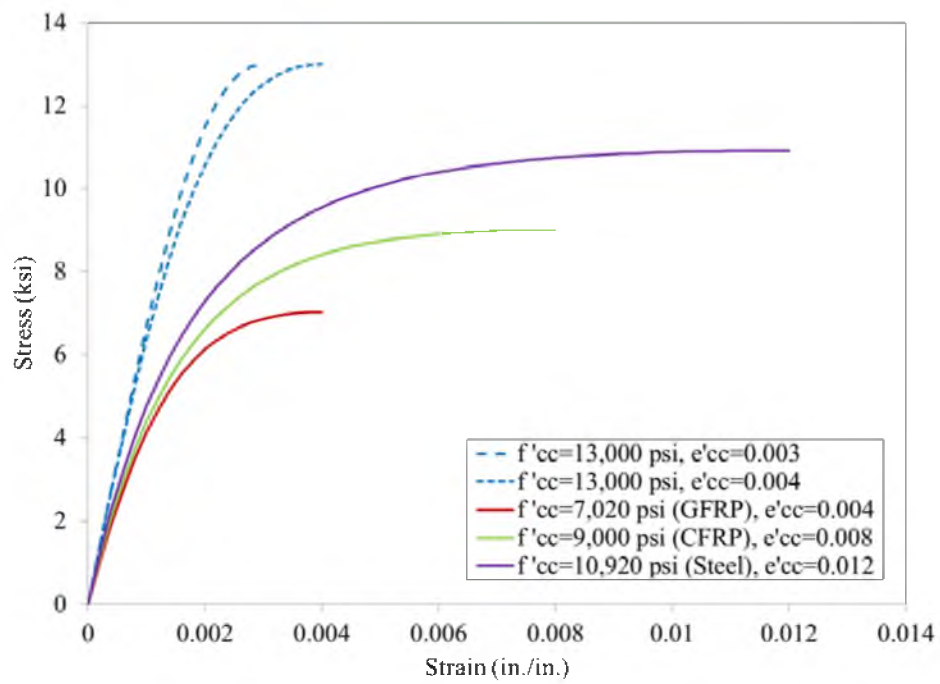


Figure 4.36: Comparison of stress-strain curves used for Parametric Study 1 and models of columns tested in present study

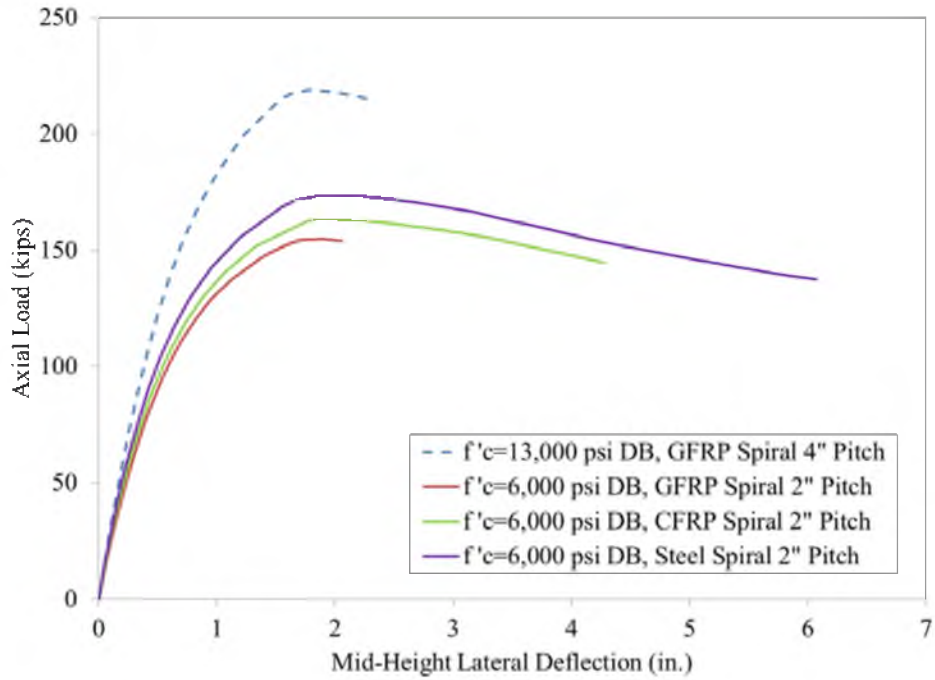


Figure 4.37: Load-deflection curves for Parametric Study 1 – DB columns

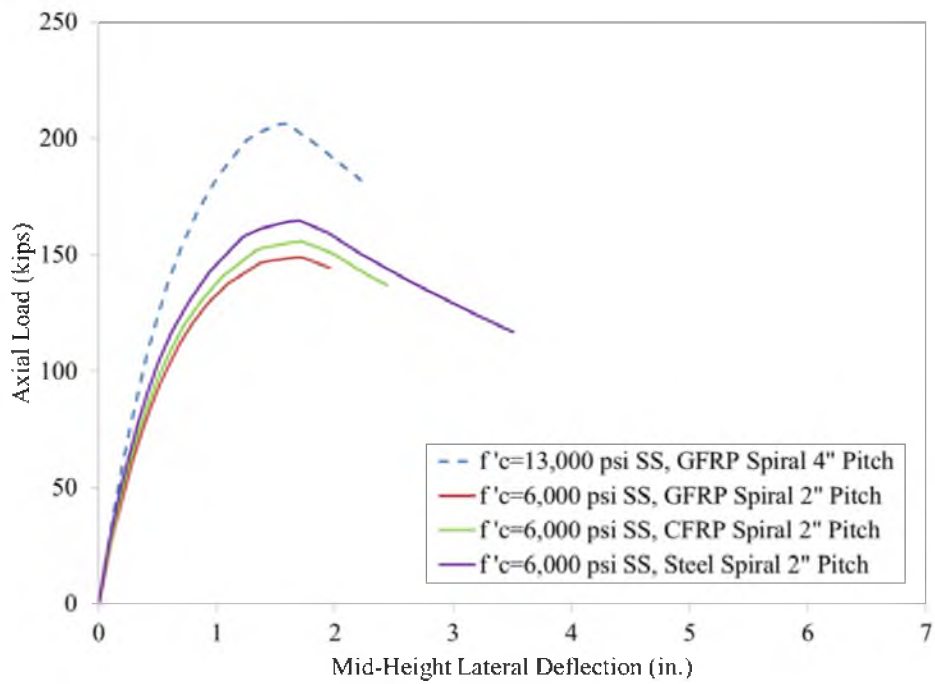


Figure 4.38: Load-deflection curves for Parametric Study 1 – SS columns

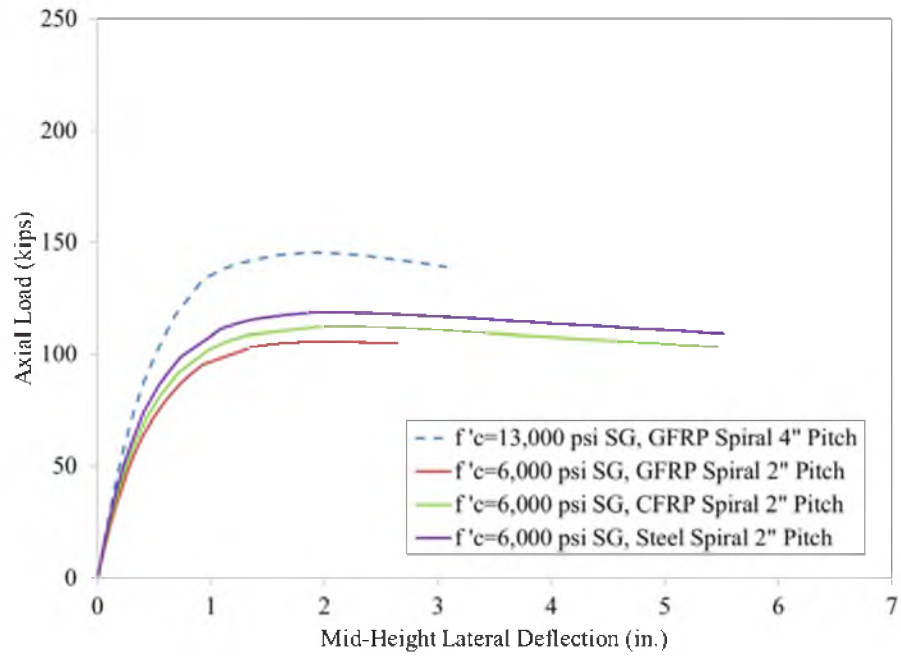


Figure 4.39: Load-deflection curves for Parametric Study 1 – SG columns

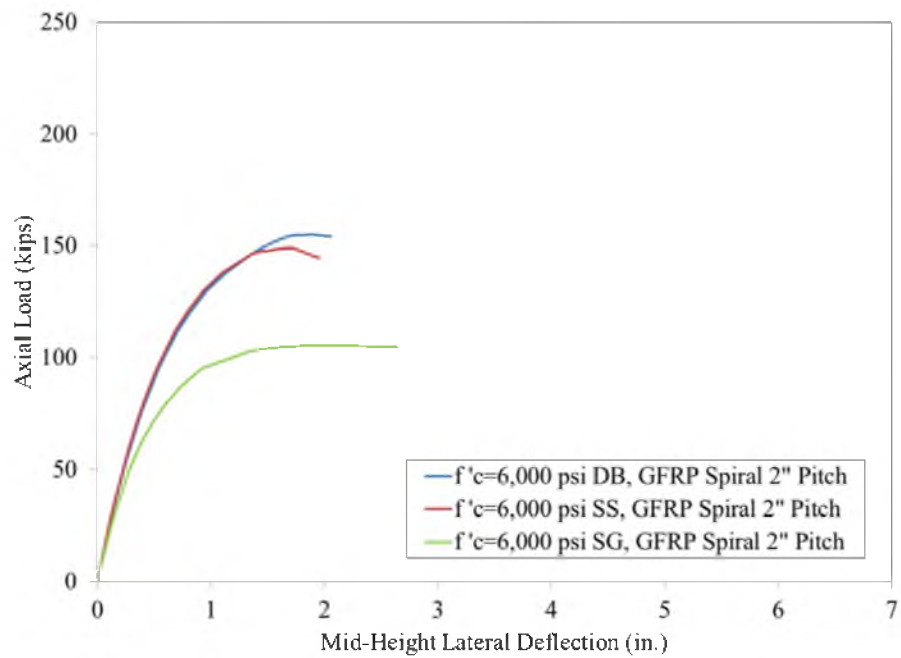


Figure 4.40: Comparison of load-deflection curves for Parametric Study 1 columns – GFRP-spiral

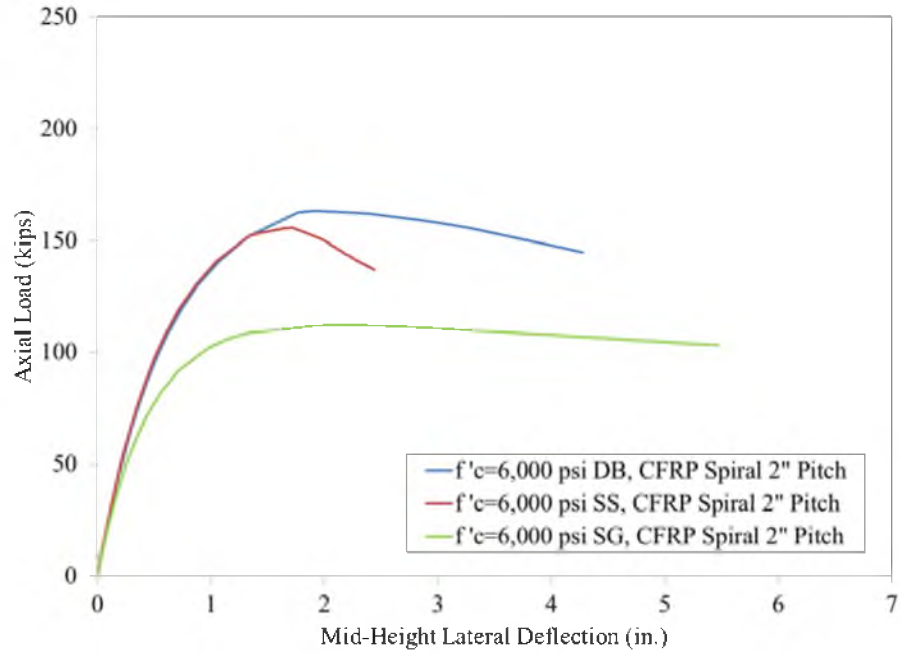


Figure 4.41: Comparison of load-deflection curves for Parametric Study 1 columns – CFRP-spiral

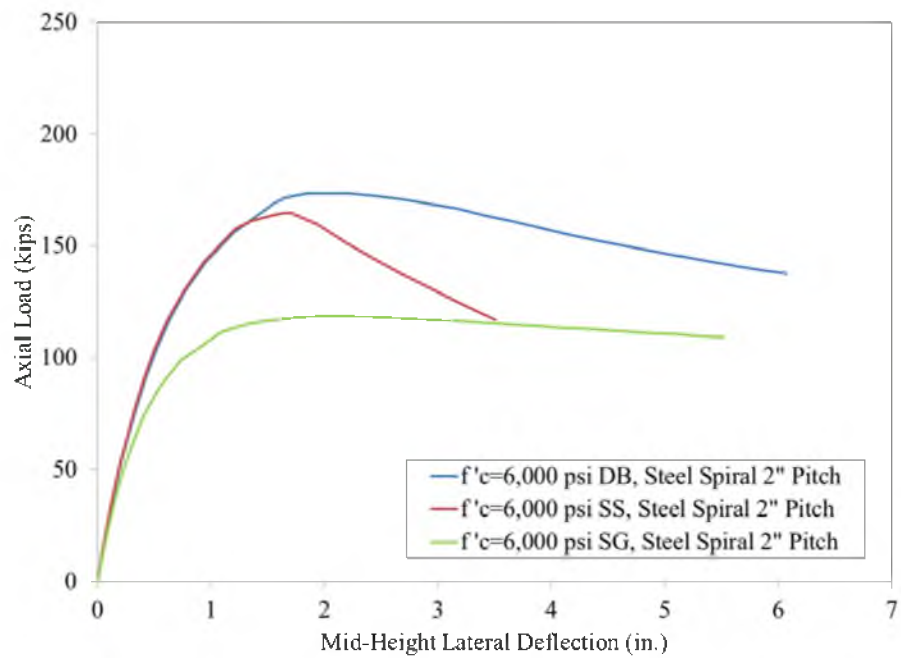


Figure 4.42: Comparison of load-deflection curves for Parametric Study 1 columns – steel spiral

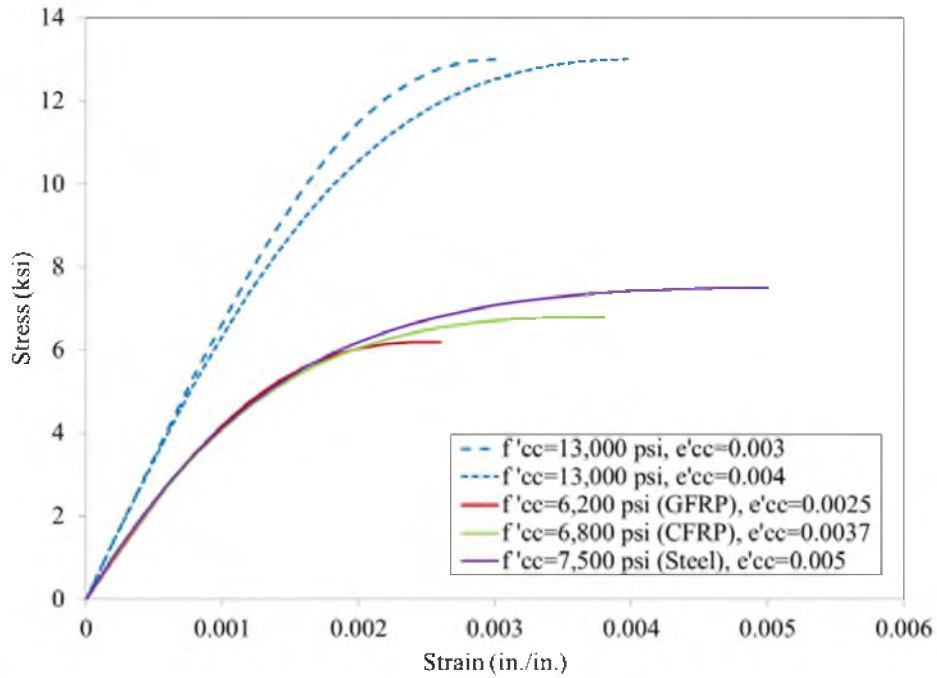


Figure 4.43: Comparison of stress-strain curves used for Parametric Study 2 and models of columns tested in present study

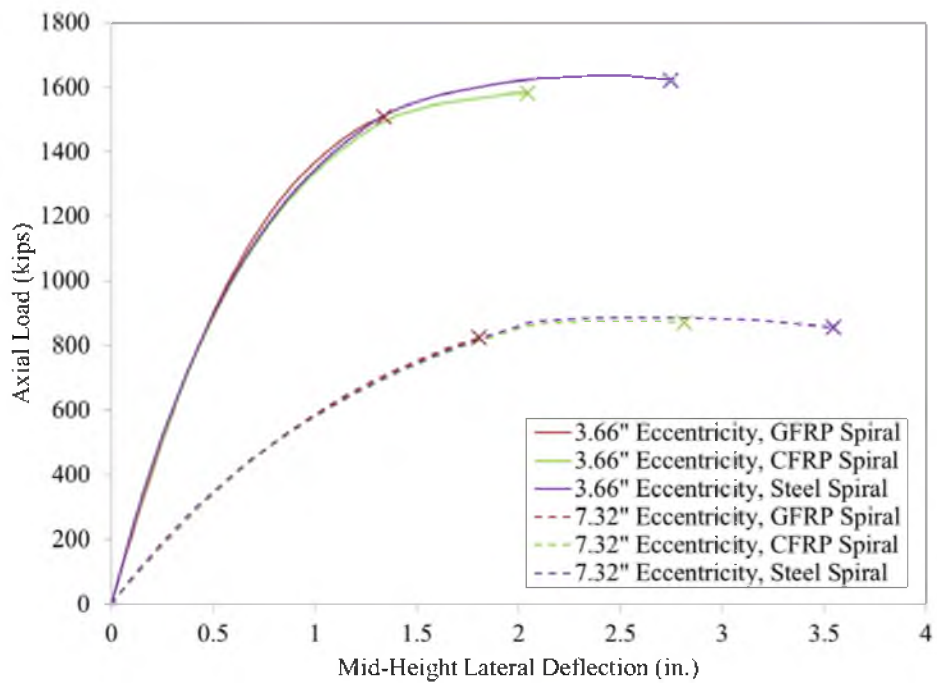


Figure 4.44: Comparison of load-deflection curves for Parametric Study 2 columns

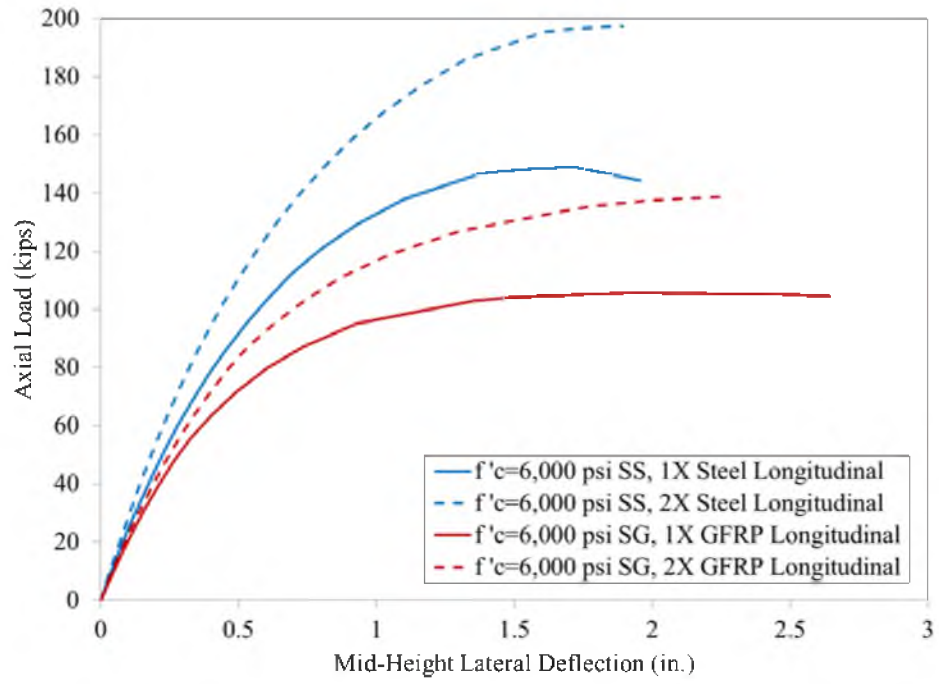


Figure 4.45: Comparison of load-deflection curves for Parametric Study 3 columns

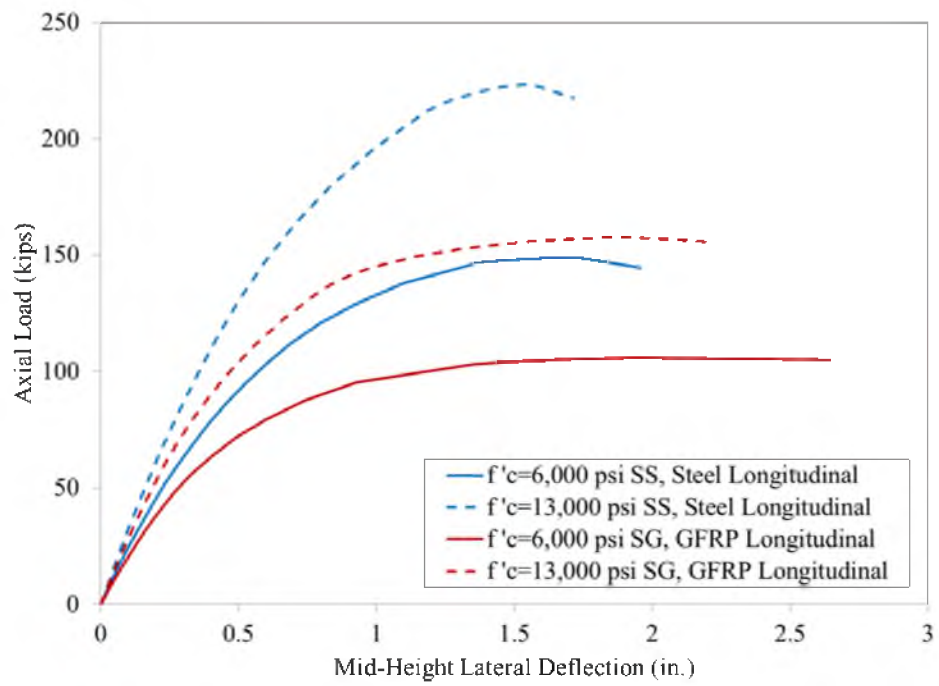


Figure 4.46: Comparison of load-deflection curves for Parametric Study 4 columns

## CHAPTER 5

### SUMMARY AND CONCLUSIONS

The present study investigated the use of FRP bars and spirals in short and slender concrete columns as a viable alternative to traditional steel reinforcement for improving axial strength and ductility while alleviating corrosion related deterioration. Experiments were conducted on nine large-scale concrete columns reinforced with internal GFRP-spirals and either steel, GFRP, or a combination of steel and GFRP longitudinal bars observing the failure mode, load capacity, and general behavior associated with these types of columns. The experimental data collected from these tests were utilized, along with data from other research, in developing an analytical confinement model to describe the axial strength and stress-strain relationship for FRP-spiral-confined circular columns. Furthermore, an analytical buckling model was developed utilizing a numerical integration method to enable modeling of the load-deflection behavior of slender, FRP-spiral-confined circular columns.

#### 5.1 Summary

Based on the experimental results and analytical models developed in this research, the following observations can be made:

1. The experimental failure mode for columns with low eccentricities (0 in. [0 %])

- and 1 in. [8.3%]) was compressive failure of concrete, compressive rupture of the longitudinal GFRP bars, compressive buckling of the longitudinal steel bars, and tensile rupture of the GFRP-spiral. It is expected that the compressive failure of the concrete initiated first, which instantly led to the occurrence of the other failure modes.
2. The experimental failure mode for columns with large eccentricities (4 in. [33%]) was a stability-type, buckling failure with the concrete cover on the compressive side breaking away near the column midheight due to bending compressive stresses where the bending moment was greatest. This failure was similar to what could be expected with a beam-column element subjected to combined axial and bending loading due to the large eccentricity.
  3. The use of GFRP-spirals is a viable means of providing noncorrosive confinement to enhance the axial load and ductility of concrete columns. However, given the same size and spacing, the confining pressure of GFRP-spirals is less effective than steel spirals due to the elastic behavior and lower modulus of elasticity of GFRP bars as compared to steel bars. Based on available test data at the present time utilizing FRP-spiral confinement, the provided normalized confining pressure,  $\frac{f_l}{f'_{co}}$ , of experimentally tested specimens had an average value of 0.006.
  4. It was found that the amount of GFRP-spiral reinforcement used for the high-strength concrete columns in the present study was below that required to provide an effective influence of confining pressure for enhancing the column's axial capacity. Further research is needed to determine the appropriate levels of GFRP or CFRP confinement to provide an effective confining pressure for high-strength

concrete.

5. The axial strength and stress-strain relationship for FRP-spiral-confined circular columns can be predicted through use of Eqs. (3.26), (3.27), or (3.30) and Eqs. (3.31) and (3.35). It is the author's hypothesis that Eq. (3.30) would likely better reflect the axial-strength-to-confinement relationship due to the lower confinement effectiveness of FRP-spirals. However, further research is needed to determine the appropriateness of these equations at higher levels of FRP-spiral confinement due to the limited number of tests available at the present time with FRP-spirals. The presented relationship is based on the assumption of a strain hardening behavior, which could also benefit from further experimental research for validation.
6. Using Eq. (3.30) of the present study's proposed analytical model, the axial load capacity of a concrete column confined with FRP-spirals with an average normalized confining pressure,  $\frac{f_l}{f'_{co}}$ , of 0.6 would be approximately 84% of a column similarly confined with steel spirals. This provides only a hypothetical example to give a comparison of the present model as compared to the model of Mander et al. (1988) for steel spirals, but, again, further research would be needed to validate the predictions of FRP-spirals at such a high level of confinement.
7. The maximum load capacity of short columns reinforced with internal GFRP-spirals and either steel, GFRP, or a combination of steel and GFRP longitudinal bars can be estimated using Eqs. (3.47), (3.48), and (3.49).
8. The load-deflection behavior of slender, FRP-spiral-confined circular columns can be predicted through the use of the analytical model and procedure presented

- in Chapter 4.
9. For slender columns with larger load eccentricities, columns with steel longitudinal bars are able to achieve significantly larger axial load capacities over those with only GFRP longitudinal bars because of the higher compressive strength contribution provided by the steel bars. This was found in both the analytical models as well as the experiments where the columns with a 4 in. (33%) eccentricity having steel longitudinal bars ( $\rho_{\text{steel}} = 1.06\%$ ) achieved at least a 37% increase in axial load over the columns having only GFRP longitudinal bars ( $\rho_{\text{GFRP}} = 1.65\%$ ).
  10. For slender columns with larger load eccentricities, columns with GFRP longitudinal bars are able to achieve larger lateral deflection capacities over those with only steel longitudinal bars because of the higher tensile strength capacity provided by the GFRP bars. This was found in both the analytical models as well as the experiments for columns with 4 in. (33%) eccentricity where a 12% minimum increase in lateral deflection was obtained with columns having GFRP longitudinal bars ( $\rho_{\text{GFRP}} = 1.65\%$ ) as opposed to columns having only steel longitudinal bars ( $\rho_{\text{steel}} = 1.06\%$ ).
  11. For slender columns with larger load eccentricities, columns with GFRP longitudinal bars are able to better maintain the axial load capacity once the lateral deflection continues beyond the peak load obtained. This is due to the GFRP's ability to contribute an increase in tensile strength with the increased moment-curvature demand from the larger deflection (as opposed to steel where its tensile strength is limited to the maximum yield strength).

12. The eccentricity from eccentric loading of circular columns can be affected by the distribution of load onto the column cross-sectional area. The transfer of load to the column circular cross-section can essentially reduce the effective eccentricity that the column is subjected to and is affected by the test setup.
13. At zero bending moment, the maximum load capacity of the slender column interaction diagrams for the DB and SS columns, which both have steel longitudinal reinforcement, was nearly the same even though the DB column also had additional GFRP longitudinal bars. Both load capacities, however, were larger than the all-GFRP (SG) column. This can be attributed to the lower compressive strength of the GFRP bars.
14. At zero axial load, the maximum moment capacity of the slender column interaction diagrams for the DB and SG columns, which both have GFRP longitudinal reinforcement, was larger (with the DB column being the largest) than the SS column, which had only steel longitudinal reinforcement. This can be attributed to the higher tensile capacity of the GFRP bars compared to the steel bars.
15. Based on Parametric Study 1, for a 12 in. diameter column, using the proposed analytical models and considering all other variables remaining the same (i.e., same longitudinal bars, same spiral size, same spiral pitch, etc.), there was approximately a 5% gain in axial load capacity when the spiral confinement material was changed from GFRP to CFRP and approximately a 10% gain going from GFRP to steel.
16. Based on Parametric Study 1, for a 12 in. diameter column, using the proposed

- analytical models and considering all other variables remaining the same (i.e., same longitudinal bars, same spiral size, same spiral pitch, etc.), there was a minimum of a 24% increase in lateral deflection capacity when the spiral confinement material was changed from GFRP to CFRP and at least a 80% increase from GFRP to steel. For the columns with GFRP longitudinal bars, this increase was typically on the order of at least a 100% increase for either GFRP to CFRP or GFRP to steel.
17. Based on Parametric Study 2, for a large-scale 24 in. diameter column, using the proposed analytical models and considering all other variables remaining the same (i.e., same longitudinal bars, same spiral size, same spiral pitch, etc.), it was found that even for a large-scale column the maximum lateral deflection increased at least 50% when increasing the confinement material from GFRP to CFRP and at least 95% from GFRP to steel. The increase in axial load was less pronounced with a minimum increase of approximately 4% from GFRP to CFRP and 8% from GFRP to steel.
18. Due to the higher modulus of elasticity of CFRP over GFRP, CFRP-spirals will potentially be able to provide higher confinement capacities than GFRP-spirals at levels more comparable to steel-spirals.
19. From Parametric Study 3, for both types of columns (steel longitudinal and GFRP longitudinal), there was approximately a 32% increase in axial load when the longitudinal reinforcement was doubled. The column with double the GFRP longitudinal reinforcement ( $A_s = 3.72$  sq. in.) had an axial load that was still less (93%) than that achieved with the column without doubling the steel longitudinal

reinforcement ( $A_s = 1.20$  sq. in.) even though it had approximately 3 times the area of longitudinal reinforcement. This validates the observation that GFRP longitudinal reinforcement has a lower compressive contribution to the overall axial load capacity of a column than steel longitudinal reinforcement.

20. From Parametric Study 4, for both types of columns (steel longitudinal and GFRP longitudinal), there was approximately a 50% increase in axial load when the concrete strength was increased from 6,000 psi to 13,000 psi (117% increase in concrete strength). The column with GFRP longitudinal reinforcement and 13,000 psi concrete strength had an axial load that was approximately 6% greater than the column with steel longitudinal reinforcement and 6,000 psi concrete. This again validates the observation that steel longitudinal reinforcement has a greater compressive contribution to the overall axial load capacity of a column than GFRP longitudinal reinforcement.

## 5.2 Conclusions

Based on the experimental results and analytical models developed in this research, the following conclusions can be made:

1. FRP spirals and FRP longitudinal bars can be a viable method of reinforcement for concrete columns, particularly in corrosive environments.
2. FRP spirals need to be placed with a closer pitch spacing to provide confinement levels similar to steel spirals due to the lower modulus of elasticity of FRP composites.
3. FRP longitudinal bars can provide larger deflection capacity (due to their higher tensile strength), and steel longitudinal bars can provide higher axial load capacity

(due to their higher modulus of elasticity), particularly for slender columns with larger eccentricities. A combination of both types of longitudinal bars can provide advantages of both within a column (i.e., larger deflection capacity and higher axial load capacity).

4. An analytical confinement model is presented that can be used to predict the axial strength and stress-strain relationship for FRP-spiral-confined circular columns.
5. An analytical buckling model is presented that can be used to predict the load-deflection curves of slender circular concrete columns, subjected to eccentric loads, reinforced with FRP or steel spirals and FRP and/or steel longitudinal bars. This model can be used to predict the behavior of columns with various configurations and materials (i.e., GFRP, CFRP and steel reinforcement, low to high strength concrete, varying pitches of spirals, etc.). Additionally, it can be used to model column interaction diagrams for FRP and/or steel reinforced, spiral-confined circular columns with different slenderness ratios.

## CHAPTER 6

### RECOMMENDATIONS FOR FUTURE RESEARCH

As observed in the present study, in addition to other limited research available regarding FRP-spiral-confined circular columns, it was found that FRP-spirals have a lower effectiveness of confinement in contrast to the more traditional means of confinement through the use of steel spirals or external FRP wraps. Future research needs to be conducted utilizing higher levels of confinement of FRP-spirals. This could be accomplished by utilizing larger diameter spirals with a closer pitch (similar to what was used in the parametric study) and/or the utilization of double layers of reinforcement similar to the experiments of the present study with the DB type columns. The use of CFRP as opposed to GFRP can also provide higher levels of confining pressure.

It is suggested that tests should be conducted on specimens with these higher levels of FRP-spiral confinement utilizing both normal-strength and high-strength concrete. Past research has shown that even with steel spirals the effectiveness of confinement is reduced when used with high-strength concrete as opposed to normal-strength concrete. The same effect would be expected with FRP-spirals thus validating the need to investigate its use in both normal-strength and high-strength concrete applications. Additional test data for higher levels of FRP-spiral confinement would allow the confinement models of the present study to be validated and refined as needed

based on the results from this additional data.

At higher levels of FRP-spiral confinement, it is also recommended that additional tests be performed on tall, slender columns reinforced with either all-steel bars or all-FRP bars to better differentiate the behavior between the two in the context of slender buckling failures. As found in the present study there can be benefits to both types of reinforcement (FRP provides greater deflection capacity and steel provides greater axial load capacity), and further research would provide better understanding of the advantages and disadvantages of both reinforcement types. Extension of this work by conducting tests on hybrid columns reinforced with a mixture of both steel and FRP longitudinal bars with either steel or FRP-spirals would be even more advantageous. This would provide additional insight on capturing the benefits of both types of reinforcement in a single specimen.

In addition to the above recommendations, additional long term corrosion studies to verify the advantages of FRP-spirals as observed by Pantelides et al. (2013a) and the development of practical implementations of FRP reinforcement to overcome the field bending limitations of its use would also be beneficial. Lateral load tests for columns with FRP-spirals to investigate their behavior under seismic loading would be another worthwhile endeavor.

## REFERENCES

- AASHTO (American Association of State Highway and Transportation Officials). (2009). *AASHTO LRFD bridge design guide specifications for GFRP reinforced concrete decks and traffic railings, 1st Edition*, Washington, D.C.
- ACI (American Concrete Institute). (2006). “Guide for the design and construction of structural concrete reinforced with FRP bars.” *ACI 440.1R-06*, Farmington Hills, MI.
- ACI (American Concrete Insitute) Committee 318. (2005). “Building code requirements for structural concrete (ACI 318-05) and commentary (318 R-05).” *ACI 318-05 and ACI 318R-05*, Farmington Hills, MI.
- ACI (American Concrete Institute) Committee 318. (2008). “Building code requirements for structural concrete (ACI 318-08) and commentary (318 R-08).” *ACI 318-08 and ACI 318R-08*, Farmington Hills, MI
- Afifi, M. Z., Mohamed, H. M., and Benmokrane, B. (2013a), “Axial capacity of circular concrete columns reinforced with GFRP bars and spirals.” *J. Compos. Constr.*, 10.1061/(ASCE)CC.1943-5614.0000438, 1–11
- Afifi, M. Z., Mohamed, H. M., and Benmokrane, B. (2013b), “Strength and axial behavior of circular concrete columns reinforced with CFRP bars and spirals.” *J. Compos. Constr.*, 10.1061/(ASCE)CC.1943-5614.0000430, 1–11
- Alsayed, S. H., Al-Salloum, Y. A., Almusallam, T. H., and Amjad, M. A. (1999). “Concrete columns reinforced by glass fiber reinforced polymer rods.” *Proc., Fourth Int. Symp. FRP Reinforcement for Reinf Conc. Struct., SP-188, C. W. Dolan, S. H. Rizkalla, and A. Nanni, eds.*, American Concrete Institute, Farmington Hills, MI, 103–112.
- Ansari, F., and Li, Q. (1998). “High-strength concrete subjected to triaxial compression.” *ACI Mater. J.*, 95(6), 747–755.
- Bank, L. C. (1993). “Properties of FRP reinforcement for concrete.” *Fiber-Reinforced-Plastic (FRP) Reinforcement for Concrete Structures: Properties and Applications, Developments in Civil Engineering, 42, A. Nanni, ed.*, Elsevier, Amsterdam, 147–157
- Benzaid, R., Chikh, N. E., and Mesbah, H. (2008). “Behaviour of square concrete column confined with GFRP composite wrap.” *J. Civ. Eng. Manage.*, 14(2), 115–120.

- Bing, L., Park, R., and Tanaka, H. (2001). "Stress-strain behavior of high-strength concrete confined by ultra-high-and normal-strength transverse reinforcements." *ACI Struct. J.*, 98(3), 395–406.
- CAN/CSA-S6-06. (2006). *Canadian Highway Bridge Design Code*, Clause 16.8.6, Canadian Standards Association (CSA) International, Toronto, ON.
- CSA A23.3. (2004). *Design of Concrete Structures*. Canadian Standards Association (CSA), Toronto, ON.
- Chen, W. F., and Han, D. J. (1982). *Plasticity for Structural Engineering*. Springer-Verlag, NY.
- Choo, C. C., Harik, I. E., and Gesund, H. (2006). "Strength of rectangular concrete columns reinforced with fiber-reinforced polymer bars." *ACI Struct. J.*, 103(3), 452–459.
- Claeson, C., and Gylltoft, K. (1998). "Slender high-strength concrete columns subjected to eccentric loading." *J. Struct. Eng.*, 124(3), 233–240.
- Cranston, W. B. (1972). "Analysis and design of reinforced concrete columns." *Research Report 20*, Cement and Concrete Association, UK
- Csuka, B., and Kollar, L. P. (2012). "Analysis of FRP confined columns under eccentric loading." *Compos. Struct.*, 94(2012), 1106–1116.
- Cusson, D. and Paultre, P. (1995). "Stress-strain model for confined high-strength concrete." *J. Struct. Eng.*, 121(3), 468–477.
- De Luca, A., Matta, F., and Nanni, A. (2009). "Behavior of full-scale concrete columns internally reinforced with glass FRP bars under pure axial load." *Composites & Polymers 2009*, American Composites Manufacturers Association, Tampa, FL, 1–10.
- De Luca, A., Matta, F., and Nanni, A. (2010). "Behavior of full-scale glass fiber-reinforced polymer reinforced concrete columns under axial load." *ACI Struct. J.*, 107(5), 589–596.
- Elwi, A. A., and Murray, D. W. (1979). "A 3D hypoelstic concrete constitutive relationship." *J. Eng. Mech., Am. Soc. Civ. Eng.*, 105(4), 623–641.
- Fitzwilliam, J. and Bisby, L. (2006). "Slenderness effects on circular FRP-wrapped reinforced concrete columns." *Proc., 3rd Int. Conf FRP Comp. Civ. Eng.*, 13–15 December 2006, Miami, FL, 499–502.
- Fitzwilliam, J., and Bisby, L.A. (2010). "Slenderness effects on circular CFRP-confined reinforced concrete columns." *J. Compos. Constr.*, 14(3), 280–288.

- Imran, I. (1994). "Application of non-associated plasticity in modeling the mechanical response of concrete." Ph.D. Dissertation, University of Toronto, 1994.
- Imran, I. and Pantazopoulou, S. J. (1996). "Experimental study plan of plain concrete under triaxial stress." *ACI Mater. J.*, 93(6), 589–601.
- Jiang, T. and Teng, J. G. (2012). "Theoretical model for slender FRP-confined circular RC columns." *Constr. Build. Mater.*, 32(2012), 66–76.
- Jiang, T. and Teng, J. G. (2013). "Behavior and design of slender FRP-confined circular RC columns." *J. Compos. Constr.*, 17(4), 443–453.
- Kim, J. K. and Yang, J. K. (1995). "Buckling behaviour of slender high-strength concrete columns." *Eng. Struct.*, 17(1), 39–51.
- Lam L., and Teng, J. G. (2003). "Design-oriented stress-strain model for FRP-confined concrete in rectangular columns." *Constr. Build. Mater.*, 17(6–7), 471–489.
- MacGregor, J. G., Breen, J. E., and Pfrang, E. O. (1970). "Design of slender concrete columns." *ACI J.*, 67(2), 6–28.
- Mander J. B., Priestley, J. N., and Park R. (1988). "Theoretical stress-strain model for confined concrete." *J. Struct. Eng.*, 114(8), 1804–1826.
- Mirmiran, A., Yuan, W., and Chen, X. (2001). "Design for slenderness in concrete columns internally reinforced with fiber-reinforced polymer bars." *ACI Struct. J.*, 98(1), 116–125.
- Mizuno, E., and Hatanaka, S. (1992). "Compressive softening model for concrete." *J. Eng. Mech., Am. Soc. Civ. Eng.*, 118(8), 1546–1563.
- Mohamed, H. M., Afifi, M. Z., and Benmokrane, B. (2014). "Performance evaluation of concrete columns reinforced longitudinally with FRP bars and confined with FRP hoops and spirals under axial load." *J. Bridge Eng., Am. Soc. Civ. Eng.*, 10.1061/(ASCE)BE.1943-5592.0000590(2014), 1–12.
- Moran, D. A. and Pantelides, C. P. (2012). "Elliptical and circular FRP-confined concrete sections: a mohr-coulomb analytical model." *Int. J. Solids Struct.*, 49(2012), 881–898.
- Newmark, N. M. (1943). "Numerical procedure for computing deflections, moments, and buckling loads." *ASCE Trans.*, 108, 1161–1234.
- Oztekın, E., Pul, S., and Husem, M. (2003). "Determination of rectangular stress block parameters for high performance concrete." *Eng. Struct.*, 25(2003), 371–376.

Pantelides, C. P., Gibbons, M. E., and Reaveley, L. D. (2013a). "Axial load behavior of concrete columns confined with GFRP spirals." *J. Compos. Constr.*, 17, 305–313.

Pantelides, C. P., Ries, J., and Nix, R. (2013b). "Construction and monitoring of a single-span bridge with precast concrete glass-fiber-reinforced polymer reinforced deck panels." *PCI J.*, Winter 2013, 78–95.

Pfrang, E. O. and Siess, C. P. (1961). "Analytical study of the behavior of long restrained reinforced concrete columns subjected to eccentric loads." *Civil Engineering Studies, Structural Research Series No. 214*, University of Illinois, Urbana, IL.

Popovics, S. (1973). "Numerical approach to the complete stress-strain relation for concrete." *Cem. Concr.*, 1973, 3(5), 583–599.

Ranger, M., and Bisby, L. (2007). "Effects of load eccentricities on circular frp-confined reinforced concrete columns." *Proc., 8th Int. Symp. on FRP Reinf for Conc. Struct. (FRPRCS-8)*, University of Patras, Patras, Greece, 16–18 July 2007.

Richart, F. E., Brandtzaeg, A., and Brown, R. L. (1928). "A study of the failure of concrete under combined compressive stresses." *Bulletin 185, University of Illinois Engineering Experimental Station*, Champaign, IL.

Schickert, G., and Winkler, H. (1979). "Results of tests concerning strength and strain of concrete subjected to multiaxial compressive stresses." *Deutscher Ausschuss für Stahlbeton, Heft 277*, Berlin, West Germany.

Sheikh, S. A. and Toklucu, M. T. (1993). "Reinforced concrete columns confined by circular spirals and hoops." *ACI Struct. J.*, 90(5), 542–553.

Sheikh, S. A. and Uzumeri, S. M. (1980). "Strength and ductility of tied concrete columns." *J. Struct. Div., Am. Soc. Civ. Eng.*, 106(5), 1079–1102.

Shen, Z. Y. and Lu, L. W. (1983). "Analysis of initially crooked, end restrained steel columns." *J. Constr. Steel Res.*, 3(1), 10–18.

Smith, S. S. (1987). "On fundamental aspects of concrete behavior." *Structural Research Series, No. 87-12. C.E.A.E. Department*, University of Colorado, Boulder, CO.

Sohanghpurwala, A.A., and Scannall, W.T. (1999). "Condition and Performance of Epoxy-Coated Rebars in Bridge Decks." *Public Roads, Federal Highway Administration*, 63(3).

Tikka, T. (2008). "Strength of concrete columns reinforced with GFRP bars." *Australasian Struct. Eng. Conf 2008: Engaging with Struct. Eng.*, Melbourne, Australia, 968–977.

- Tikka, T. K., and Mirza, S. A. (2006). "Nonlinear equation for flexural stiffness of slender composite columns in major axis bending." *J. Struct. Eng.*, 132(3), 387–399.
- Tobbi, H., Farghaly, A. S., and Benmokrane, B. (2012). "Concrete columns reinforced longitudinally and transversally with glass fiber-reinforced polymer bars." *ACI Struct. J.*, 109(4), 551–558.
- Todeschini, C. E., Bianchini, A. C., and Kesler, C. E. (1964). "Behavior of concrete columns reinforced with high-strength steels." *ACI J., Proc.*, 61(6), 701–716.
- Willam, K. J., and Warnke, E. P. (1975). "Constitutive model for the triaxial behavior of concrete." *Proc., Int. Assoc. Bridge Struct. Eng.*, Vol. 19, 1–30.
- Yan, Z. (2005), "Shape modification of rectangular columns confined with FRP composites." Dissertation, University of Utah.
- Yan, Z., and Pantelides, C. P. (2006). "Fiber-reinforced polymer jacketed and shape-modified compression members: II-model." *ACI Struct. J.*, 103(6), 894–903.